

Graz University of Technology  
Institute for Thermal Turbomachinery and Machine Dynamics

# Alternative Fuels and Bio-Fuels for Aviation

## Analysis of the Evaporation in a Combustion Chamber

DISSERTATION

for the Degree of Doctor of Engineering Sciences

submitted to

the Faculty of Mechanical Engineering,  
Graz University of technology

by

Dipl. Ing. Johannes Fritzer

*Rewiever 1:* Univ.-Prof. Dr.-Ing. Franz Heitmeir

*Rewiever 2:* Univ.-Doz. Dipl.-Ing. Dr.techn. Fabrice Giuliani

Graz, October 2013

Funded by the European Commission (EC) within the 7<sup>th</sup> framework program ALFA BIRD  
(Grant No. EU FP7: ACP/-6A-2008-213266).



Je planmässiger die Menschen vorgehen, desto wirksamer trifft sie der Zufall.

*-Friedrich Dürrenmatt-*

### **Statutory Declaration**

*I declare that I have authored this thesis independently, that I have not used other than declared sources / resources, and that I have explicitly marked all material which has been quoted either literally or by content from the used sources*

---

Place

---

Date

---

Signature

## **Acknowledgements**

The underlying contribution was written during my time as research associate at the Institute for Thermal Turbomachinery and Machine Dynamics at Graz University of Technology. I would like to thank the head of the institute Univ.-Prof. Dr.-Ing. Franz Heitmeir for the support and the supervision of this work.

Furthermore I wish to thank Univ.-Doz. Dipl.-Ing. Dr.techn Fabrice Giuliani for his motivation and support in technical and organizational concerns and as well his assistant Jaana Rajamäki for her ambitious work within the literature survey.

I would also like to thank Dipl.-Ing. Dr.techn. Thomas Leitgeb, whose extensive expertise has always been advantageous for the underlying work of this doctoral thesis.

Finally I'd like to thank my family and friends for their persistent emotional support.

## **Abstract**

Due to an increasing oil price and the probable impact of the combustion of fossil fuel-derivatives on climate change on one hand and the depletion of hydrocarbon natural resources and the steady growth of transportation needs on the other, there is a need to develop alternatives to oil also for aeronautics.

For this purpose a specific research programme on the investigation of adequate alternatives to oil for aircraft implementation was founded by the European Commission's Framework Programme. It is called Alfa Bird which stands for Alternative Fuels and Bio-fuels in Aircraft Development. This consortium is made up of several industrial partners, research and educational institutions on aeronautics as well as oil companies and aims to investigate the adaptability of conventional aircraft engines to the use of alternative fuels such as Gas To Liquid (GTL), Coal To Liquid (CTL), Naphtenic Cut and blendings of GTL with HVO (Hydrogenated Vegetable Oils). Due to the very long lifetime of current civil aircraft and because of very strict operational constraints (e.g. flight in very cold conditions) it is a great challenge to use bio-fuels and alternative fuels in aircrafts.

The main objectives of this project were an identification of possible alternative fuels to kerosene, the investigation of the adequacy of the selected ones, an evaluation of the environmental and economic performance of those and finally the creation of a future perspective for the industrial use of the "best" alternative.

The main part of the investigation activities in the Institute of Thermal Turbomachinery and Machine Dynamics (ITTM) at TU Graz, in cooperation with ONERA Centre de Toulouse and Fauga-Mauzac on these specific topics consisted on one hand in an extensive study addressing to existing investigations on alternatives to conventional fossil-based standard jet fuels as well as on the existence and development of new technologies related to this topic, especially on the combustor sector for jet engines. The main outcomes of this study are presented in the first part of this contribution.

On the other hand TU-Graz's experimental work focused on the analysis of the evaporation of the previously chosen fuel types in comparison to conventional Jet A1 fuel. Therefore an evaporation test rig has been installed in the combustion-laboratory of the ITTM. A test combustor was installed which has also been used at ONERA, who focused on the atomization of the chosen fuel types. Due to the analysis being isothermal, which means without combustion, it was necessary to install an afterburner unit to reduce the unburned hydrocarbons led into the exhaust tower. In order to analyze the evaporation gradients in the test combustion chamber the Infrared Extinction Method was applied to the setup. This measurement technique was validated and then integrated in the automation conglomerate of the test rig. After the entire setup has been initiated and tested the required points in the Alfa Bird test matrix were detected, displayed and finally interpreted.

# Contents

Contents	5
Nomenclature	8
Abbreviations .....	8
Parameters .....	9
Chapter 1 Introduction	1
Chapter 2 Fuels	7
2.1 Initial selection .....	7
Chapter 3 Existing Technologies and Investigations	10
3.1 Emissions and low-emission technologies with conventional fuels.....	10
3.1.1 Specifications of a Gas Turbine (GT) combustor .....	10
3.1.1 Target emissions to be reduced .....	12
3.1.2 Combustor architectures .....	15
3.1.3 Other parameters of importance.....	18
3.2 Open literature survey .....	21
3.2.1 Spectrum of products .....	21
3.2.2 Kerosene Jet A1 .....	22
3.2.3 Biodiesel .....	23
3.2.4 Vegetable oils.....	27
3.2.5 Hydrotreated vegetable oil [25] .....	28
3.2.6 Alcohol fuels.....	29
3.2.7 Hydrogen .....	32
3.2.8 Synthetic fuels (XtL) .....	34
Chapter 4 Analysis of the Alfa-Bird data	37
4.1.2 Comparison of the performance (stability and emissions) of a real airblast nozzle working with normal/alternative fuel at atmospheric pressure [37] .....	37
4.1.3 Experimental database on the effect of fuel reformulation on pollutants emissions: Specification of pollutants formed by reformulated kerosene [40] .....	39
4.1.4 ONERA contribution – Spray atomization and evaporation from atmospheric to high pressure: LACOM experiments [31] .....	40
4.1.5 Report on evaluation of Well to Tank greenhouse gas emissions [43] .....	40
Chapter 5 Measurement Techniques	41
5.1 Laser Doppler Anemometry .....	41

---

5.1.1	Principle .....	41
5.1.2	Configuration .....	45
5.2	Infrared Extinction Method.....	46
5.2.1	Technical fundamentals .....	46
	Spectra of rotation and oscillation of a 2-atomic molecule .....	47
	Transition Intensity .....	48
	Absorption band of the C-H Valence oscillation .....	49
	The Beer-Lambert law .....	51
	The $d^2$ law .....	51
	Influence of convection .....	53
	The Stefan flow.....	54
5.2.2	IRE measurement principle in a spray.....	54
5.2.3	Error analysis.....	59
Chapter 6	Test Rig .....	62
6.1	Hot/Cold Flow facility .....	62
6.2	Fuel supply Feed .....	64
6.2.1	Schematic of the fuel supply .....	64
6.3	Combustor design .....	68
6.4	Afterburner design .....	72
6.5	Thermodynamic dimensioning of the afterburner concept .....	73
6.5.1	Evaporation tube zone .....	73
6.5.2	Mixing zone.....	75
6.5.3	Flame tube zone .....	76
6.5.4	Dilution zone .....	82
6.5.5	Geometric dimensioning of the combustion chamber.....	83
6.5.6	Optical access and ignition.....	86
Chapter 7	Initialisation and Main Flow Analysis .....	89
7.1	Atmospheric tests of ignition of the radial swirl combustor .....	89
7.2	LDA Measurements .....	90
7.3	Setup Initialisation Test.....	93
7.4	IRE measurements with ultrasonic injector .....	95
7.4.1	Beam Analysis.....	98
7.4.2	Tests on the fuel spray .....	100
Chapter 8	IRE measurements .....	104

8.1	Setup.....	104
8.1.1	Results.....	107
Chapter 9	Summary / Results	114
Chapter 10	Bibliography	116

# Nomenclature

## Abbreviations

ASTM	American Society for Testing and Materials
BSA	Burst Spectrum Analyzer
CAEP	Comitee on Aviation Environmental Protection
CCS	Carbon Capture Storage
CH <sub>4</sub>	Methane
CO	Carbon monoxide
CO <sub>2</sub>	Carbon dioxyde
CTL	Coal To Liquid
CW	Continuous Wave
DAC	Double Annular Combustor
DCL	Direct Coal Liquefaction
DEHS	Di-Ethyl-Hexyl-Sebacin-Ester
DLR	Deutsches Zentrum für Luft und Raumfahrt
FAE	Fatty Acid Ester
FAME	Fatty Acid Methyl Ester
FTSPK	Fischer Tropsch Synthetic Paraffinic Compound
FSJF	Fully Synthetic Jet Fuel
GHG	Greenhouse Gas
GPH	Gallons Per Hour
GTL	Gas To Liquid
HVO	Hydrogenated Vegetable Oil
H <sub>2</sub> SO <sub>4</sub>	Sulphuric Acid
HRJ	Hydrotreated Renewable Jet Fuel
IATA	International Air Transport Association
ICAO	International Civil Aviation Organisation
ICL	Indirect Coal Liquefaction
IO	Injection Outlet
IR	Infrared
JFTOT	Jet Fuel Thermal Oxidation Test Breakpoint
LBO	Lean Blow Out limit
LDA	Laser Doppler Anemometer
LIF	Laser Induced Fluorescence
LOSU	Level of Scientific Understanding
LPP	Lean Premixed Prevaporized
LTO	Landing and Take Off
LUC	Land Use Change
NEWAC	New Aero Engine Core Concepts
NGV	Nozzle Guide Vane
NO <sub>x</sub>	Nitrous Oxyde
OPR	Operation Pressure Ratio

---

OTDF	Overall Temperature Distribution Factor
PAH	Polyaromatic Hydrocarbons
PERM	Partially Evaporated Rapid Mixing
PDA	Phase Doppler Anemometer
PLC	Programmable Logic Controller
PSC	Polar Stratospheric Clouds
RF	Radiative Forcing
RME	Rapeseed Methyl ester
RPK	Revenue passenger kilometers
RQL	Rich Quench Lean
S	Swirlnumber
SAC	Single Annular Combustor
SMD	Sauter mean diameter
SO <sub>x</sub>	Sulphur oxide
TAPS	Twin Annular Premixing Swirler
TEM	Transversal Electromagnetic
TSFC	Specific Fuel Consumption
UHC	Unburned Hydrocarbons
VIS	Visual

### Parameters

$\Phi$	Equivalence Ratio
$f'$	Frequency shift
$f_0$	Wave frequency
$\vec{u}$	Velocity vector of particle
$\vec{I}$	Directional vector
$c$	Speed of light
$\mu$	Reduced mass of the molecules
$\tilde{\nu}$	Wavenumber
$k$	Constant force parameter
$h$	Planck constant
$J$	Quantum number
$\rho$	Radiation intensity
$k(\nu)$	Absorption index
$\overline{C_n}$	Line-of-Sight Averaged Number Density
$N(D)$	Drop Diameter Distribution
$Q_{sca}$ and $Q_{abs}$	Scattering and Absorption Efficiency
$c_m(x)$	Integral Vapor Concentration
$\alpha_{IR}$	Absorption Coefficient
$L$	Length of Laser Penetration through medium
$\lambda_{abs}$ and $\lambda_{na}$	Absorbing and Non-absorbing Wavelength
$f$	Focal Length
$p$	Pressure
$T$	Temperature
$B$	Spalding number
$Nu$	Nusselt number

Re	Reynolds number
Sh	Sherwood number
Pr	Prandtl number
Sc	Schmidt number
Le	Lewis number
$\tau_{abs}$ and $\tau_{na}$	Optical Thickness
$D_{20}$	Area Mean Diameter
$D_{32}$	Sauter Mean Diameter
Qa	Heat transfer,
W	Technical work,
H	Incoming and outgoing enthalpy
Ea	System immanent energy either kinetic or potential energy
r(T)	Latent heat of vaporization
$c_p$	Heat capacity
$L_{min}$	Minimum air demand for stoichiometry
$\eta_A$	Combustion efficiency

# Chapter 1

## Introduction

With the start of industrial revolution, which had been initiated in 1769 by the invention of the steam engine, combustion of fossil combustibles and fuel derivatives such as coal, natural gas and crude oil became essential for aspects of industrialization and mobility purposes. The combustion of fossil fuel resources has the negative side effect of pollutant production such as Nitrous oxides ( $\text{NO}_x$ ), Carbon monoxide ( $\text{CO}$ ) and Hydrocarbon compounds ( $\text{HC}$ ), which are all defined as either toxic or carcinogenic. As well as Carbon dioxide ( $\text{CO}_2$ ) which represents the most important part of the so called greenhouse gases (GHG) (Figure 1.1). These gases dominate the effect of atmospheric radiative forcing, an indicating factor for the alteration of the balance of incoming and outgoing energy in the earth's atmosphere<sup>1</sup>. Other anthropogenic GHGs are Nitrous oxides ( $\text{N}_2\text{O}$ ), Methane ( $\text{CH}_4$ ) and F-Gases (Hydrofluorocarbons, Perfluorocarbons, Sulphurhexafluorides) which play as well a crucial role directed to the greenhouse effect, but are not primarily produced by the combustion of fossil fuels.

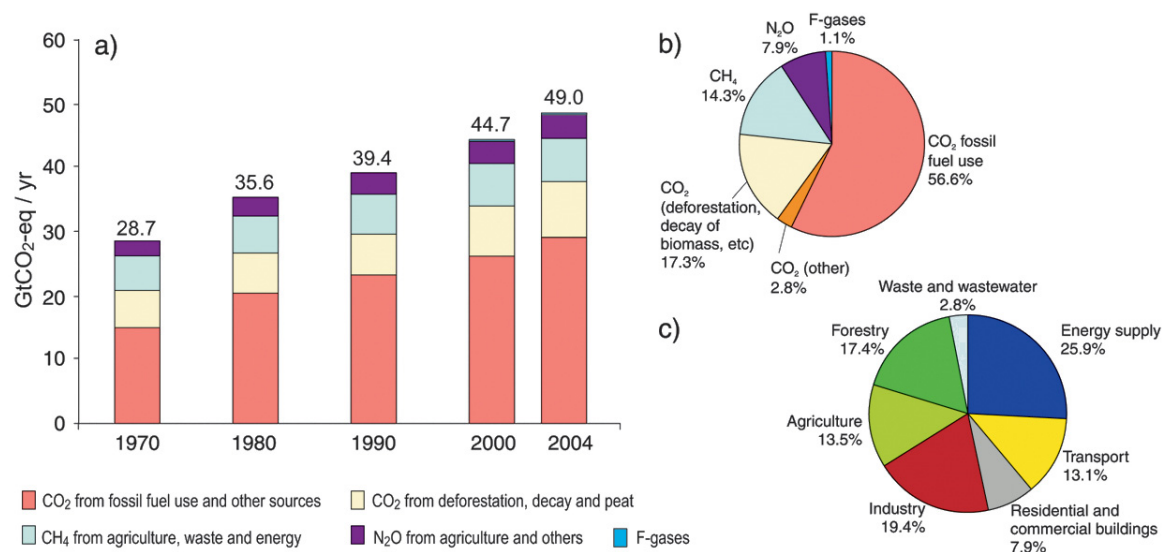


Figure 1.1: (a) global annual emissions of anthropogenic GHGs emission (b) Share of different anthropogenic GHGs in total emissions 2004 (c) share of different sectors in 2004 in terms of  $\text{CO}_2$ -eq [1]

Rising energy demand based on globalization, industrial food production, economic growth and extended mobility requisition all over the world is highly responsible for a consistent increase of anthropogenic GHGs in the atmosphere. It is very likely that the rise of their atmospheric concentration is profoundly responsible for the exaltation of the global mean temperature especially tak-

<sup>1</sup> Changes in the atmospheric concentrations GHGs and aerosols, land cover and solar radiation alter the energy balance of the climate system, they affect the absorption, scattering and emission of radiation within the atmosphere and at the earth's surface. The resulting positive or negative changes in energy balance due to these factors are expressed as radiative forcing and define the relative changes to preindustrial conditions defined at 1750 and are expressed in Watts per square meter  $\text{W}/\text{m}^2$  [1].

ing carbon dioxide into account. Observations of the global temperature distributions, the averaged sea level as well as the snow cover in northern and southern hemisphere as presented in Figure 1.2 have shown definite evidence for a global change in climate conditions. The smoothed curves represent averaged values while marked as circles are annual values all set into differential relation to corresponding averages from 1961-1990 on the left ordinates.

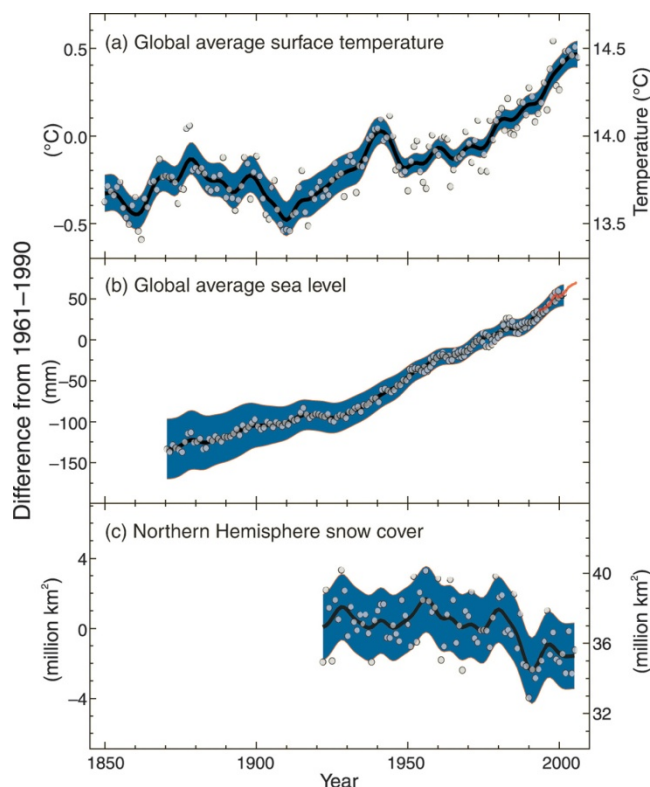


Figure 1.2: Observed changes in (a) global average surface temperature, (b) global average sea level, (c) northern hemisphere snow cover for March-April [1]

A relation between the progressing concentration of GHGs in Figure 1.1 and the observed ascent of atmospheric temperature is obvious especially focusing on the tendencies from the 1970s till now referring to [1]. There are several scenarios existing for future development of the atmospheric temperature gradient, all including a mild to severe progress of averaged temperature level depending on the global GHG emissions. Each of these emission scenarios immanent is an alternation of climatic conditions resulting in increased flooding risks, drought in other regions resulting in famine, wildfire, ocean acidification affecting the ecosystem in the sea due to higher  $\text{CO}_2$  concentration, extinction of plant and animal species that are sensitive to temperature and climate changes. Also a rise of the averaged sea level is part of these prognoses which has an increased salinisation of groundwater resources as a consequence, as well as a critical affection of low lying coastal areas, islands and delta areas.

Due to global development of industry, the mobility sector and individual energy consumption a categorical prevention of these affection towards environment based on the production of GHGs is nonrealistic. However drastic mitigation of this predicted alternation in climate conditions is possible and inevitable. Several global research and development projects on sustainability have been introduced in the last decades especially for the mobility sector. These are mainly focusing

on energy efficiencies of engines, turbines and power plants as well as alternative and sustainable fuel resources. The mobility sector is divided into individual mobility (cars, motorcycles), heavy goods vehicles, railway, navigation and aviation. Regarding to this contribution the attention is directed towards the aviation sector.

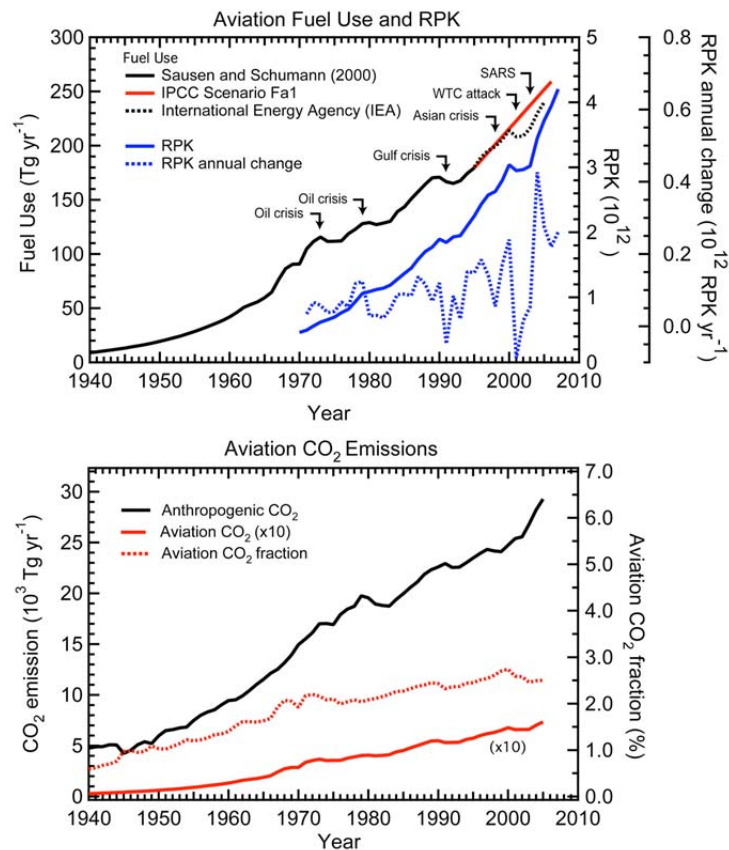


Figure 1.3: (top) Fuel usage and Revenue Passenger Kilometers (RPK) from 1940 to 2007, (bottom) corresponding CO<sub>2</sub> emissions total anthropogenic and aviation related [2]

The overall emissions of CO<sub>2</sub> from aviation were denoted with 2,7 % of the global total fossil fuel emissions in 2000. whereas 21 % of the total emissions had been produced by the global transportation sector. as a consequence 12 % of the fossil CO<sub>2</sub> emissions by transportation were due to aviation [2]. Figure 1.3 (top) shows the global aviation fuel usage since world war II indicating revenue passenger kilometers and its growth rate in RPK per year. Arrows represent global crisis events that potentially influenced air traffic. Figure 1.3 (bottom) presents the evolution of anthropogenic CO<sub>2</sub> emissions opposed to aviation emissions and its fractional curve. Referring to this diagram it can be gathered that the growth rate of aviation based CO<sub>2</sub> emissions is lower than the total anthropogenic CO<sub>2</sub> emissions growth rate. Aviation induced radiative forcing is pre-

sented in Figure 1.3. Sequentially each GHG component is listed with its ratio of RF (values). The error bars represent a 90 % confidence interval and LOSU stands for level of scientific understanding. As it can be deduced from this graphic not only carbon dioxide but also nitrous oxides as well as linear contrails are significantly involved in total aviation induced radiative forcing. CO<sub>2</sub> emissions can be reduced basically by increased efficiency of turbines and the usage of sustainable energy resources, which also affects NO<sub>x</sub> production. Due to the different production mechanisms (thermal NO<sub>x</sub>, prompt NO<sub>x</sub> and fuel NO<sub>x</sub>. for further explanation refer to literature) a reduction cannot be easily realized and needs further investigations taking combustion management and exhaust gas treatment as well as its role in chemically reducing other long lasting GHG components such as methane into account.

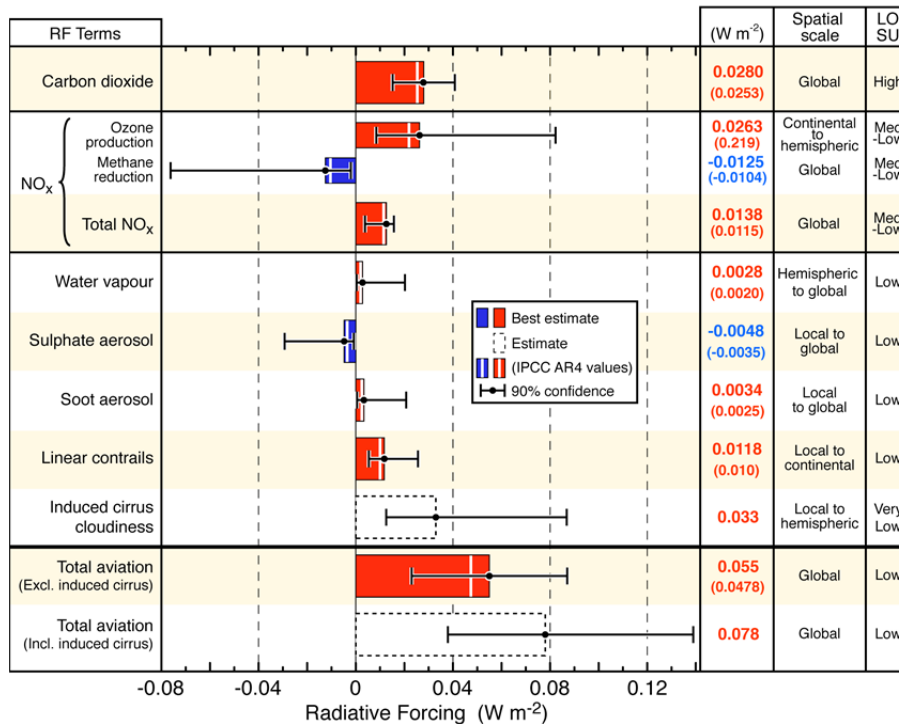


Figure 1.4: Aviation induced radiative forcing components and their RF amount in W/m<sup>2</sup>. negative (blue) / positive (red) [2]

Derived from several future projections for aviation induced fuel consumption respectively CO<sub>2</sub> emissions a trend towards an air traffic growth rate of approximately 4 to 5 % per year meets the global consensus in forecast models. As a consequence air traffic will double within the next 20-25 years. Even considering an annual improvement in fuel efficiency of 2% per year results in a quadruplication of the momentary fuel consumption till 2050 [2]. IATA (International Air Transport Association) set the goals for CO<sub>2</sub> emissions till 2050 to a reduction of at least 50 %. This will only be possible by introducing new innovative technologies using biofuels including neutral Land Use Change (LUC) influences and an improved air traffic management.

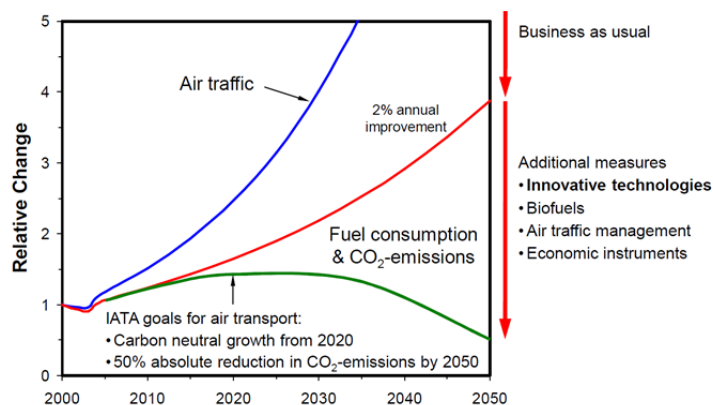


Figure 1.5: Actual and predicted aviation induced CO<sub>2</sub> production including model based air traffic growth. business as usual including a 2% annual improvement in fuel consumption (red), IATA goals for carbon neutral growth till year 2050 (green) [3]

While NEWAC had focused mainly on new innovative technologies reducing greenhouse gases, European commission's seventh frame work program (FP7) also introduced a research and development project with its attention directed towards the drop in compatibility of existing alternative and bio fuels called ALFA BIRD (**AL**ternative **Fuels** **And** **BI**ofuels for ai**R**craft Development).

This contribution has been produced in the frame of this project. The ALFA BIRD consortium is made up of several industrial partners, research and educational institutions on aeronautics as well as oil companies and aims to investigate the adaptability of conventional aircraft engines to the use of alternative fuels such as GTL, CTL, Naphtenic Cut and blendings of GTL with HVO (Hydrogenated Vegetable Oils). Due to the very long lifetime of current civil aircraft and because of very strict operational constraints (e.g. flight in very cold conditions) it is a great challenge to use bio-fuels and alternative fuels in aircrafts. The main objectives of this project were an identification of the most probable alternative fuels to kerosene in terms of production, economics and technologies from well to tank, the investigation of the adequacy of the selected ones, an evaluation of the environmental and economical performance of those and finally the creation of a future perspective for the industrial use of the "best" alternative. The Institute of Thermal Turbomachinery and Machine Dynamics (ITTM) at the TU Graz participated in Subproject 2 and 3 (SP2/SP3). For SP3 a literature survey facing existing technologies concerning combustor designs and research publications dealing with alternative and biofuels had been conducted. This part represents chapter 2. In the frame of SP2 an analysis of the evaporation and atomization of the chosen fuel types had been performed in cooperation with Onera Fauga Mauzac, who focused on the atomization. For this purpose a versatile test rig had been installed in the combustion laboratory of the ITTM.

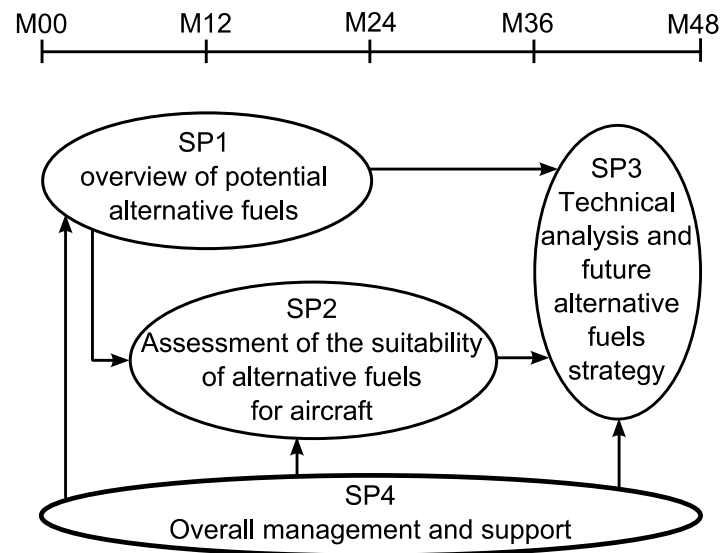


Figure 1.6: ALFA BIRD Project structure year 1 – 4

The work related to this contribution included the installation of a new fuel supply system, the design of a combustion chamber using an existing burner geometry owned by TURBOMECA and the design and construction of an afterburner in order to reduce unburned Hydrocarbons produced by an isothermal evaporation analysis. Representing a measurement technique to detect the fuel vapor phase gradients in the primary zone of the radial swirl combustor the infrared extinction

method (IRE) had been applied. This technique had to be adapted to the laboratory surrounds and combined with an automation system. Preliminary investigations using the IRE were published. Finally an isothermal evaporation analysis had been performed, the results evaluated and compared to the atomization investigations of ONERA. The results had been identified as comparable to the mechanisms and tendencies from other investigations. The main outcome of this work is that concerning existing combustor geometries the chosen fuels had been found adaptable. The measurement results show similar vapor distributions for all tested fuel samples, slight divergencies in the gradients are assumed to derive from the measurement as well as the test setup uncertainty. Recommendations for future works with this kind of measurement technique and combustor surroundings consist of an improvement of the stability of the used data acquisition system, especially the diodes and the adaptation of the technique towards the principle of the combustor type in order to avoid zones of extinction in the boundaries due to recirculation.

# Chapter 2

## Fuels

### 2.1 Initial selection

Workpackages of the partner institutions in Subproject 1 (SP1) of the Alfa Bird Project, as presented in Figure 1.6 consisted of a selection and characterization of possible alternatives to conventional jet fuel [45]. This procedure had been divided into two several passages. Within the first passage the existing market situation had been analyzed and possible fuels identified and investigated. All of these have been distinguished by their chemical derivation namely:

- Fatty Acid Esters (FAE)  
*derive mainly from vegetable oils and are converted by a trans-esterification process into a less viscous oil. Future derivation: Oil from algae and non-alimentary plants*
- Alcohols for fuel purpose  
*are produced by a fermentation process of corn and sugar cane. Future derivation: from cellulosic biomass derived from forestry and agriculture for non-food uses.*
- Synthetic Fuels  
*are predominantly produced by a Fischer Tropsch synthesis using synthesis gas derived from coal and gas and post processed by cracking and isomerization process. Future derivation: Biomass and new feedstocks such as algae*
- Hydrotreated Oils (HO)  
*can be converted from domestic oils animal fats and cheaper vegetable oils by a hydrogenation process resulting in straight chain hydrocarbons C12 – C18. Future derivation: Oil produced from algae*
- Naphtenic compounds  
*are produced by a liquefaction process of coal. Future derivation: biomass*
- Succinic acid derivatives  
*Are extracted by a special sugar fermentation procedure and a following reaction with ethanol that results in diethyl-succinate (DES). Future derivation: biomass*
- Furane derivatives  
*Are produced by fermentation of carbohydrates such as sugars and starch. Glucose is then converted into furanic products. Future derivation: biomass*

An overview of the typical properties (positive and negative) of the most promising liquids such as Fatty Acid Methyl Ester (FAME), Ethanol, higher alcohols, Hydrogenated Vegetable Oils (HVO) and Gas, Coal and Biomass To Liquid fuels (GTL, CTL, BTL) is presented in Table 2.1.

Table 2.1: Main advantages and drawbacks of several alternative fuels (drop-in routes) for Jet fuel [45] modified

	Advantages	Drawbacks
<b>FAME</b>	Price Availability Large production plant investments Lubricity	Density Viscosity Can absorb water during storage Heating value Stability Cold flow properties
<b>Ethanol</b>	Cold flow properties	Flash point Heating value Water solubility
<b>High alcohols</b>	Flash point Heating value Cold flow properties	Availability Investment cost
<b>HVO</b>	High quality (stability)	Cold flow properties, lubricity Availability, investment cost Dependency on feedstock (oil composition)
<b>GTL</b>	High quality (stability) Already available	Price
<b>CTL</b>	High quality (stability)	Must be imported, price
<b>BTL</b>	High quality (stability)	Process not ready (impurities, cost...), few production plant investments

Based on multiple criteria for the selection of alternatives to kerosene mainly influenced by production efficiency, availability on the fuel market, price and physical and chemical requirements, such as heat value, flash point, water solubility, cold flow properties, ignition delay and lubricity the most promising molecules have been chosen and put into blends with FTSPK due to their compositions being outside the boundaries for jet fuel specification. As a reference fuel fully synthetic jet fuel (FSJF) from Sasol (CTL) had been chosen. This type of fuel is further discussed in 3.2.8 and is certified in ASTM (American Society for Testing and Materials) standards as replacement fuel for the use in jet engines. JET A1 was neglected as reference fuel due to its regional refinery based differences in quality and chemical composition especially regarding to the aromatics and sulphur content. This identification process initiated by research partners from Shell global, IFP and Sasol resulted in a primary selection of 12 possible fuel alternatives towards Kerosene Jet A1 presented in Table 2.2.

Table 2.2: Selected alternative fuel samples WP1.2 [45] modified

Fuel number	Fuel Reference number	Description (volume % blends)
1	8040	CTL from Sasol
2	8289	GTL from Shell
3	8286	GTL + 50% Naphtenic cut
4	8290	GTL + 20% Hexanol
5	8087	GTL + 20% Furane
6	8088	GTL + 30% FAE
7	8089	GTL + 30% Furane
8	8090	GTL + 50% HVO
9	8091	GTL + 75% HVO
10	8092	GTL + 10% FAE
11	8093	GTL + 10% Furane
12	8094	GTL + 20% FAE

The next step within WP1.2 was to test these chosen compounds against the industry jet fuel specification ASTM D7566 for Jet A1 and Synthetic Paraffinic Kerosene (SPK), which includes mainly the following restricting properties [46]:

- An aromatic content between 8% and 25% volume fraction
- A Jet Fuel Thermal Oxidation Test breakpoint (JFTOT) of  $\geq 325^{\circ}\text{C}$
- Density between  $730 \text{ kg/m}^3$  and  $770 \text{ kg/m}^3$
- And others

These tests have been performed by Shell Global Solutions. Most of the chosen fuel samples failed the test standard boundaries of the above mentioned criteria especially for the aromatic content, which is responsible for lubricity and the seal swelling performance. Blends of FAME and HVO failed due to low temperature viscosity limits and total acidity requirements.

This experimental investigation lead to a final fuel matrix of only four interesting blends namely CTL GTL and blends of GTL with 50 % naphtenic cut and GTL with 20% hexanol (fuel number 1-4 in Table 2.2). All following investigations in the frame of this research project have been performed using these 4 blends.

## Chapter 3

# Existing Technologies and Investigations

### 3.1 Emissions and low-emission technologies with conventional fuels

#### 3.1.1 Specifications of a Gas Turbine (GT) combustor

State-of-the-art GT technology, plus external factors such as discussed before show how numerous the constraints are for the combustion engineer who has to design a new system. The many parameters are summarised in Figure 3.1. The combustor is a complex system, it results from a multitude of compromises, and requires an extensive and expansive trial-and-error session before being validated. The main problem is that precise combustion research often requires full-scale experiments, since many parameters such as thermochemistry at given (p, T) conditions have to be simulated at scales specific to the flow.

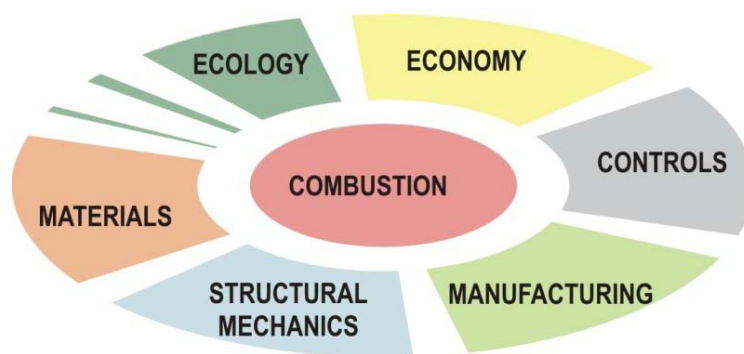


Figure 3.1: Technical and external constraints for GT combustor design.

The eleven specifications for combustor design that follow were prescribed by Lefebvre more than 30 years ago [1]. They are still up-to-date. These are the baseline rules for advanced combustion management.

1. High combustion efficiency: Combustion efficiency ( $> 99.9\%$  at design point) achieves quasi 100% on all modern combustors at cruise. Combustors with efficiencies of less than 90% anywhere else on the operation envelope are unlikely to be tolerated [5].
2. Reliable and smooth ignition (no detonation): Ignition is usually performed with help of high-energy sparkplugs. Ignition difficulties at cold start are similar to the ones met with internal combustion engine, with the risk to spray too much kerosene before the flame starts, and the resulting risk of detonation. Civil aeroengine combustors are also designed to ignite at windmilling condition in case of emergency, where the pilot manages to keep up the required speed with the still active engines, or speeds up in a descent manoeuvre to recover the minimum air inlet velocity necessary to maintain the fan in rotation (windmilling), compress the air, and achieve the right temperature for auto-ignition. Ignition at extremely cold temperatures for helicopters that landed at high altitudes in the mountains,

as well as emergency re-ignition for combat airplanes at high altitudes (10-20 km) where the air is extremely thin are also important issues of R&D.

3. Wide stability limit (over the whole operation range): Stability is here meant in the sense of flammability, or pushing the flame blow out limits well beyond the engine's operation.
4. No combustion instability: where stability means steady-state flame, and instability is often of aero-thermo-acoustic origin.
5. Low pressure loss between compressor and turbine: The pressure loss of the liner varies from 3 to 5%. If losses in the diffuser are to be minimised, a minimal value is required to maintain turbulence in the liner (jet swirls and cooling jets).
6. Cooling air: The reduction of the amount of combustion chamber cooling air (currently about 1/3 of the main air) has an influence on the overall efficiency. Less cooling air tends also to a lower overall pressure loss. However, augmenting the pressure ratio for future designs result also in augmenting the combustor entry temperature, which acts against the cooling effectiveness.
7. Deliver the ideal gas temperature at the turbine inlet: Temperatures up to 2500K are achieved in the primary zone at full load, cooled down to 2000K in the dilution zone before reaching the turbine's first guide vanes. Temperature gradients, as well as unsteady temperature fluctuations, augment the fatigue of the parts at turbine entry. The Overall Temperature Distribution Factor (OTDF) is the ratio of the difference between peak and mean temperature right before the plane of the HP turbine Nozzle Guide Vane (NGV). OTDF should be controlled to be less than 50 %. The Radial Temperature Distribution Factor (RTDF) is analogous to OTDF but uses circumferentially averaged temperature values. RTDF should be controlled to be less than 20 % [5].
8. Low emissions, no unburned hydrocarbons, no soot: The problem on emissions is that they are conflicting with each other.  $\text{NO}_x$  appear at high temperatures and long residence times, at near-stoichiometric conditions. UHCs, soot and CO appear at extreme lean or rich combustion. Since it is not feasible to achieve low levels of  $\text{NO}_x$ , UHCs and CO at once, an acceptable compromise has to be found.
9. Ease of maintenance: The maintenance shall be performed on time intervals greater than 10,000 hours of operation on power turbines. The parts shall be easily accessible and disposable.
10. Integration aspect in comparison with the other turbine elements: This is less a problem for industrial GT where notions of size and volume are flexible. For aeroengines, the dimensions and weight of the combustor have to be optimised.
11. Lifetime - durability: A modern aeroengine is designed to operate up to 50 years.
12. Multifuel capability: This was meant originally for stationary gas turbines, but can be extended to aviation using biofuels.

### 3.1.1 Target emissions to be reduced

GT combustor designers put a very strong effort on reducing the impact on the environment of their machine while improving constantly their efficiency (taken separately, the notions efficiency and low-emissions may often be conflicting). Table 3.1 summarises the pollutants involved in aviation and their probable impacts on climate change [6]

Table 3.1: Species contributing to climate and ozone change. [6] modified

Emitted Species Role and Major Effect on Atmosphere			
CO <sub>2</sub>	<b>Troposphere and Stratosphere</b>		
	Direct radiative forcing	→ warming	
H <sub>2</sub> O	<b>Troposphere</b>		
	Direct radiative forcing	→ warming	
	Increased contrail formation	→ radiative forcing	→ warming
	<b>Stratosphere</b>		
	Direct radiative forcing	→ warming	
	Enhanced PSC formation	→ O <sub>3</sub> depletion	→ enhanced UV-B
	Modifies O <sub>3</sub> chemistry	→ O <sub>3</sub> depletion	→ enhanced UV-B
NO <sub>x</sub>	<b>Troposphere</b>		
	O <sub>3</sub> formation in upper troposphere	→ radiative forcing	→ warming
		→ reduced UV-B	
	Decrease in CH <sub>4</sub>	→ less radiative forcing	→ cooling
	<b>Stratosphere</b>		
	O <sub>3</sub> formation below 18-20 km	→ reduced UV-B	
	O <sub>3</sub> formation above 18-20 km	→ enhanced UV-B	
Enhanced PSC formation	→ O <sub>3</sub> depletion	→ enhanced UV-B	
SO <sub>x</sub> and H <sub>2</sub> SO <sub>4</sub>	<b>Troposphere</b>		
	Enhanced sulfate aerosol concentrations		
	Direct radiative forcing	→ cooling	
	Contrail formation	→ radiative forcing	→ warming
	Increased cirrus cloud cover	→ radiative forcing	→ warming
	Modifies O <sub>3</sub> chemistry		
<b>Stratosphere</b>			
Modifies O <sub>3</sub> chemistry			
Soot	<b>Troposphere</b>		
	Direct radiative forcing	→ warming	
	Contrail formation	→ radiative forcing	→ warming
	Increased cirrus cloud cover	→ radiative forcing	→ warming
	Modifies O <sub>3</sub> chemistry		
	<b>Stratosphere</b>		
Modifies O <sub>3</sub> chemistry			

The environmental issues for a combustor aim primarily at reducing the CO<sub>2</sub>, NO<sub>x</sub> and CO emissions, and at a secondary level at reducing noise. Table 3.2. shows the typical emission index for aeroengines of the 90's [6]. These are repeated in Figure 3.2.

Table 3.2: Typical emission index (g/kg) levels for engine operating regimes. [6]

Species	Idle	Take-Off	Cruise
CO <sub>2</sub>	3160	3160	3160
H <sub>2</sub> O	1230	1230	1230
CO	25 (10-65)	1	1-3.5
HC (as CH <sub>4</sub> )	4 (0-12)	0.5	0.2-1.3
NO <sub>x</sub> (as NO <sub>2</sub> )			
- Short Haul	4.5 (3-6)	32 (20-65)	7.9-11.9
- Long Haul	4.5 (3-6)	27 (10-53)	11.1-15.4
SO <sub>x</sub> O (as SO <sub>2</sub> )	1.0	1.0	1.0

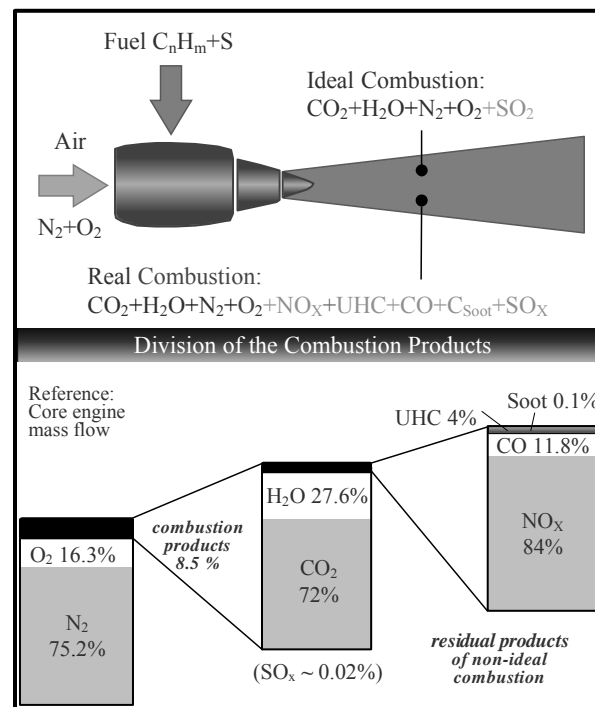


Figure 3.2: Schematic of ideal combustion products (top), and all existing combustion products. [6] modified

### 3.1.1.1 Carbon dioxide CO<sub>2</sub>

The production of CO<sub>2</sub> is specific to the average carbon contents of the fuel (this explains why natural gas is favoured as a "low-emission" fuel since its main component is methane CH<sub>4</sub>, having thus the lowest carbon content in the alkane group). It is also proportional to the specific fuel consumption (TSFC), so that reducing CO<sub>2</sub> emissions means increasing the overall efficiency. In other words, it means saving fuel for providing the same thrust. This parameter is therefore a major sales argument.

The CO<sub>2</sub> represents 77% of total anthropogenic GHG emissions in 2004 (74% in 1990). Radiative forcing of CO<sub>2</sub> predominates over all other radiative forcing agents [8]. It results from the continuous increase in atmospheric CO<sub>2</sub> concentration caused by human activities since the preindustrial era.

### 3.1.1.2 Nitrate oxides NO<sub>x</sub>

The NO<sub>x</sub> emissions (generic term for nitrate oxides such as NO, NO<sub>2</sub>, N<sub>2</sub>O etc., where NO dominates by 95 %, followed by NO<sub>2</sub> with approximately 4.9 % and traces of the other species) contribute to the GHG formation at ground level and to the ozone layer depletion at high altitude. They represent 7.9% of the yearly emitted GHG emissions, and are classified third after methane (14.3 %) and CO<sub>2</sub> (77 %). They represent up to 0.01% of the mass flow of the exhaust gases of a classical GT core [6]. They mainly result of the reaction of dissociated air nitrogen in the reaction zone (thermal NO<sub>x</sub>). The higher the temperature, the longer is the residence time and the larger the NO<sub>x</sub> concentration.

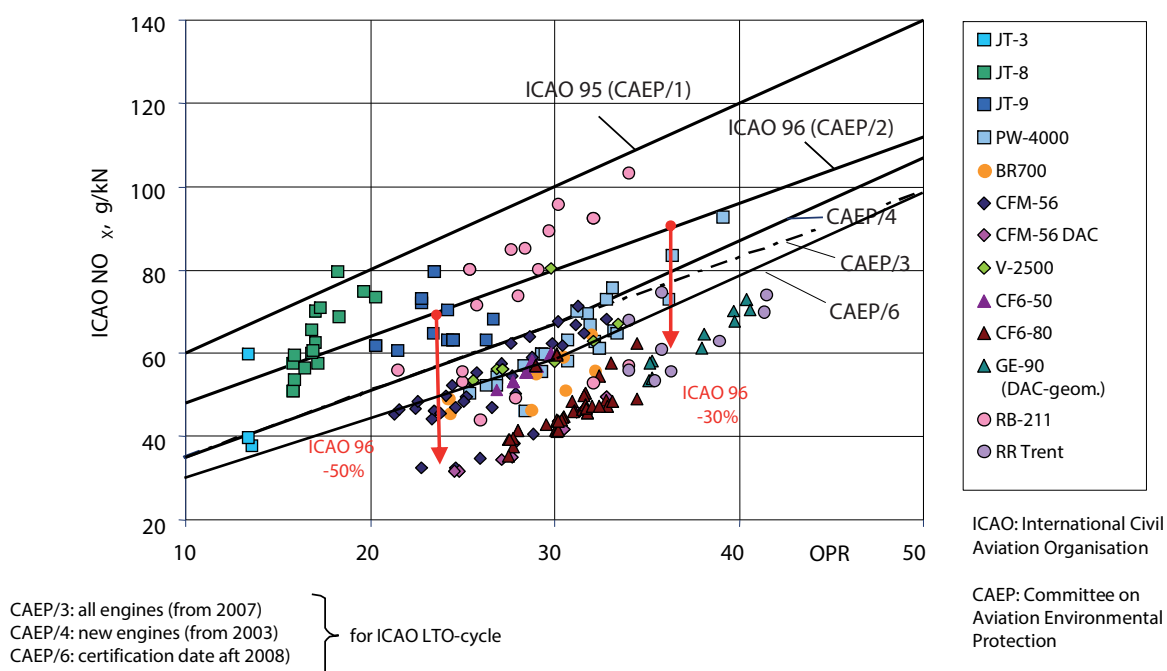


Figure 3.3: ICAO-CAEP target emission levels [9] in the medium and long term, and some existing engines

Figure 3.3 shows the limits fixed for NO<sub>x</sub> emissions at ICAO-LTO cycle (Landing and Take-off cycle, as defined by the ICAO), for several certified engines parameterised over OPR. Note that the admissible NO<sub>x</sub> level augments with the OPR, since higher engine operating pressure ratios (OPR) such as for transatlantic flights, are involved resulting in a larger NO<sub>x</sub> production. Modern land-based gas turbines aim at NO<sub>x</sub> values below 20ppm, ultra low NO<sub>x</sub> means below 5ppm.

### 3.1.1.3 UHCs and soots

Unburned hydrocarbons (UHC) and soots (or smoke) result from a poor combustion respectively at extremely lean and rich conditions. Hence, they degrade the combustion efficiency. Furthermore,

they fall in the GHG class. They are normally associated with poor atomization, inadequate burning rates, the chilling effect of film-cooling air or any combination of these. These emissions take place in principle at part load. Typically, liquid-fuelled combustors produce more of these emissions than gas-fuelled GT combustors at similar thermal power.

They provoke health problems when accumulated in confined atmospheres since these are submicronic particles with high aromatic contents.

#### 3.1.1.4 Carbon monoxide CO

CO emissions also results from a poor combustion respectively at extremely lean and rich conditions. It is a potential fuel since it can be further oxydized to CO<sub>2</sub>, hence degrade the combustion efficiency when produced. It results from inadequate mixing of fuel and air, inadequate burning rates in the primary combustion zone or insufficient residence time because of a too sudden air injection quenching.

It is highly toxic, provoking rapid suffocation when unnoticed because of its odourlessness and colourlessness. Special security measures are to be taken when working with GT combustion in a confined atmosphere.

Note that CO and UHCs have a similar growth rate when operating at extremely rich or extremely lean conditions, whereas NO<sub>x</sub> appear mostly near stoichiometry. It is therefore not possible to reduce all emissions at once, so that a compromise has to be found.

### 3.1.2 Combustor architectures

Figure 3.4 is a synthesis of the main designs of combustors found on current systems, summarising the potential of different Low-NO<sub>x</sub> strategies as seen at the end of the 90's. Gas turbine Low-NO<sub>x</sub> systems started to be studied about 30 years ago during the 70's (e.g. early works on RQL technology of Pierce et al, 1980, as reported in Smith et al., 1991). Low-NO<sub>x</sub> concepts are compared to the conventional combustor, and estimates of NO<sub>x</sub> reduction are drawn. The colours show the domain of operation of each concept, for instance in the rich and lean domain for the Rich-burn/Quick-Quench/Lean-burn (RQL) burner, or lean combustion with the lean premixed pre-vaporized concept (LPP).

The Research & Development effort was strongly enhanced beginning of the 90's, with the introduction on the market of low-emission burners on ABB, GE and SIEMENS land-based machines, as well as the introduction of double-annular combustors (DAC) on turbofans during that decade.

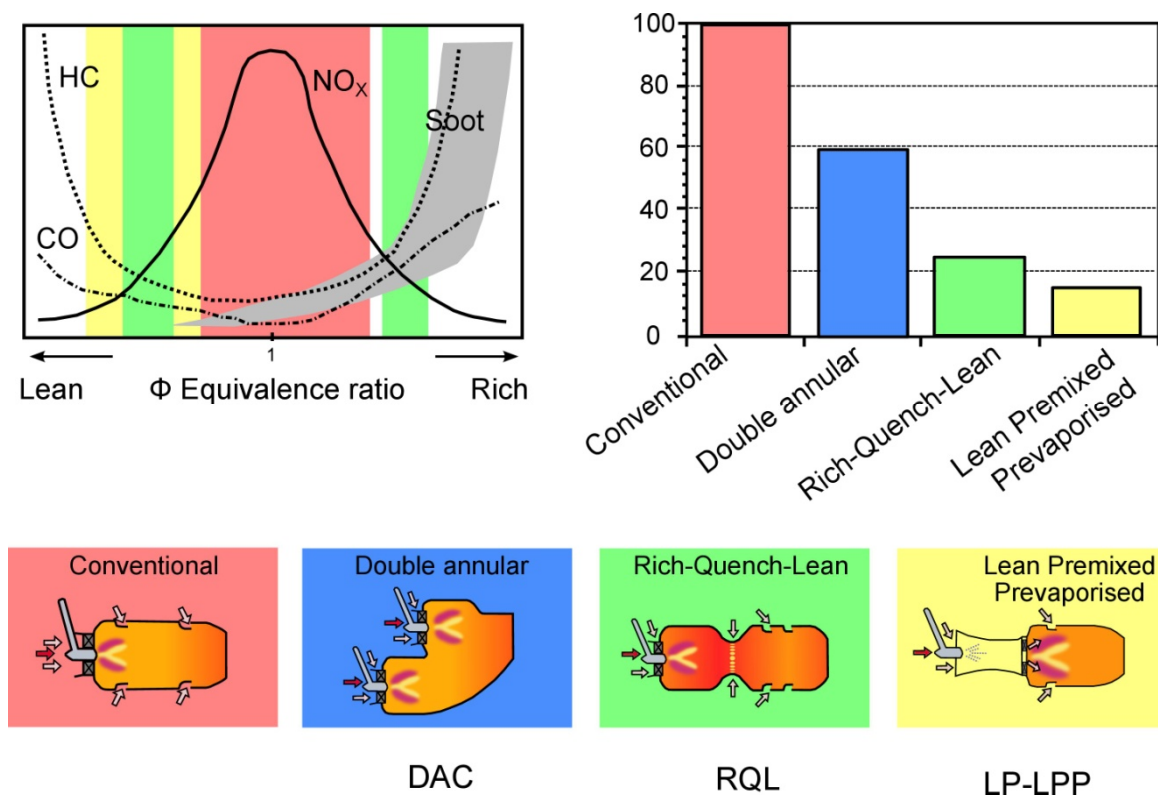


Figure 3.4: Different combustor constructions to reduce NO<sub>x</sub>, [11] modified

### 3.1.2.1 The conventional combustor

This is the most represented architecture in current civil aviation. The conventional combustor combines an air-blast injection system to an annular combustor geometry, see Figure 3.5 with near-stoichiometric combustion in the primary zone (Φ near 0,8).

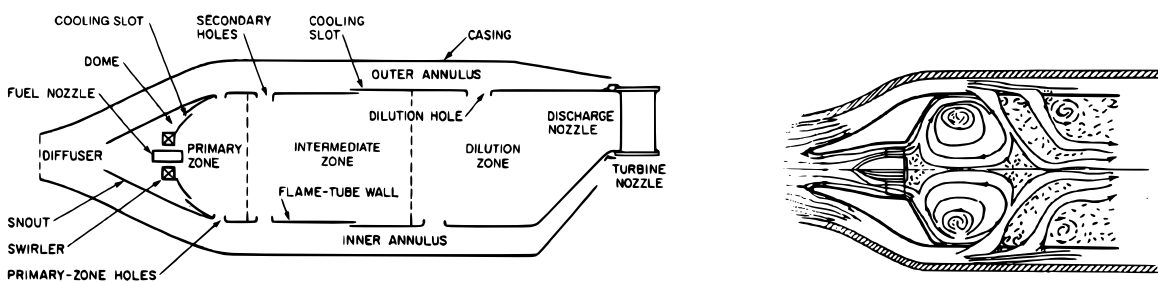


Figure 3.5: Conventional aero engine annular combustor (left), with the suggested air flow streams (right) [4].

The injector of the air-blast type became a standard injection system during the 70's (works by Lefebvre, 1989) and complemented the pressure nozzle injection, ensuring a refined spray, by taking advantage of the aerodynamic forces of the injection. Figure 3.5 right summarizes the aerodynamics of the injection, where fine atomization takes place in the mixing layer between two swirled flows at the tip of the injector, and the flame stabilizes around the internal recirculation zone. A mechanical flame holder is therefore not required.

In comparison with older combustor designs comprising can combustors or turbo annular architectures and pressure nozzles for injection, they are reduced to the status of traces, and there is much less black smoke plume at the tail of modern jets. Combustion is steady, and the thermal efficiency is high.

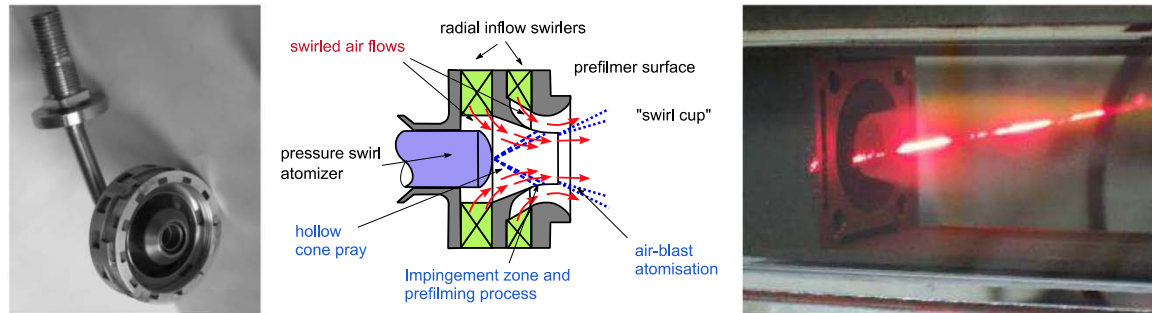


Figure 3.6: Air blast atomizer. Left: air-blast picture (standard industrial system). Centre: principle of air-blast atomization. Right: laboratory air blast injector under operation at the DLR Cologne spray test rig, using laser diagnostic methods (here: infrared absorption for fuel vapor measurement) [13]

### 3.1.2.2 Staged combustion

The idea is to split up the flame into several "sub-flames" that can be controlled separately. As a result, more flexibility on their respective power is achieved and the operation can be optimized. It often consists in a pilot flame burning at near stoichiometric conditions that maintains combustion and ensures part load operation, and a main zone with lean combustion that provides the thermal power at full load. Figure 3.4 shows the DAC concept (Double-Annular Combustor).

Reducing and distributing the single burners results in smaller residence time for  $\text{NO}_x$  formation, combined with the operation at lean conditions resulting in up to 40%  $\text{NO}_x$  reduction compared to a conventional combustor. However, the added complexity of this staging has made some engine manufacturers investing to come back to a single annular combustor (SAC) geometry where the split is placed in the injector itself (e.g. TAPS concept: twin annular premixing swirler). The commercial introduction of the CFM56 with first generation DAC was not a commercial success (more expensive, more maintenance costs), but the second generation GE90 and CFM were more successful. This technology is successfully in operation since about 10 years.

### 3.1.2.3 Rich-burn/Quick-Quench/Lean-burn (RQL)

This is the third Low- $\text{NO}_x$  concept with target emission reduction more than 50% in comparison to the emissions of the conventional burner. A rich mixture is injected, and rich combustion takes place in the combustor dome, ensuring the combustion robustness. After that a secondary injection of air takes place, quenches the flame and lean combustion takes place downstream, providing most of the thermal power.

The drawback is a higher production of soot in comparison with the conventional burner. RQL technology was successfully commercialized (e.g. the TALON burner flying with the PW6000).

#### 3.1.2.4 Lean premixed prevaporized (LPP)

The last Low-NO<sub>x</sub> concept of Figure 3.4 is the most promising in terms of NO<sub>x</sub> emission reduction (more than 70%). The LPP burner aims to achieve the characteristic of a well-stirred reactor while being fed with liquid fuel, and this at lean operation to minimize NO<sub>x</sub> production. It consists of a classical air-blast system and of a premixing tube where fuel vaporisation and mixing take place.

The lean operation is set at an equivalence ratio such that NO<sub>x</sub> emissions are strongly reduced, while attention is paid that the thermal efficiency is not too affected (the effect of lower flame temperature is partly compensated by energy savings due to a lower need in cooling air), that the CO and UHC emissions remain low, and that the blow-out limit stays away from operational bandwidth. However, the greater transit time of the reactants between injection nozzle and flame front favors the couplings between turbulence and acoustic, facilitating the appearance of combustion instabilities. This is the main drawback of this concept that retarded its industrial use.

### 3.1.3 Other parameters of importance

#### 3.1.3.1 Ignition

Classical ignition in gas turbines implies a high energy sparkplug flush-mounted on the liner in the primary zone, typically positioned perpendicular to the injector at a depth where the fresh reactants meet the wall.

Attention is to be paid that ignition is successful within a short ignition sequence, to avoid the risk of detonation. Under some conditions, ignition is to be dimensioned to operate a cold start such as in the case of a helicopter starting from a high mountain during a rescue mission. The fuel specifics as well as the combustor architecture are the main parameters. See the works by Lang et al. 2010 on this topic.

#### 3.1.3.2 Self-ignition and altitude relight

Two aspects concern self-ignition. The first one is where self-ignition is unwished, for instance self-ignition is the limiting parameter in the dimensioning of a premixing tube of a LPP injector. If the transit time of the fresh reactants exceeds the critical auto-ignition delay  $\tau$  the flame might ignite within the tube and flash-back towards the fuel nozzles, settle there and create a diffusion flame that will irremediably destroy the injection module.

Self-ignition is wished for altitude relight under windmilling conditions. If an engine of an aeroplane is incidentally turned off, the aeroplane dives to achieve a characteristic velocity so that the fan is entrained by the incoming air, air is compressed, and the temperature and pressure in the combustor are favourable for auto-ignition, enabling the relight.

The main parameters for self-ignition are the inlet temperature and pressure (about 700K for conventional Jet A1 at standard pressure). Typical self-ignition delays at full load are of the order of 10 ms.

Reference correlations on self-ignition of conventional fuels have been done by Spadaccini & Tevelde (1982) [18] and, more recently, by C. Guin (1999) [19].

### 3.1.3.3 Lean blow-out limit

The lean blow out limit (LBO) is the limit of the operational domain in the lean domain, usually expressed as a function of the thermal power versus equivalence ratio. It is also specific to the inlet conditions (pressure, temperature, reference inlet velocity and swirl number), and requires a characterization under realistic conditions.

Operation near the LBO limit is not recommended, since CO and UHC emission rise because of the low flame temperature combined to the strong flame dynamics, resulting in incomplete combustion. The flame also fails to anchor properly and tends to deform and follow bubbles of hot gases in the flow. When this dynamic becomes too strong, the flame does not return towards the fresh reactants and blows out.

The determination of the LBO limit is important in determining the domain of flammability and assessing where stable combustion is guaranteed. See the works of Thomas Doer et al. on this topic.

### 3.1.3.4 Combustion instability

Higher pressure ratios tend towards small combustor architectures with elevated pressure density. The stability of the flame is therefore a critical parameter. The flame shall ideally remain along a confined volume, so that the thermal load on the combustor components is evenly distributed.

Combustion instability implies a mechanism of thermo-acoustics. The natural resonant frequencies of the cavities of the combustor couple with the unsteady heat release and possibly with the flow dynamics, resulting a noisy and extremely dynamic flame, with the increased risk of flashback, blow-out and structural damage. Combustion instabilities have been a major concern in gas turbine combustor design over the last 20 years.

Low-NO<sub>x</sub> systems implying lean combustion and premixing are particularly sensitive to this problem, since they imply characteristic times (e.g. premixing) that favour the interaction between flow turbulence and fuel mixing. Lean flames are known to be extremely sensitive to turbulence and equivalence ratio fluctuations. The dimension of the main zone of the burner is also typically larger since about 2/3 of the total air are usually implied in combustion and pass through the injector. This favours a larger panel of resonant frequencies in the axial and tangential directions. Concerning the fuel itself, the characteristic times that play a role in combustion instabilities are related to the atomization, the vaporisation and the vapor diffusion. See the works by Giuliani (2010) on this topic [13].

### 3.1.3.5 Atomization quality

Lefebvre (1989) did extensive works on air-blast atomization, an injection technology that has become a standard in turbo-machinery, benefiting of the aerodynamic stress exerted by fast-flowing turbulent air on the injected fuel and resulting in a refined spray. Combined to a swirl-stabilized flame structure, this burner offers a robust flame that is compact, benefits from a heat-up of the reactants because of the central recirculation zone it generates, and produces little soot.

The rheology of the fuel determines the atomization quality. Important parameters are among others the Weber number (particle inertia versus surface tension) and the Morton number (particle viscosity versus surface tension). The favoured characteristic diameter is the Sauter Mean Diameter (SMD, the sum of all measured particle diameters to the square divided by the sum of all measured diameters to the cube).

The aspect fuel tuning, especially regarding additives is essential regarding atomization quality and is in conflict with emissions, so that a compromise is to be found. Fuel tuning was a major field of research in the 80's during the introduction of lead free gasoline in the automobile world.

#### **3.1.3.6 Coking**

In terms of heat management it is interesting to push the temperature of the fuel as high as possible when injecting it so that vaporisation happens as soon as possible.

However, at elevated temperatures the fuel reacts with its dissolved oxygen contents and produces coking with the risk to plug the piping's narrow passages. For conventional fuels, the temperature of the fuel shall remain below 430K to ensure security.

For instance, technologies such as multi-points injection are known to be sensitive to coking. At cool down, heat transfers via conduction to the nozzle and heats up remnant fuel. Flushing technologies are unwished because of added complexity and hardware and failure risk.

Among the parameters of interest, the aromatic contents play a similar role as in the production of soot with the agglomeration of benzene-like structures [14]. The fuel heat capacity is also of high importance.

## 3.2 Open literature survey

### 3.2.1 Spectrum of products

#### 3.2.1.1 Spectrum of products

A literature survey was performed on replacement fuels on a wide range. A matrix of first-generation replacement fuels distributed in the early phase of the project was taken as a reference.

Table 3.3: First-generation biofuel specifics, and comparison with kerosene. [14]

	Kerosene	Plant oils	Biodiesel (FAME)	BTL	MTBE
Energy	> 42800	38000	37400	43000	26900
Density	0.775 to 0.840	0.916 to 0.955	0.880	0.77	0.750
Freezing point	< -47	-15	< -15	> -47	-109
Viscosity	8	60 to 100	8.2	4	0.47 (16°C)
Thermal stability	> 260°	low	low	-	-
g. eq CO <sub>2</sub> /MJ	80	12	22	8	70

#### 3.2.1.2 Statistics on publications with a high impact factor

Using the Scopus literature engine, a hit count was performed using keywords pertaining the research effort on replacement fuels for aviation and their emissions.

According to Figure 3.7 a significant increase in papers available in the open literature with elevated impact factor (function of the number of times a paper is cited in similar fields of expertise) concerning aviation and fuels is observable over the last 10 years. A decrease is observable since 2010, even if the numbers for 2012 are still temporary at the time of drafting this report. The amount of papers concerning aviation and emissions and aviation and replacement fuels is slightly similar. The rising interest on replacement fuels for aviation is observable since about 2005, the amount of papers treating the emissions when using these fuels is about half the first figure. No paper on developing Low-Emission combustor designs specific to a replacement product was found.

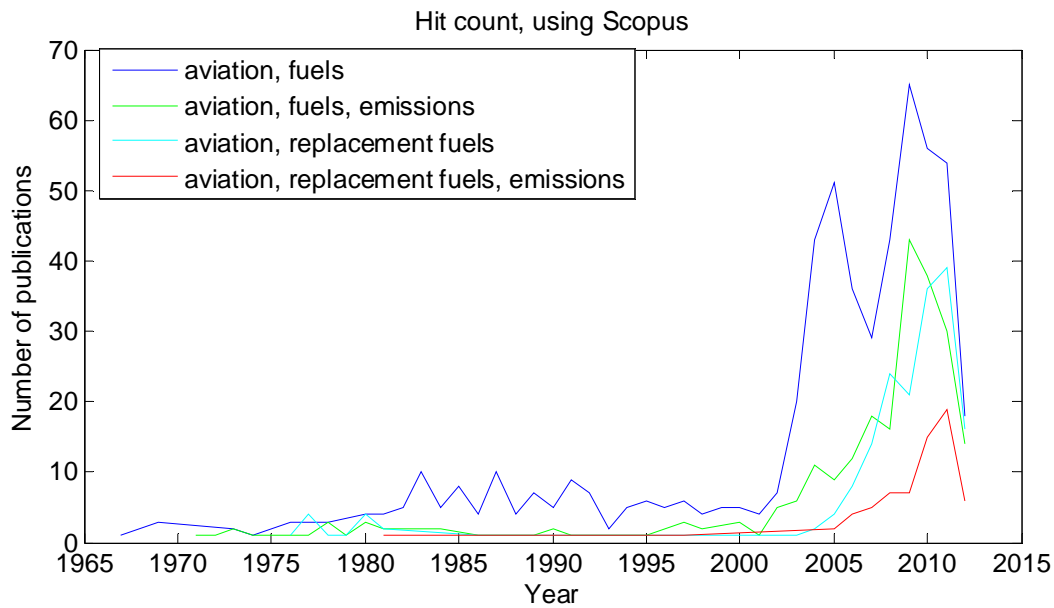


Figure 3.7: Hit count using the Scopus literature engine.

### 3.2.2 Kerosene Jet A1

Kerosene belongs to the intermediate crude oil distillation products with carbon chains from the  $C_9$  to the  $C_{15}$  range. It is multi-component, the concentrations are volatile as a function of the production site and crude oil origin.

Some approximations allow to simplify its properties to some commonly accepted values. However, research focuses on the effect of multicomponent evaporation, especially because of its impact on combustion stability and other environmental issues. The standard aviation fuel is Jet-A1. Table 3.4 provides some informations on the specifics of this fuel, and Table 3.5 lists the composition, according to a comprehensive study led by Rachner. [16]

Table 3.4: Kerosene Jet A1 [16]

Flash Point:	38°C
Auto-ignition temperature:	425°C
Freezing point:	-47°C (-40°C for Jet A)
Open air burning temperatures:	260-315 °C
Maximum burning temperature:	980°C
Approximate equivalent formula:	$C_XH_Y$ with $X=12$ and $Y=23$
Nearest model hydrocarbon:	Dodecan $C_{12}H_{26}$
Hydrogen content:	$y_H = Y M_H / M_{jetA1} = 0,13856$ kg H / kg Fuel
Mean molar mass:	$M_{jetA1} = X M_C + Y M_H = 167,315$ g/mol
Stoichiometric air-fuel-ratio:	$S_{stoech} = \frac{X+Y/4}{M_{jetA1}} \frac{M_{O_2}}{y_{O_2 in Air}} = 14,67$ kg Air/kg Fuel
Stoichiometric mixture fraction:	$f_{stoech} = 0,06382$ kg Fuel/ kg Air

Table 3.5: Composition Jet A1 [16]

chem	Name	Molar Mass [kg/kmol]	Mass Fraction [%]	Molar Fraction [%]	T <sub>crit</sub> [K]	p <sub>crit</sub> [bar]	V <sub>merit</sub> [cm <sup>3</sup> /mol]	$\omega$ azentr.Faktor
C <sub>8</sub> H <sub>12</sub>	n-Oktan	114,23	1,136	1,506	568,8	24,9	492,0	0,398
C <sub>9</sub> H <sub>20</sub>	n-Nonan	128,26	8,472	9,996	594,6	22,9	548,0	0,445
C <sub>10</sub> H <sub>22</sub>	n-Dekan	142,28	15,91	16,922	617,7	21,2	603,0	0,489
C <sub>11</sub> H <sub>24</sub>	n-Undekan	156,31	14,05	13,603	638,8	19,7	660,0	0,535
C <sub>12</sub> H <sub>26</sub>	n-Dodekan	170,34	14,154	12,575	658,2	18,2	713,0	0,575
C <sub>13</sub> H <sub>28</sub>	n-Tridekan	184,37	14,67	12,042	676,0	17,2	80,0	0,619
C <sub>14</sub> H <sub>30</sub>	n-Tetradekan	198,39	7,438	5,674	693,0	14,4	803,0	0,581
C <sub>15</sub> H <sub>32</sub>	n-Pentadekan	212,42	2,17	1,546	707,0	15,2	880,0	0,706
C <sub>9</sub> H <sub>18</sub>	n-Propyl-Cyclohexan	126,24	6,397	7,669	639,0	28,0	506,5	0,258
C <sub>10</sub> H <sub>20</sub>	n-Butyl-Cyclohexan	140,27	3,403	3,671	667,0	31,5	455,4	0,362
C <sub>8</sub> H <sub>10</sub>	Äthylbenzol	106,17	0,635	0,905	617,2	36,0	374,0	0,302
C <sub>9</sub> H <sub>12</sub>	1,2,4-Trimethylbenzol	120,19	6,463	8,137	649,2	32,3	430,2	0,376
C <sub>10</sub> H <sub>14</sub>	1,2,4,5-Tetramethylbenzol	134,22	5,102	5,753	675,0	29,4	482,3	0,435

### 3.2.3 Biodiesel

#### 3.2.3.1 Works by Glaude et al. [21]

Glaude et al. studied the adiabatic flame temperatures of some biodiesels, naphthas, natural gas fuels and blends of conventional diesel fuels. Since thermal NO<sub>x</sub> is the most significant form of NO<sub>x</sub> emissions in gas turbines, the adiabatic flame temperature can be considered as the main criterion for NO<sub>x</sub> emissions.

The fuels selected were studied by calculations with appropriate software. First, the enthalpy and free energy properties of the fuels were calculated with THERGAS. The software is intended for perfect gases and it is based on the group additivity method. The calculations were performed for gas mixtures, and the heat of vaporization of liquid fuels was not taken into account.

Then the adiabatic flame temperature at constant pressure was evaluated with GASEQ by calculating the temperature at which the free enthalpy of the combusted air/fuel mixture reaches its minimum. Both air and fuel were considered to be perfect gases. In the method used a set of reaction products is fixed to minimize the Gibbs free energy of the mixture at constant pressure. The adiabatic flame temperature is then attained iteratively until the enthalpy of the equilibrium composition is the same as that of the reactants.

The calculations were performed for three different cases. Case 1 was a standard case far from gas turbine conditions at 300 K and 1 atm with stoichiometric mixture of combustible in air. Case 2 represented an F-class gas turbine with a stoichiometric mixture at 673K and 16 atm and Case 3 a standard, i.e. E-class, gas turbine with a stoichiometric mixture at 623 K and 11.5 atm.

It is still worth noting that the calculations only allow a prediction of a trend when substituting a fuel to another but not of the real NO<sub>x</sub> emissions in a gas turbine. Also, only thermal NO<sub>x</sub> is taken into consideration whereas prompt and fuel NO<sub>x</sub> have been neglected.

From biodiesels, five Fatty Acid Methyl Esters (FAME) were studied, four of them derived from vegetable oils (VO) and representative of the most important biodiesel classes. The four vegetable oils considered were rapeseed, sunflower, soybean and palm oil. The fifth FAME studied was a tallow based biofuel, representative of biodiesel produced by trans-esterification of animal grease. The compositions of these FAME biodiesels are shown in Table 3.6.

Table 3.6: Compositions (mol-%) of the five biodiesel fuels considered in the study of Glaude et al. [21]

Name	Formula <sup>a</sup>	BF1	BF2	BF3	BF4	BF5
		Rapeseed	Sunflower	Soybean	Palm	Tallow
Myristic acid	C <sub>14:0</sub>	0	0	0	1	4
Palmitic acid	C <sub>16:0</sub>	5	6	10	44	27
Stearic acid	C <sub>18:0</sub>	3	5	4	6	24
Oleic acid	C <sub>18:1,Δ9</sub>	59	18	23	38	4,
Linoleic acid	C <sub>18:2,Δ9,12</sub>	21	69	53	10	3
Linoleic acid	C <sub>18:3,Δ9,12,15</sub>	9	1	8	0,5	0,5
Arachidic acid	C <sub>20:0</sub>	0,5	0,5	1	0,5	0,5
Gadoleic acid	C <sub>20:1,Δ9</sub>	1	0,5	0,5	0	1
Behenic acid	C <sub>22:0</sub>	0,5	0	0,5	0	0
Erucic acid	C <sub>22:1,Δ13</sub>	1	0	0	0	0

<sup>a</sup> In the formulae C<sub>x:y Δz</sub>, x is the number of carbons in the original acid, y is that of the double bond in the molecule and z is the position of a double bond on the alkyl chain relatively to the acid function

The calculated values of adiabatic flame temperatures are displayed in Table 3.7. The results show that the adiabatic flame temperatures of biodiesel fuels are higher than those of natural gases but close to those of conventional diesel fuels and naphtha. In particular, the adiabatic flame temperatures of biodiesels were found to be usually slightly lower than those of conventional diesel fuels, leading to slightly lower NO<sub>x</sub> emissions when using biodiesel fuels instead of conventional diesel fuels. Furthermore, there was no remarkable difference in the adiabatic flame temperatures between different biodiesels, predicting an even behaviour of biodiesels worldwide.

Table 3.7: Adiabatic flame temperatures (K) of selected fuels at constant pressure. [21]

Name	Case 1	Case 2	Case 3
BF1	2287	2556	2519
BF2	2291	2559	2522
BF3	2290	2558	2521
BF4	2279	2547	2510
BF5	2278	2546	2509
DF1	2291	2560	2523
DF2	2292	2560	2523
DF3	2309	2578	2541
NA1	2281	2548	2511
NA2	2287	2553	2517
NG1	2227	2449	2454
NG2	2245	2509	2470

BF: Biofuel, DF: Diesel fuel, NA: naphtha, NG: natural gas, Case 1: 300 K, 1 atm; case 2: 673 K, 13 atm; case 3: 623 K, 11,5 atm

### 3.2.3.2 Works by Bolszo and McDonell [22]

Bolszo and McDonell studied the plain-jet air blast atomization and evaporation of alternative liquid fuels. The attraction of using air blast atomization is that it maximizes the interaction between air and the fuel that, if done correctly, supports the generation of fine droplets in a well-distributed spray pattern. Due to the larger amount of air, air-blast atomization also leads to leaner combustion and thus lower soot particulate as well as CO and NO<sub>x</sub> emissions.

The study was performed in a commercial diesel-fuelled gas turbine with heat recuperation. Two alternative fuels were tested, 100 % ethanol and a soy biodiesel fuel that was blended with less than 1 % with diesel fuel; named E100 and B99, respectively. The results were compared with the results obtained with the diesel fuel DF2. The power of the gas turbine was 30 kW and the tests were conducted with engine loads of 50-100%.

In comparison to DF2, biodiesel B99 was found to have larger droplet size and significantly longer evaporation lifetime. That was seen to be the main reason for the higher NO<sub>x</sub> emissions.

Figure 3.8 represents the emission reduction for the B99 biodiesel as a function of the Air-to-Liquid ratio (ALR). It shows that for all engine loads tested, the minimum NO<sub>x</sub> emissions were obtained at ALR = 0.85. Also the droplet size was found to decrease at the optimal ALR. The droplet size of B99 at ALR = 0.85 was thus significantly smaller in comparison with the DF2 droplet size at the baseline ALR but, as shown in Figure 3.9, the emissions of B99 at the optimized ALR are still higher than those of DF2 at the baseline. This observation supports the idea that atomization quality is not the only parameter affecting between fuel injection performance and emissions, but attention must be paid also to additional factors. Nevertheless, it was shown that the ALR optimization has potential for emission reduction. In the study of Bolszo and McDonell, ALR optimization reduced NO<sub>x</sub> emissions by 21-25 % while it did not affect CO emissions.

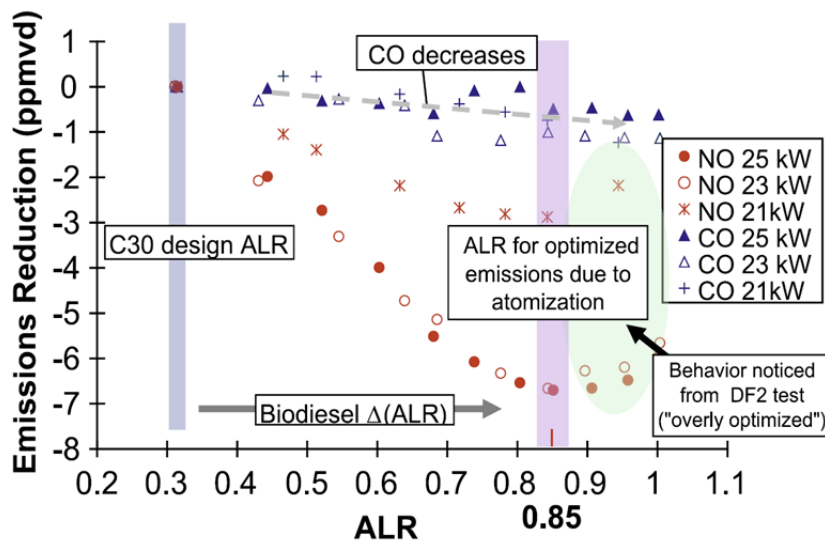


Figure 3.8: Emission reduction in parts per million volume dry (ppmvd) as a function of Air-to-Liquid ratio (ALR). [22]

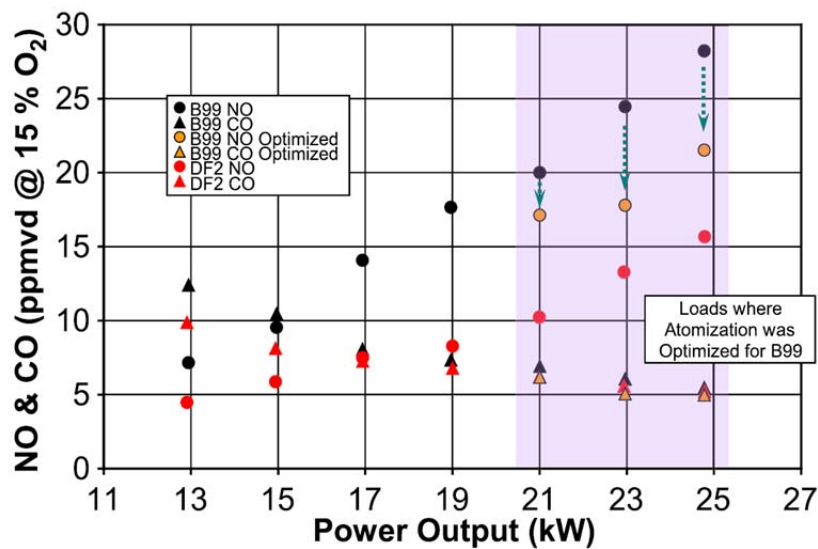


Figure 3.9: NO and CO emission improvement achieved by optimization of atomization for B99 in comparison to DF2. [22]

### 3.2.3.3 Works by Park et al. [23]

Park et al. also studied the possibility of reducing emissions through optimization of spray characteristics, including spray tip penetration, spray area and droplet size. It had already been discovered by previous studies that using the pilot injection strategy decreases CO and HC emissions since it improves the atomization. On the contrary, the heat released when the pilot injection timing approaches the main injection timing causes high temperatures in combustion chamber, leading to increased NO<sub>x</sub> emissions. In turn, the split injection strategy had been found to remarkably decrease NO<sub>x</sub> emissions, without significantly increasing soot emissions. Furthermore, it had been

observed that increasing the blending ratio of the biodiesel in a biodiesel-conventional diesel fuel blend reduces HC and CO emissions but increases the amount of NO<sub>x</sub> produced.

The fuel examined by Park et al. was an undiluted biodiesel fuel, soybean oil methyl ester (SME). The study was conducted both theoretically and experimentally. Numerical results were obtained by the KIVA-3V code. The experimental part was performed in a diesel engine, and spray tip penetration, spray area, spray centroid, injection delay and Sauter mean diameter (SMD) were analyzed. Results obtained for the biodiesel were then also compared to those of a diesel fuel, ultra low sulfur diesel (ULSD).

In the experimental test, the droplet size of the SME biodiesel was found to be slightly larger than that of the conventional diesel. The difference was, however, rather small, and it was explained by higher viscosity and worse volatility characteristics of the biodiesel fuel when compared to conventional diesel. The numerical results of the droplet size distribution were in good agreement with the experimental results. It was concluded that blending biodiesel with another fuel having low viscosity and good volatility will enhance the fuel injection and atomization.

### 3.2.4 Vegetable oils

#### 3.2.4.1 Works by No [24]

Soo-Young No reviewed the studies of the performance and emissions of vegetable oils in internal combustion engines, concentrating particularly in the effect of vegetable oils and their derivatives on spray characteristics. The vegetable oils primarily concerned were soybean, rapeseed, palm oil, jatropha, karanja, rubber seed and used cooking oils. Spray angle, spray penetration and liquid phase penetration were investigated from macroscopic spray characteristics, from microscopic characteristics only the Sauter mean diameter was analyzed.

In previous studies, using biodiesels in diesel engines was found to significantly decrease particulate emissions. Contra-wise, HC and NO<sub>x</sub> emissions were found to be higher than with conventional diesel fuel. Nonetheless, it had also been stated that neat vegetable oils have about 6 times higher life-cycle output-to-input energy ratio than conventional diesel fuels, and 2-6 times that of biodiesels. Furthermore, neat vegetable oils were also stated to have higher potential to decrease life-cycle greenhouse gas emissions than bio- or conventional diesel.

While investigating the studies of the spray angles of vegetable oils and vegetable oil derived biodiesels, Soo-Young No found that the spray angle of vegetable oils and their blends is very small compared to that of conventional diesel, while the blending ratios of vegetable oils in the blends did not have a significant effect on the spray angle. According to Soo-Young No, biodiesel fuels also have smaller spray angles than conventional diesel, decreasing with increasing amount of biodiesel in the blend. It had also been suggested that the smaller spray angle would be one of the main reasons for the increased NO<sub>x</sub> emissions when burning biodiesels. It was stated that a possible explanation for that could be that while the decreased spray angle increases the spray penetration, the degree of widespread combustion in the chamber is increased and therefore also NO<sub>x</sub> emissions increase.

Vegetable oils and their blends were also found to have larger Sauter mean diameters than diesel fuel. However, it was as well concluded that according to the review made, the original vegetable oil used in the biodiesel production also has an effect on the spray characteristics and atomization quality of the product fuel.

### 3.2.5 Hydrotreated vegetable oil [25]

According to the definition by Knothe, biodiesel fuels are mono-alkyl esters of long-chain fatty acids derived from vegetable oils or animal fats. Biodiesel fuel is derived from an oil or fat by trans-esterification, and glycerol occurs as a co-product of the formation. The European biodiesel standard is referring to Fatty Acid Methyl Esters (FAME). In contrast to that, a diesel fuel based on hydro-treated vegetable oils (HVO) is a petrodiesel-like fuel that has been derived from biological sources. It is also often called renewable diesel.

#### 3.2.5.1 NExBTL [27]

Neste Oil has developed a HVO renewable diesel NExBTL. Neste Oil claims that it has great potential to reduce the greenhouse gas emissions in aviation, including both CO<sub>2</sub> emissions and other pollutants. There have also been test flights with NExBTL in cooperation with Lufthansa, and the results were promising. [26]

NExBTL is basically a mixture of n- and isoparaffins. It has high cetane number and it is sulfur-, oxygen-, nitrogen- and aromatic free. In general, HVOs have properties similar to Gas-to-Liquid and Biomass-to-Liquid fuels produced by Fischer-Tropsch synthesis. HVOs can also be produced from many different kinds of vegetable oils without any significant influence in fuel quality, unlike with FAMES whose properties are highly bound to the feedstock used.

#### Works by Lindfors [28]

In his paper, Lindfors summarizes several HVO emissions studies that have been performed with NExBTL renewable diesel in passenger cars as well as in heavy duty engines and vehicles. It had been found that in general the emissions of NO<sub>x</sub>, HC, CO, PAH and particulate are significantly decreasing when using HVO as a fuel. The result makes a remarkable difference to biodiesels, i.e. FAMES, since FAMES usually increase NO<sub>x</sub> emissions. It had also been found that NO<sub>x</sub> and particulate emissions are decreasing quite linearly when the blending ratio of HVO in the fuel increases. In terms of CO and HC, HVO had been found to reduce emissions already with low blending ratios. In addition to that, Lindfors stated that NExBTL has a great potential to decrease greenhouse gas emissions also in aviation.

#### Works by Rantanen et al. [29]

Rantanen et al. studied the use of NExBTL in passenger cars. They blended NExBTL in various proportions with conventional diesel fuel EN590 and Swedish Environmental Class 1 (EC1) diesel fuel. Both base fuels are sulfur free and have high quality when it comes for example to cetane number or the content of aromatics and poly-aromatics. The fuel blends were tested in modern passenger cars, with and without catalyst.

The results of emission measurements showed that there was no significant difference in NO<sub>x</sub> emissions. All the same, blending NExBTL in diesel fuel was found to reduce CO and HC emissions and particulate. However, emissions were, although relatively clearly reduced, already so low that the reduction at absolute scale was not very significant. It was also found that blending NExBTL to EN590 had greater influence in emissions than the blending with EC1. This was because EC1 already as pure had lower emissions than EN590.

Within the measurement accuracy, NExBTL was not found to have an effect on fuel consumption. This was supported by the measured CO<sub>2</sub> emissions that were similar to both blends and base fuels.

### **Works by Aatola et al. [27]**

Aatola et al. conducted similar tests with a heavy duty diesel engine. Tests were performed with sulfur free commercial summer grade diesel fuel (EN590), neat HVO and a blend with 30 % HVO and 70 % conventional diesel fuel (EN590-30).

The results showed that the use of 100 % HVO fuel significantly reduces emissions. In the study, the reduction in smoke was more significant but also the decrease in NO<sub>x</sub> emissions was clear. EN590-30 also caused a reduction in smoke emissions but the level of NO<sub>x</sub> remained unchanged. The changes in total hydrocarbons (THC) and CO were not remarkable because the emissions were low already for the reference fuel EN590.

The very low aromatic hydrocarbon and poly-aromatic content of HVO as well as its high cetane number were suggested to be the main reasons for low smoke emissions. Furthermore, the shorter ignition lag and the lower volumetric heating value that leads to longer-lasting fuel injection were suggested to be the possible causes to the lower NO<sub>x</sub> emissions, since they might lengthen the combustion time and thus lower the temperature.

Specific fuel consumption is also significant for the emissions since CO<sub>2</sub> emissions are depending on mass based fuel consumption. 100 % HVO was shown to decrease the specific fuel consumption. Similar trend was obtained with EN590-30 blend but the difference was, naturally, not so clear. The study was stated to be in good agreement with earlier studies performed with heavy duty engines fuelled with GTL and FT-BTL.

## **3.2.6 Alcohol fuels**

### **3.2.6.1 Works by Moliere et al. [30]**

Moliere et al. performed field tests of the combustion of an ethanol-naphtha blend that contained up to 95% of ethanol. The tests were performed with a Frame 6B gas turbine owned by Reliance Energy. The fuel normally used in the gas turbine is naphtha; in addition a distillate fuel is used for start-up and shutdown. The gas turbine is operating in combined cycle with bypass stack, but the tests were performed in simple cycle, as well with bypass stack. Intensive site preparations were made before the tests, and the experiment was started by baseline tests with gasoil and pure naphtha before the ethanol tests.

The results considering the emissions are represented in Figure 3.10. It was found that increasing the percentage of ethanol in the fuel blend leads to lower NO<sub>x</sub> emissions, and the NO<sub>x</sub> emissions formed in the combustion of 100 % ethanol were only about a half of those in the combustion with 100 % naphtha. Furthermore, regardless of the blend tested, there were almost no CO and UHC emissions. It was also found that burning ethanol produces a slightly greater amount of CO<sub>2</sub> emissions since due to its smaller lower heat value, the fuel consumption of ethanol is slightly larger than that of naphtha.

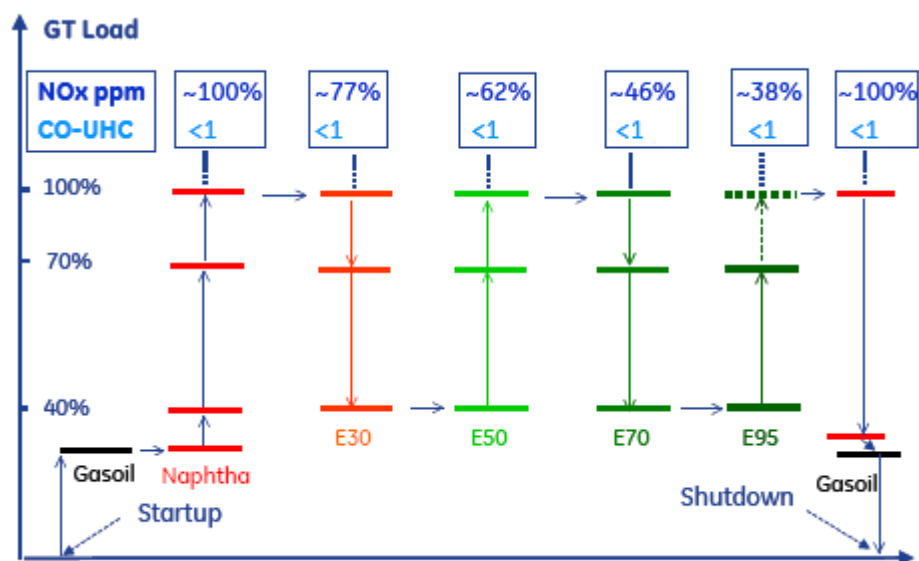


Figure 3.10: Results from the ethanol-naphtha field test. [30]

### 3.2.6.2 Works by Padala et al. [31]

Padala et al. also studied ethanol and in particular its effects on spray parameters. When it comes to emissions, especially the droplet size can be seen as the question of interest since the smaller droplet size is believed to contribute the reduction of UHC emissions. Padala et al. also stated that due to its non-fossil origin, ethanol has potential to reduce CO<sub>2</sub> emissions.

The study was performed with gasoline, ethanol and 50 % in volume blend of gasoline and ethanol (E50), and the ambient conditions were kept fixed. An optical spray chamber was used to simulate engine intake conditions and to image Mie-scattered fuel sprays. Post-processing was applied to get the parameter data, i.e. the mean droplet diameter, number of droplets and spray-tip penetration. Also the effect of intake boosting was investigated.

Ethanol was found to have smaller mean droplet diameter in comparison to gasoline, which was explained by the fact that gasoline has heavier molecules that are thus also atomized or evaporated at a slower rate than those of ethanol. The droplet diameters measured for ethanol were, nevertheless, higher than those presented in the literature and previous studies. Differences in diagnostics and variations in operating conditions were offered as causes for the differences between measured diameters and literature values; and thus the measurements were stated to be reasonable close to previous ones. The mean droplet diameters and number of droplets as a function of time after the injection (time aSOI) are shown in the Figure 3.11. It was seen that the increased ethanol content causes a decrease in the mean droplet diameter.

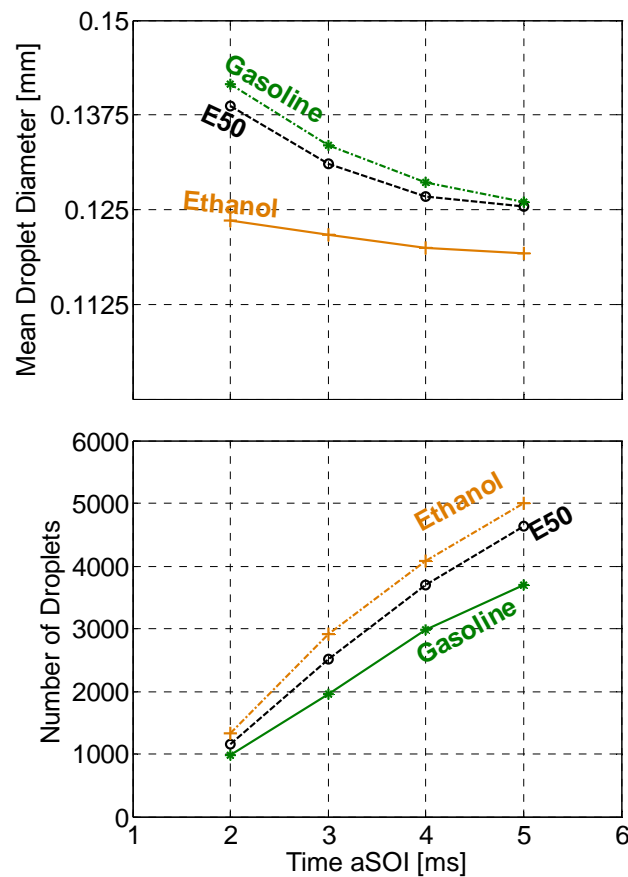


Figure 3.11: Mean droplet diameter and number of droplets in function of time aSOI (time after the start of injection) for gasoline, 50 % blend (E50) and ethanol. [31]

### 3.2.6.3 Works by Zhang et al. [32]

Zhang et al. studied the effect of alcohols, in particular ethanol and butanol, in spray and atomization characteristics. Quoting earlier studies, they noted that ethanol may help to achieve a great decrease in CO and NO<sub>x</sub> emissions. Butanol was also introduced as a possible future fuel since in comparison to ethanol, its properties are closer to gasoline, but in terms of emissions and renewability it still has the same benefits as ethanol. In previous studies in a port-fuel-injected spark-ignition engine butanol was found to have lower peak temperature than gasoline but between two or three times higher UHC emissions, and therefore the atomizing of butanol was suggested to be less effective than that of gasoline and ethanol.

The fuel effects on spray structure and atomization were studied for ethanol, butanol and isooctane. Isooctane was used to simulate gasoline. A swirl-type inwardly opening gasoline direct injection (GDI) injector was used to analyse spray structure and cone angle. The measurements were performed with two different injection pressures, and the particle size distribution, as well as Sauter mean diameter (SMD), DV(50) and DV(90) were obtained.

It was shown that higher injection pressure decreases the droplet size of isooctane. In case of ethanol and butanol, it helps producing a more uniform particle size distribution but unfortunately does not necessarily decrease the droplet size. As a result, Zhang et al. suggested that the switch-

ing from conventional fuels to alcohols in GDI engines should be made with care due to the fact that atomization and mixing may significantly vary between different fuels.

### 3.2.6.4 Works by Glaude et al. [21]

In the study by Glaude et al., it was found that alcohols, represented by triangles in the Figure 3.12, have slightly lower adiabatic flame temperatures than corresponding alkanes. This is due to the fact that the oxygen atom is already bounded to a carbon atom and the heat of combustion is therefore lower. The result was found to be consistent with the results of Moliere et al. represented earlier in Chapter 3.6.1. Furthermore, the finding that the combustion of ethanol is producing less NO emissions than the combustion of pure naphtha was explained by the fact that ethanol corresponds to the adiabatic flame temperature equal to 2238 K that is lower than the adiabatic flame temperature of the main components in naphtha, i.e. alkanes with 7 or 8 carbon atoms.

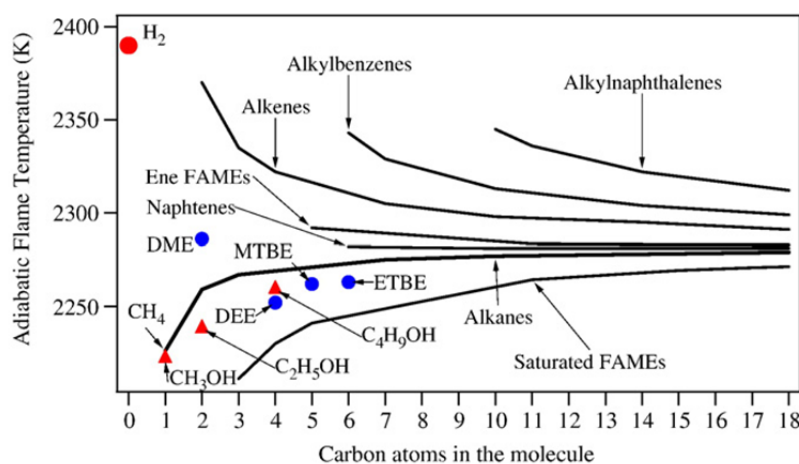


Figure 3.12: Adiabatic flame temperatures at 300 K and 1atm as a function of the number of carbon atoms in the molecule. [21]

## 3.2.7 Hydrogen

### 3.2.7.1 Works by Nojoumi et al. [33]

Nojoumi et al. studied the effect of hydrogen on the greenhouse gas emissions of aviation. They examined some sample flights, including estimations of their  $\text{NO}_x$ , HC and CO emissions, and compared the results from conventional aircraft to those of an aircraft using liquid hydrogen as a fuel, i.e. an  $\text{LH}_2$  aircraft. As a result they stated that hydrogen has potential to remarkably decrease the greenhouse gas emissions in aviation. They claimed the emissions of an  $\text{LH}_2$  aircraft to be low or even zero, when the hydrogen is produced from a non-emitting source. The emissions of an  $\text{LH}_2$  aircraft are so low because burning hydrogen produces only water vapor, containing a small amount of  $\text{NO}_x$ ; and water vapor, even though also being a greenhouse gas, is at lower altitudes less effective than  $\text{CO}_2$  or  $\text{NO}_x$ .

When the hydrogen production is neglected,  $\text{LH}_2$  aircraft generates zero  $\text{CO}_2$  emissions.  $\text{LH}_2$  aircraft should be used at altitudes lower than 12 km since  $\text{NO}_x$  emissions from the aircraft increase the ozone concentration, and an increase in the amount of ozone in lower altitudes increases radia-

tive forcing and thus the climate change less than the same increase in ozone in the upper troposphere.

### 3.2.7.2 Works by Yilmaz et al. [34]

Yilmaz et al. also examined some sample flights in order to study the potential of hydrogen to decrease the emissions in aviation. The total fuel usage and NO<sub>x</sub>, HC and CO emissions of the sample flights were estimated and as in the study by Nojoumi et al., hydrogen was also found to decrease the emissions. HC and CO emissions were found to be close to zero since hydrogen fuel does not contain carbon. NO<sub>x</sub> emissions were also found to be lower, and the wider flammability limit of liquid hydrogen in comparison to conventional jet fuels was taken as an explanation to that. Wider flammability limit allows the use of hydrogen fuel in a wider range of margins, which in turn allows lower NO<sub>x</sub> production. Engine redesign and a 2-3 km lower flight altitude were also offered as possibilities to reduce NO<sub>x</sub> emissions. Also the lean combustion, which can be used to reduce NO<sub>x</sub> emissions, is less complicated to realize with hydrogen than with conventional jet fuel since the flame out point of hydrogen is very low. Engine redesign can also lead to less NO<sub>x</sub> production than with any kerosene system, mainly because the weak extinction limit of hydrogen is significantly leaner than that of kerosene. The turbine temperature is also slightly slower for hydrogen fuel, which contributes a longer engine life. It was, however, also highlighted that the production process of hydrogen has a significant role when considering the emissions, and to minimize the emissions renewable hydrogen sources should be favoured.

The energy content of hydrogen is almost 2.6 times that of kerosene. However, a volume of a hydrogen fuel is 4 times larger than the volume of kerosene containing the same amount of energy. In addition to that, the more complex and heavier fuel system and fuel tanks also compensates the benefit of the higher energy content.

Furthermore, the life cycle CO<sub>2</sub> emissions of liquid hydrogen and kerosene as aviation fuel were compared with the conclusion that using hydrogen may decrease the life cycle emissions by nearly 140 kg CO<sub>2</sub> per MWh.

### 3.2.7.3 Works by Janic [35]

Janic studied the use of liquid hydrogen as aviation fuel as well, concentrating on the “carbon-neutral” air transport. Also he regards hydrogen as a low-emission fuel. Moreover he stated that the previous experiments have shown that cryogenic aircraft will have a specific fuel consumption that is around 64 % lower than that of conventional aircraft. Cryogenic engines are also expected to have 1-5 % better efficiency in generating thrust from the given energy content. Furthermore, they are supposed to have slightly lower turbine entry temperatures, which lengthen their life time and reduces maintenance costs.

However, a cryogenic aircraft emits H<sub>2</sub>O in quantities about 2.6 times higher than conventional aircraft at and above the cruising altitudes of 31 000. This could be weakened by operating at lower altitudes, as stated above, but it would affect other aircraft performances. In addition, cryogenic aircraft emits about 5–25% of the emissions of NO<sub>x</sub> of their conventional counterparts, a gain expected to be achieved by the adequate design of the combustion chamber of cryogenic engines. Janic had also developed a model to estimate the greenhouse gas emissions and applied it to the longterm development and emissions of aviation system for different sub-periods according to different scenarios. The results show that if only conventional aircrafts are used, the greenhouse

house gas emissions will continuously grow. Instead of that, replacing conventional aircrafts gradually by cryogenic ones has potential to restrict the growth or even decrease CO<sub>2</sub> and NO<sub>x</sub> emissions. However, he stated that H<sub>2</sub>O emissions still remain as a primary concern of the usage of LH<sub>2</sub> aircrafts.

### 3.2.8 Synthetic fuels (XtL)

#### 3.2.8.1 Works by Moses and Roets [36]

Moses and Roets conducted studies of the fully synthetic jet fuel of Sasol. The synthetic jet fuel is made from coal-derived synthetic gas by Fischer-Tropsch method, being thus a so called Coal-to-Liquid (CtL) fuel. The tests concerning emissions were performed with a single test fuel provided by Sasol. The test fuel was a blend of approximately 70 % iso-paraffinic kerosene (IPK) and 30 % heavy naphtha. The most important properties and characteristics of the test fuel are represented in Table 3.8.

Table 3.8: Properties and characteristics of the Sasol test fuel. [36]

Fuel Property	Specification Limits	Value
Aromatics, vol%	8.0 – 25.0	10.9
Sulfur, wt%	0.3 max	< 0.01
Smoke point, mm	25.0 min	28
Viscosity, cSt	8.0 max	4.09
Density, kg/m <sup>3</sup>	771.0 - 836.0	781.2
Freezing point, °C	-47.0 max	-55.0
Flash Point, °C	38.0 min	51.0
Heat of combustion, kJ/kg	42.8	43.7

The emission test was performed by Pratt & Whitney using a commercial combustor with an 80°, four-nozzle arc sector rig. The data was obtained from the combustor exit as averages of the samples from the center two sections. Tests were performed at various pressures and inlet temperatures as well as fuel/air ratios and combustor flow parameters, and the measurement data was then scaled to flight conditions. After the tests with synthetic fuel, also Jet A was tested in the same conditions and with the same procedures to enable the comparison between the fuels.

Figure 3.13 and Figure 3.14 represent the NO<sub>x</sub> and CO emissions obtained, respectively. The results are displayed for a simulated landing take-off (LTO), sea-level take-off (STLO), climb, approach and idle. It is to be seen that for the Sasol synthetic jet fuel, the LTO cycle NO<sub>x</sub> emissions were 4 % lower compared to Jet A, while the CO emissions were 19 % lower. It was also found that for the synthetic jet fuel, the NO<sub>x</sub> emissions at individual power points stayed virtually unchanged whereas the CO emissions were lower, especially at the idle. When it comes to CO<sub>2</sub> emissions, the differences between the Sasol synthetic jet fuel and Jet A were negligible.

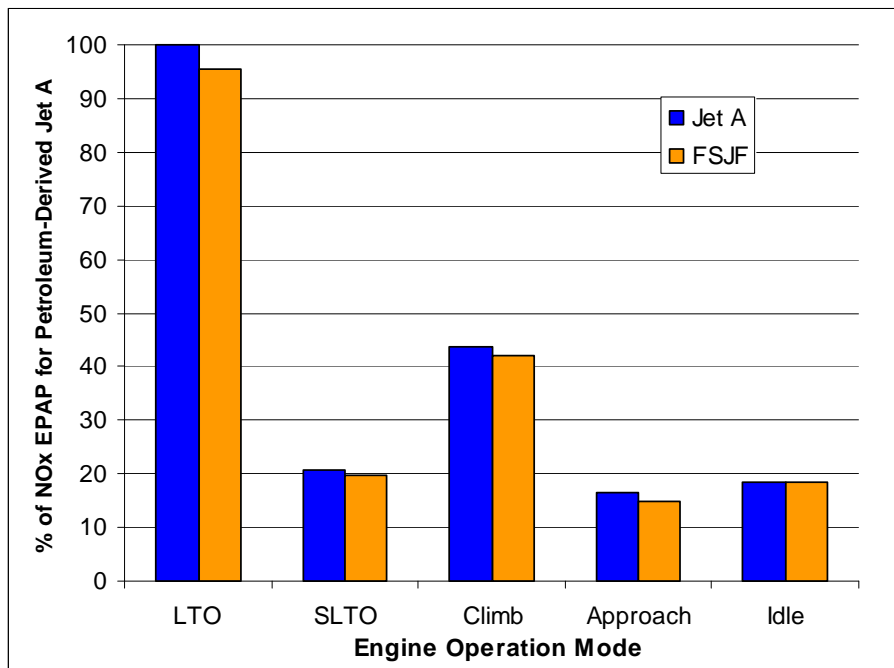


Figure 3.13: NO<sub>x</sub> emissions of synthetic Sasol jet fuel and Jet A. [36]

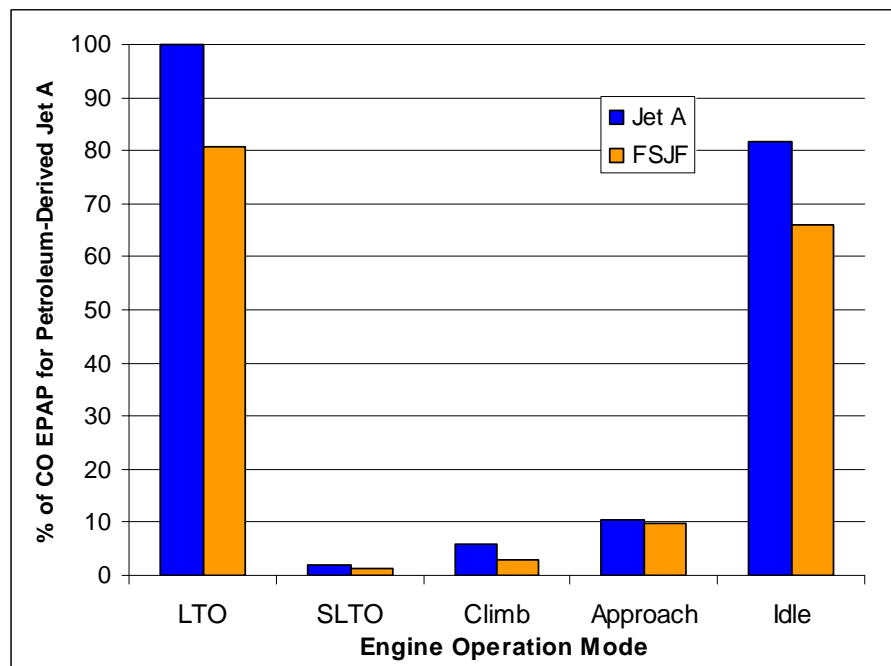


Figure 3.14: CO emissions of synthetic Sasol jet fuel and Jet A. [36]

Table 3.7 compares the UHC emissions of the Sasol synthetic jet fuel and Jet A. Data was obtained only for the idle condition since the level of UHC at other power points was too low compared to the uncertainty of the measurement. Table 3.9 shows that the difference in UHC emissions between the fuels was insignificant.

Table 3.9: UHC emissions of synthetic Sasol jet fuel and Jet A. [36]

Fuel	UHC, ppm
Sasol FSJF	11.8
Jet A	16.0

Figure 3.15 displays the smoke number. The data is normalized to the results of Jet A. It was found that the smoke number of the Sasol synthetic jet fuel was lower than that of Jet A. This is consistent with the expectation while the Sasol synthetic jet fuel has higher hydrogen and thus lower aromatic content than Jet A. The outlier at STLO at a fuel/air ratio of 0.018 was caused by the low smoke number of Jet A.

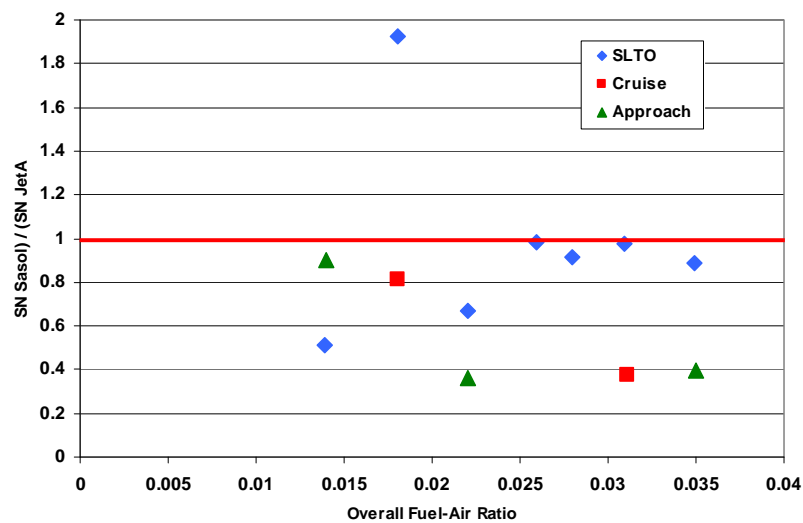


Figure 3.15: Smoke number (SN) of synthetic Sasol jet fuel and Jet A. [36]

According to Pratt & Whitney, the results show that switching from Jet A to Sasol synthetic jet fuel does not have adversely effect on the emissions. They concluded that the same air/fuel ratio would be used for the synthetic fuel as for the Jet A.

## Chapter 4

# Analysis of the Alfa-Bird data

### 4.1.1.1 Experimental database on the kinetics of reformulated kerosene combustion [38]

Dagaut et al. studied the kinetics of reformulated kerosene combustion and pollutants formation. The data was obtained by two experiments: a pool fire experiment that was used to analyze the polyaromatic hydrocarbons (PAH) from soot samples, and a pressurized jet-stirred reactor (JSR) that was used to investigate the kinetics.

The pool fire experiment was performed for rapeseed oil methyl ester (RME), methyl decanoate and hexanol in 20 % volume blends with kerosene Jet A. JSR tests were performed for Coal-to-Liquid (CTL) fuel, Gas-to-Liquid (GTL) fuel, GTL-hexanol blend, naphthenic cut, GTL-naphthenic cut blend and GTL-hydro-treated vegetable oil (HVO) blend. Nevertheless, the low carbon balance in GTL-HVO blend caused experimental problems, and there are thus no results presented for this blend.

Results from pool fire experiment show that blending oxygenates to kerosene tends to decrease the concentration of PAHs in soot and also significantly reduce the mass of soot. The PAH reduction with 20 % in volume oxygenate blended in kerosene ranged between 5 and 73 % and the mean reduction was 41 %, 36 % and 16 % when used RME, methyl decanoate and hexanol as oxygenate, respectively. The mean reduction of all three oxygenates tested was 31 %.

In the JSR experiment the concentrations of various species during the oxidation of the fuels were measured. Since the experiment was concentrating on the kinetics of the reactions, it does not offer much valuable information of the emissions.

### 4.1.2 Comparison of the performance (stability and emissions) of a real airblast nozzle working with normal/alternative fuel at atmospheric pressure [37]

Four alternative fuels, Coal-to-Liquid (CTL), Gas-to-Liquid (GTL), GTL with 50 % naphthenic cut and GTL with 20 % hexanol, were studied by the Karlsruhe Institute of Technology. Later on, when concerning this study, the fuels are referred to with their fuel reference numbers 8289, 8291, 8286 and 8040 respectively. The heat of combustion for each alternative fuel tested is shown in Table 4.1. As a reference fuel, standard kerosene was tested.

Table 4.1: Heat of combustion for the alternative fuels tested [37]

Fuel	Reference number	Heat of combustion [MJ/kg]
CTL	8040	44.24
GTL	8289	42.00
GTL + 50 % naphthenic cut	8286	43.54
GTL + 20 % hexanol	8291	43.24

Tests were performed by an AVIO burner with a combustion chamber. It had two radial swirlers and a fuel atomizer at the axis of the burner. For kerosene a pressure atomizer was used.

Figure 4.1 displays the Emission Indexes (EI in g/Kg fuel) of CO for the fuels tested. It was found that the Emission Index of CO decreases when equivalence ratio decreases moving from unity towards smaller values, i.e. the conditions become leaner. It is also shown that kerosene seems to have the smallest Emission Index of CO, smaller than any of the alternative fuels.

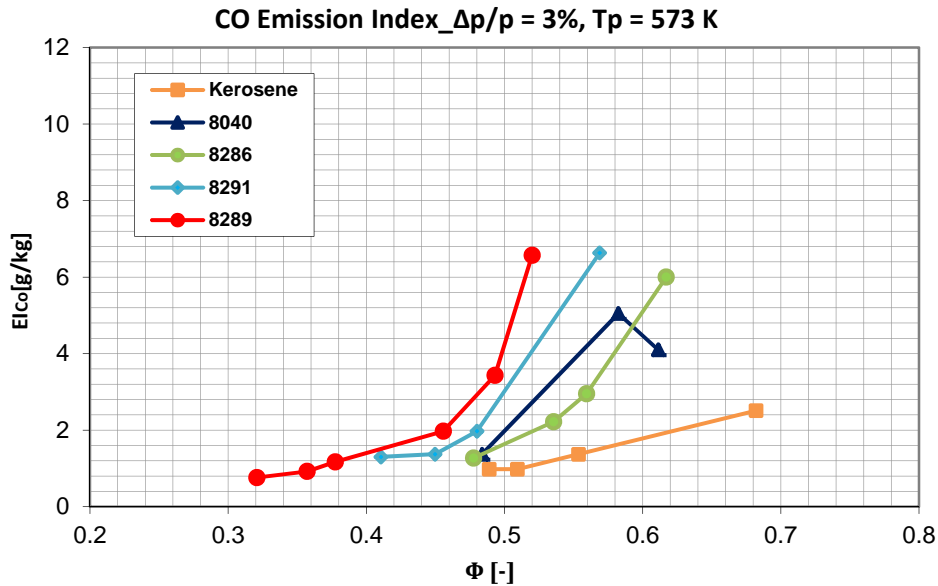


Figure 4.1: Emission Index of CO for the fuels tested. [37] modified

The Figure 4.2 then displays the Emission Indexes of  $\text{NO}_x$ .  $\text{NO}_x$  increases as the equivalence ratio approaches unity because the adiabatic flame temperature increases. It was also claimed that the GTL fuel has a comparatively higher Emission Index of  $\text{NO}_x$  than other alternative fuels tested. This was explained by the fact that GTL has the highest heat of combustion that causes relatively higher adiabatic flame temperatures and thus  $\text{NO}_x$  emissions. Kerosene seems, however, again to be better than the alternative fuels.

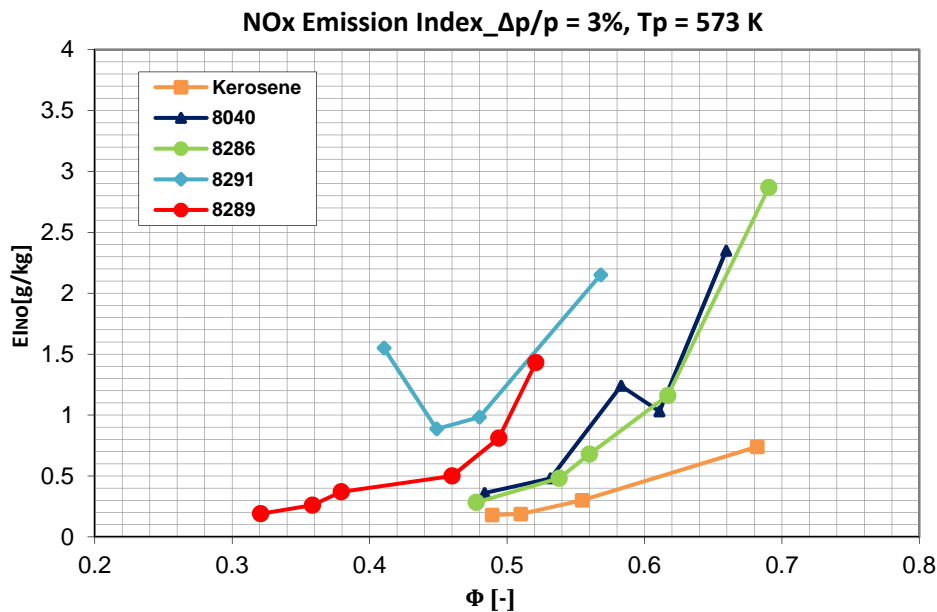


Figure 4.2: Emission Index of NO<sub>x</sub> for the fuels tested. [37] modified

For all the alternative fuels tested, the lean blow out (LBO) limits were found to be higher than for kerosene. Higher flame temperature and higher laminar flame velocity of alternative fuels were suggested to be the main reasons. Furthermore, the GTL fuel seemed to have the highest LBO stability at most of the conditions tested. This results support the suggestion of the importance of flame temperature in LBO limit since as already mentioned, the GTL fuel also has comparatively higher heating value than other fuels tested and thus relatively higher flame temperature. All tested alternative fuels were also found to have leaner blow out equivalence ratios than kerosene.

#### 4.1.3 Experimental database on the effect of fuel reformulation on pollutants emissions: Specification of pollutants formed by reformulated kerosene [40]

Thomson et al. studied reformulated kerosene combustion and pollutants formation by investigating gaseous species, soot and temperature in different atmospheric coflow diffusion flames. The alternative fuels tested were Gas-to-Liquid (GTL or FSJF), Coal-to-Liquid (CTL), a blend of 80 % GTL and 20 % hexanol (Hex20-GTL), and a blend of 80 % GTL and 20 % naphthenic cut, all percentages representing proportions in volume.

The measurements of gaseous species were performed only for the first three fuels, i.e. for GTL, CTL and Hex20-GTL. All measurements were done both alongside the centreline and at several radii. The burner used was a co-annular non-premixed flame burner. Only significant differences in gaseous species between CTL and GTL species concentrations were acetylene and, in particular, ethylene, the concentrations of which were higher for GTL than for CTL. This might have been expected since GTL contains considerably more n-paraffinics than CTL. In comparison with GTL and Hex20-GTL, the trends of gaseous species were as well found to be similar. Ethylene was again the exception, having a concentration peak in the Hex20-GTL flame at the height of  $z = 32$  mm while the corresponding peak in GTL flame is at  $z = 36$  mm.

#### **4.1.4 ONERA contribution – Spray atomization and evaporation from atmospheric to high pressure: LACOM experiments [31]**

D’Herbigny et al. studied the injection, atomization and evaporation of alternative fuels by spray visualization and PDI measurements. The fuels discussed were CtL, GtL, GtL with 20% in volume of hexanol and GtL with 50 % in volume of naphthenic cut. Experimental conditions were ranging from atmospheric conditions to high pressure and high temperature. Semi-angle of the spray and the droplet size and velocity distributions at two stations in the test chamber were analyzed. The test rig used was designed to partially meet the conditions of a combustion chamber in terms of pressure and temperature. The main elements of the test rig are a plenum chamber with mass flow, pressure and temperature measurements; a test chamber with optical windows; and an exhaust system for hot gases. An airblast injection system was also used.

The results show that the fuels tested have similar spray expansion behaviour. Also the evolution of the Sauter mean diameter and of the mean components of the velocity were found to be similar between the fuels. Thus the fuel performances are equivalent with respect to the measured quantities. Although there wasn’t truly a difference between the particle sizes of the fuels, it can be observed from the results that the blend of GTL and 20 % in volume hexanol shows slightly smaller particle sizes than pure GTL. [41] This supports the results found by Padala et al., stating that ethanol forms smaller particles in comparison to gasoline. The early results on vaporisation of the same products performed at TU Graz show no dramatic change in fuel placement as a function of the fuel.

#### **4.1.5 Report on evaluation of Well to Tank greenhouse gas emissions [43]**

Thellier studied the Well-to-Tank greenhouse gas emissions of various alternative fuels. The fuels considered were Direct Coal Liquefaction (DCL), Indirect Coal Liquefaction (ICL), Gas-to-Liquid (GTL) and Biomass-to-Liquid (BTL) fuels. It was found that all fossil based alternative fuels, i.e. DCL, ICL and GTL, emit as much or more greenhouse gas emissions when compared to conventional jet fuel, even when the use of Carbon Capture and Storage (CCS) during the production process was considered, whereas BTL produces less greenhouse gases than Jet A. [42] Life cycle greenhouse gas emissions have also been discussed in several other reports. Stratton et al., for example, stated that the emissions of all alternative jet fuels relying exclusively on fossil fuels have higher emissions than conventional jet fuel. Nevertheless, when based on renewable feedstocks, Fischer-Tropsch fuels and Hydrotreated Renewable Jet (HRJ) fuel, i.e. hydrotreated vegetable oils (HVO), have a potential to reduce greenhouse gas emissions by 10-50 %, while the corresponding reduction with certain biofuels could rise up to 100 %, i.e. zero life cycle greenhouse gas emissions.

# Chapter 5

## Measurement Techniques

In the frame of the investigations on the evaporation and atomization 3 optical measurement techniques have been applied. Firstly Laser Doppler Anemometry in order to analyze the flow field for reasonability and correct construction of the existing configuration of the used combustor geometry. Secondly phase Doppler interferometry (used by ONERA Fauga Mauzac)(will not be discussed here) to define particle sizes and velocity components and finally the infrared extinction method to determine fuel specific absorption coefficients and the evaporation gradients in the flow field.

### 5.1 Laser Doppler Anemometry

#### 5.1.1 Principle

Laser Doppler Anemometry (LDA) is a non-intrusive optical measurement method that uses monochromatic, coherent, bundled light emitted by Continuous Wave Lasers (CW). The typical beam profile is defined by a Gaussian intensity distribution (TEM<sub>00</sub> mode). The measurement technique is based on the effect that coherent ( $\rightarrow$  constant frequency alongside a large distance) light emitted by a laser light source and scattered by moving particles in a flow is detected comprising a frequency shift that includes a velocity information. This phenomenon is generally known as Doppler Effect defined in equation ( 5.1 ).

$$f' = f_0 \left[ 1 - \frac{\vec{u} \cdot \vec{l}}{c} \right] \quad (5.1)$$

$f_0$  is the wave frequency of the incident laser light,  $\vec{u}$  is the velocity vector of the particle,  $\vec{l}$  stands for the directional vector of the laser light propagation and  $c$  represents the speed of light in the medium surrounding the particle.

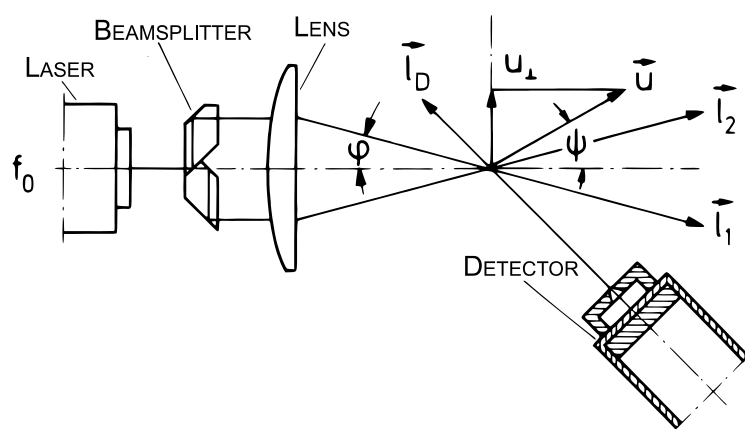


Figure 5.1: LDA Principle [47] modified

This technique can be applied to flows with bubbles, droplets and particles that are small enough to cause no impact on the flow field and are big enough to scatter sufficient laser light to be de-

tected. Usually the incident laser light beam is divided into two partial rays (Dual beam scattering configuration (Figure 5.1).

These partial rays are focused by a lens and the focal point of the lens represents the measurement volume. Due to the different directional vector of the rays the detector receives two differently frequency shifted signals  $F_{D1}$  and  $F_{D2}$  scattered by the particles.

$$f_{D1} = f_0 \left[ 1 - \frac{\vec{u} \cdot \vec{l}_1}{c} \right] \quad f_{D2} = f_0 \left[ 1 - \frac{\vec{u} \cdot \vec{l}_2}{c} \right]$$

Referring to the acoustic Doppler effect theory the detected wave frequency by the photo detector is different to the received frequency of the particles  $f'_1$  and  $f'_2$ . The detector processes superimposed waves which can be described by the signal frequency or 'Doppler Frequency'  $\Delta f$ .

$$\Delta f = f_{D1} - f_{D2} \approx f_0 \left[ \frac{\vec{u} \cdot \vec{l}_2 - \vec{u} \cdot \vec{l}_1}{c} \right] \quad (5.2)$$

Taking the trigonometric relations illustrated in Figure 5.1 into account and assuming that the speed of light  $c = f_0 \lambda$  results in the following reformulation of equation (5.1).

$$\Delta f = \frac{|\vec{u}| [\cos(\psi - \phi) - \cos(\psi + \phi)]}{\lambda}$$

$$\Delta f = |\vec{u}| \sin \psi \frac{2 \sin \phi}{\lambda} \quad (5.3)$$

It can be seen here that the detected frequency has a linear relation to the velocity and therefore needs no calibration. The proportionality can be determined in post processing.

For typical LDA systems the interference fringe model is often applied for effect explanation. The aforementioned laser beam emitting a plane wave front separated by a beam splitter and then focused in the measurement volume produces an interference fringe pattern shown in Figure 5.2.

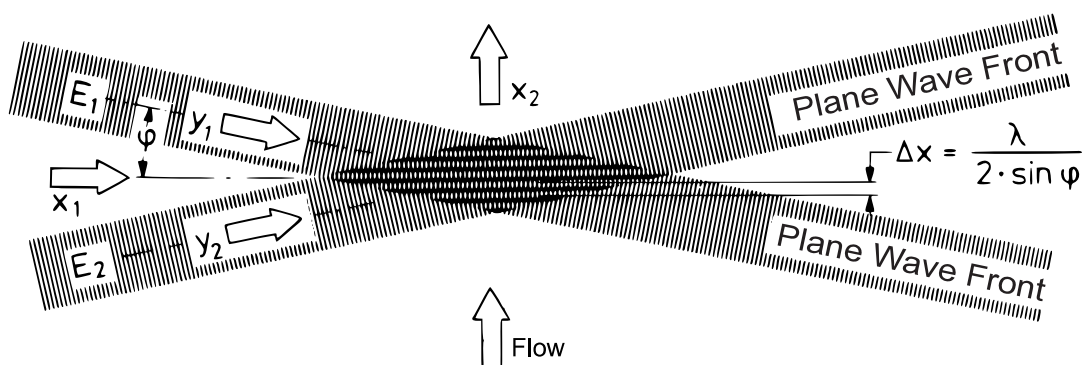


Figure 5.2: LDA interference fringe pattern [47] modified

The distance between the fringes  $\Delta x$  can be calculated depending on the relation in equation (5.4)

$$\Delta x = x_{2,n+1} - x_{2,n} = \frac{\lambda}{2 \sin \varphi} \quad (5.4)$$

Particles passing this pattern consisting of dark and bright fringes scatter light in a frequency that is related to its velocity through the measurement volume. The detected frequency is proportional to the velocity component normal to the fringe pattern:

$$\Delta f = \frac{u_{normal}}{\Delta x} \quad (5.5)$$

$$u_{normal} = \frac{\Delta f \lambda}{2 \sin \varphi} \quad (5.6)$$

Hence applying two different fringe patterns based on two particular wavelengths of the lasers to the interesting volume leads to two velocity components in one plane.

The detected signals or so called Doppler bursts include the frequency shift of both waves which are superimposed and the Beat or Doppler frequency can be derived out of that. Lasers usually used for LDA systems have a Gaussian beam shape (TEM<sub>00</sub>), as a consequence the detected burst signal bears a similar type of shape shown in Figure 5.3.

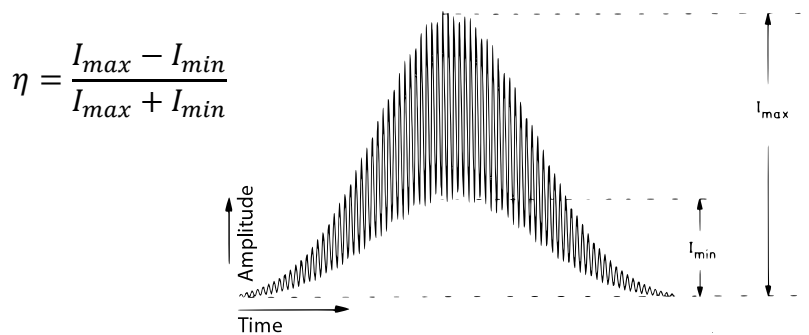


Figure 5.3: Doppler Burst [47] modified

For statistical reasonability the data rate has to be kept high which means a lot of particles have to pass the measurement volume simultaneously. In order to process this high amount of data burst spectrum analyzers have to be applied (BSA). The influence of the particle size when passing the measurement volume is illustrated in Figure 5.4. Particle sizes have to be determined in advance in order to define the reasonability of the results. Using seeding in gaseous flows is a method which produces sizes of distinct amount usually in the range of 0,3 - 0,5  $\mu\text{m}$ . signals consisting of multiple bursts can show a phase shift Figure 5.4 III and V. usually the so called visibility  $h$  is used when defining the quality of the scattered signal (Figure 5.3).

- Droplet diameter  $d_p = \Delta x / 2$  represents the ideal case for which the visibility  $h=1$  case I in Figure 5.4.
- $d_p < \Delta x$  or  $d_p > \Delta x$  is the most common case and results in a visibility of  $0 < h < 1$
- $d_p = \Delta x$  the worst case and results in a visibility of  $h = 0$

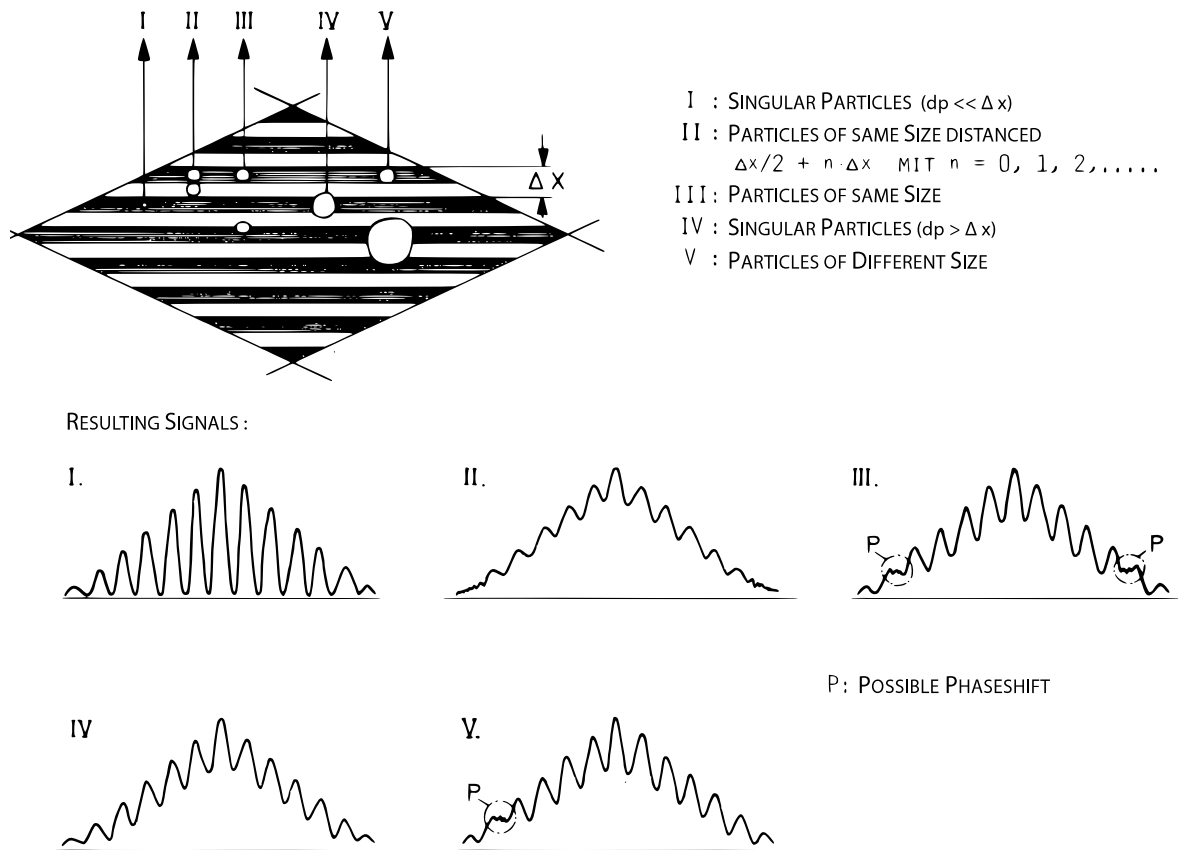


Figure 5.4: Fringe pattern and related Doppler burst signals depending on particle size [47] modified

Simple LDA systems are not able to differentiate from which direction the particles cross the measurement volume, even if the Doppler signal includes a velocity information. Therefore one of the separated beam parts is modulated by an acousto-optic modulator, a so called Bragg cell. This component shifts the frequency of one splitted beam using ultrasonic waves which results in a fringe pattern that is moving with a certain velocity. Particles moving in the direction of the moving fringes do show a lower frequency than in the opposite direction. This way the direction of the particles can be defined, which is very important especially for turbulent flows.

Practically two different types of LDA system configurations are used:

- Dual beam configuration

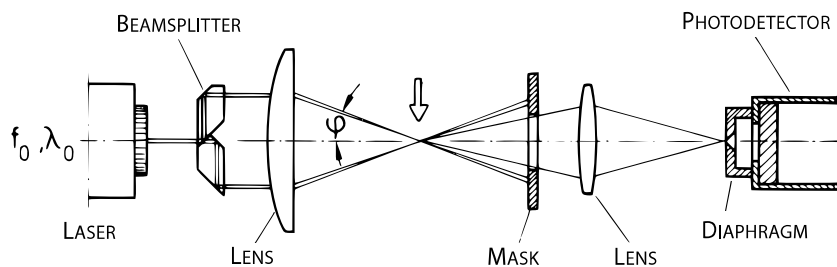


Figure 5.5: Dual beam configuration LDA system [47] modified

The dual beam configuration is characterized by a separation of the laser beams into 2 beams of same intensity (50/50 %) and a concentric positioning opposite to the laser (front scattering mode) or on the same side as the laser (back scattering mode). This configuration makes the system direction independent for the detection of the signal and allows a large modulation range.

- Reference beam configuration

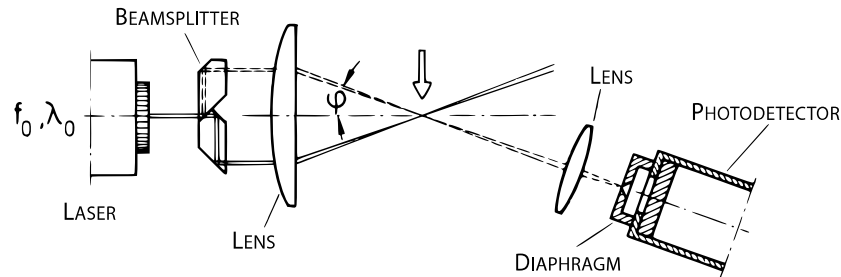


Figure 5.6: Reference beam configuration LDA system [47] modified

In the reference beam configuration, the photo detector is positioned in the direction of one of the splitted laser beams. This way only the light scattered by the opposite beam is Doppler shifted, consequently the received signal is the original superimposed with a Doppler shifted wave. The system is difficult to calibrate because of the intensity difference between the splitted laser beams and therefore is not used very often anymore.

### 5.1.2 Configuration

The system used for this contribution is a two component LDA system by DANTEC (DANTEC Fiber-Flow with Burst Spectrum Analyzers).

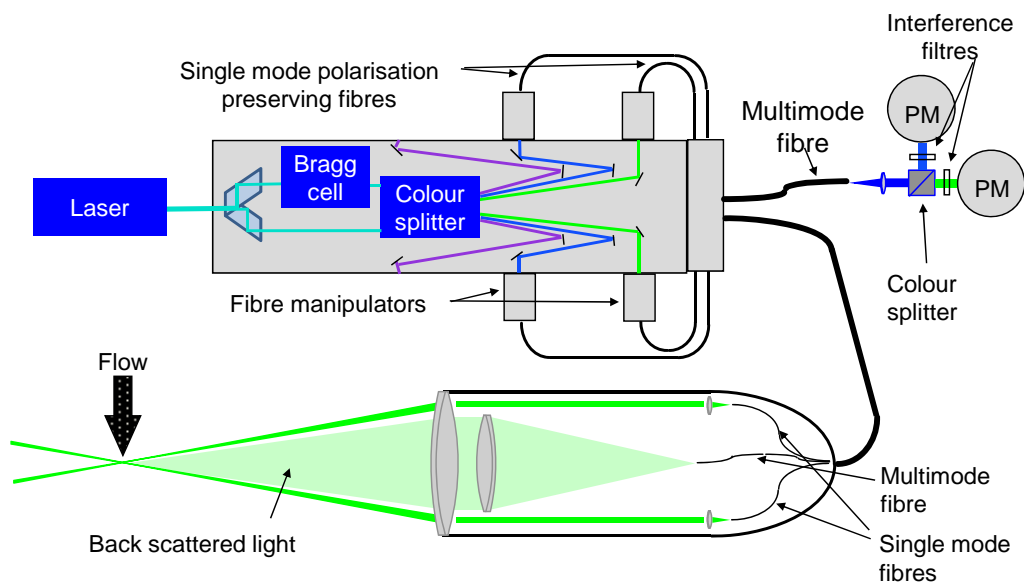


Figure 5.7: Dantec two component backscatter LDA [48] modified

The laser used is a CW Argon-ion Laser split by a color splitter into wavelength  $\lambda = 488 \text{ nm}$  and  $514,5 \text{ nm}$ . The system is of type backscatter mode and is traversed with a mechanical unit as well

by DANTEC which can be controlled by the BSA flow software parallel to data acquisition. The measurement grid has been run through automatically. As scattering particles Di-Ethyl-Hexyl-Sebacin-Ester droplets produced by a so-called seeding generator were used. The produced particles have a mean diameter of approximately  $d = 0,5 \mu\text{m}$ .

## 5.2 Infrared Extinction Method

In order to optimize existing evaporation models such as the later on mentioned CEDRE code from ONERA as well as defining and characterizing evaporation mechanisms, it is important to be able to measure the vapor phase in fuel injection systems of turbo and piston engines. The technical possibilities on the market for such analyses are reduced. Not a lot of techniques are known to be used for reasonable vapor concentration measurements. One example is the Laser induced fluorescence (LIF) which uses radiation emission of hydrocarbon molecules released from an excitation by high power laser radiation to characterize the vapor phase. This specific method has its disadvantages in the sensitivity range due to its tendencies of blooming at phase transitions and as a consequence saturation concerning the optical data acquisition chain that results in useless data for these concerned areas. These facts influence immensely the accuracy of this technique. However it is widely used for industry purposes.

A commercially cheaper and less sensitive measurement technique concerning blooming and saturation effects is represented by the so called Infrared extinction method (IRE). There are a lot of investigations found in literature using this technique, having started in the end of the seventies of the last century a big evolution of this method had been developed especially in the beginning of the nineties by James Drallmeier [53].

The Infrared extinction or absorption method is based on the effect of light extinction due to the presence of absorbing molecules. According to this the molar concentration can be determined by measuring the extinction of electromagnetic radiation alongside the optical path directed through a test section. Initially this effect has been used for the determination of soot production and oxidation in combustion chambers and cylinders of engines.

In order to get information about the presence of gaseous Hydrocarbon concentration the light extinction for the Infrared range which is proportional to the molar vapor concentration is being measured.

### 5.2.1 Technical fundamentals

#### 5.2.1.1 Absorption process

The extinction of Infrared light directed through a gaseous concentration of hydrocarbons such as gasoline is based on the following theoretical background:

The interaction between electromagnetic radiation in the infrared wavelength range and a molecule basically results in a transition of oscillation and rotation within the molecule. The radiation energy is being absorbed and transmitted into kinetic energy generating oscillations and rotations of the basic molecules. The frequency of this absorption oscillation depends on the binding strength of the molecules and is typically positioned in the range of a few micrometers wavelength. The rotational transitions depend on the inertial momentum of the molecule and are typically within a range of a few millimeters of wavelength.

### Spectra of rotation and oscillation of a 2-atomic molecule

Near the potential minimum on the position  $R_0$  the definition for the potential energy  $V$  of molecules based on a composition of 2 atoms can be formulated using a parabola with a constant force-parameter  $k$ :  $V=1/2*k*(R-R_0)^2$ . The reformulation of the equation of Schrödinger results in the oscillation energies expressed by the oscillation terms using wavenumbers.

$$G(\nu) = \left(\nu + \frac{1}{2}\right) \frac{\sqrt{k/\mu}}{2\pi c} \quad (5.7)$$

$\mu$  stands for the reduced mass of the molecules:  $1/\mu=1/m_1+1/m_2$  and  $\nu$  is the quantum number of the oscillations with  $\nu = 1, 2, 3, \dots$

Molecule spectroscopy mainly uses wave-numbers  $\tilde{\nu}$  instead of wave-lengths. The wave number is defined as  $\tilde{\nu} = \nu/c = 1/\lambda$ , where  $c$  stands for light speed in a vacuum and  $\nu$  for its corresponding frequency.

From the rotational terms it can be formulated:

$$F(J) = \left(\frac{\hbar}{4\pi c I}\right) I (J + 1) \quad (5.8)$$

$I$  stands for the rotational inertia momentum of the molecule with the rotation quantum number  $J=1, 2, \dots$   $\hbar$  is the reduced Planck constant defined as  $\hbar = h / 2 \pi$ .

Rotation oscillation terms  $S(\nu, J)$  are composed by the terms for rotation and oscillation:

$$S(\nu, J) = G(\nu) + F(J) \quad (5.9)$$

Permitted transitions are characterized by a certain rule for selection, for oscillation transition it is  $\Delta\nu=\pm 1$  and for rotation transition  $\Delta J=\pm 1$

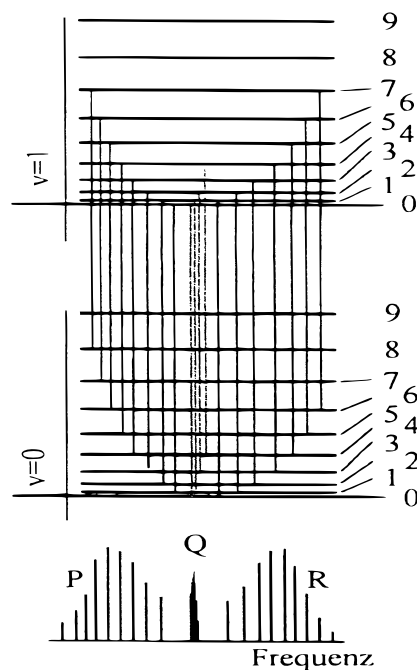


Figure 5.8: P Q R sectors of the rotation-oscillation spectrum [52]

During a transition of oscillation from  $\nu=0 \rightarrow \nu=1$  the rotation quantum number  $J$  changes with  $\Delta J=\pm 1$ . For the constraint that the molecule has an orbital angular momentum around its axis also the transition of  $\Delta J=0$  is permitted. As a consequence the absorption lines can be classified in 3 sectors see Figure 5.8: transitions  $\Delta J=0$  for the Q sector, whose transition frequency is according to its oscillation energy,  $\Delta J=-1$  for the lower frequency range of the P-sector and  $\Delta J=+1$  for the higher frequency range of the R-sector. [52]

### Transition Intensity

The induced absorption stands for the transition of a molecule from a lower energy level to a higher one. This transition is induced by radiation in the transition frequency. The probability of the transition of the molecular absorption is defined as follows:

$$W = B * \rho \quad (5.10)$$

$\rho$  stands for the radiation intensity and  $B$  is the Einstein coefficient of the absorption. If the molecule is already in an excited level it can also be transformed in a less energetic level by radiation. The propability for this process is defined as follows:

$$W' = B' * \rho \quad (5.11)$$

Where  $B'$  is the Einstein coefficient of the Emission.

There is also a possibility that the molecule spontaneously is transduced into a lower energy level.  $A$  stands for the propability of the transition into spontaneous emission. Based on the investigations of Einstein it was possible to prove that the coefficients for induced absorption and emission are the same and that the spontaneous emission is related to the induced emission according to the following equation:

$$A = \left(\frac{8\pi h\nu^3}{c^3}\right)B \quad (5.12)$$

The spontaneous emission is dependend on the frequency. For the absorption concerning the infrared wavelength range spontaneous emission can be neglected. Concerning the netto absorption of  $N$  particles in the basic energy level and  $N'$  particles in the excited energy level it can be formulated:

$$W = (N - N') B \rho \quad (5.13)$$

It is proportional to the difference of the occupation numbers of the participating levels which is defined by the Boltzmann distribution:

$$\frac{N_i}{N_j} = e^{-\frac{E_i - E_j}{kT}} \quad (5.14)$$

$N$  stands for the number of particles in the corresponding energy levels  $E$ ,  $T$  is the temperature and  $k=1.38 \cdot 10^{-23}$  is the Boltzmann constant.

In order to interact in an electric field the molecule must have at least a temporary dipole moment. The transition dipole moment  $\mu_{12}$  between the level 1 and 2 describes the amount of load redistribution of a molecule during the transition. Only if the transition dipole moment is different

to zero the line can appear in the spectrum and the molecule is active in the Infrared range. The Einstein coefficient of the induced Absorption and Emission is proportional to the square of the transition dipole moment. [52]

### Absorption band of the C-H Valence oscillation

Molecules with heteroatoms always have a dipole moment and therefore are active in the infrared range. Figure 5.9 shows the transmission spectrum of gaseous methane in the range between wavenumbers  $3200\text{ cm}^{-1}$  and  $2800\text{ cm}^{-1}$ .

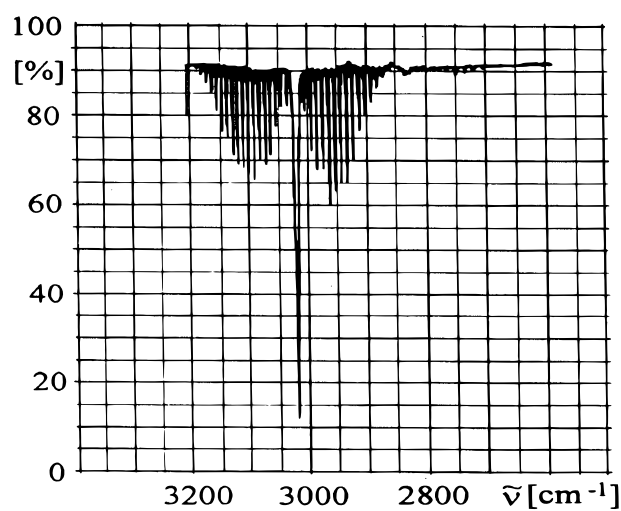


Figure 5.9: Transmission spectrum of methane [52]

The maximum absorption is positioned at a wavenumber of  $3020\text{ cm}^{-1}$  which is according to the C-H valence oscillation without a change in the angular momentum. Valence oscillation is the periodic movement of the molecule alongside its bond axis.

The resolution of the rotation's fine structure can be identified here. This structure can be observed for gaseous molecules at low pressure level only. Increasing pressure leads to numerous impulses and a lower residence time of the rotational state. Thus the lines of the fine structure are broadened until only the band of the C-H rotation-oscillation spectrum can still be detected. The C-H rotation-oscillation band of n-tridecan is shown in Figure 5.10. n-tridecan is very similar to kerosene Jet A1 concerning its physical and chemical properties (referring to [52])

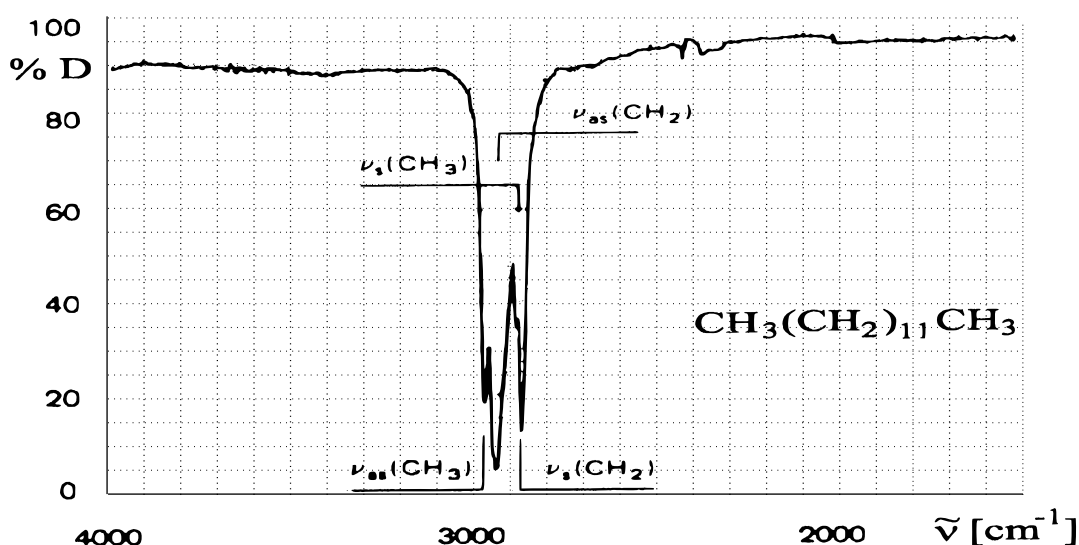


Figure 5.10: Absorption spectrum of liquid n-tridecan [52]

Because of the lower mass of the hydrogen atom opposed to the mass of the carbon atom also the carbon oscillation amplitude is of negligible amount and therefore is only peripherally influenced by the remaining bonds. Hence the absorption band of the C-H valence oscillation in the range of the wavenumbers  $2850\text{ cm}^{-1}$  -  $2960\text{ cm}^{-1}$  ( $3370\text{ nm}$  -  $3500\text{ nm}$ ) is typical for most hydrocarbons.

A characteristic wavelength for radiation emitted by Helium-Neon lasers in the infrared range is  $3390\text{ nm}$  ( $2850\text{ cm}^{-1}$ ). Alkanes react with valence oscillations in this wavelength which is mainly based on the valence oscillation of the methyl and methylene groups (see Figure 5.11).

Basic oscillation modes are symmetric ( $\nu_s$ ) and anti-symmetric ( $\nu_{as}$ ) valence oscillations of the methyl and methylene group. Their position within the n-tridecane absorption band is shown in Figure 5.10

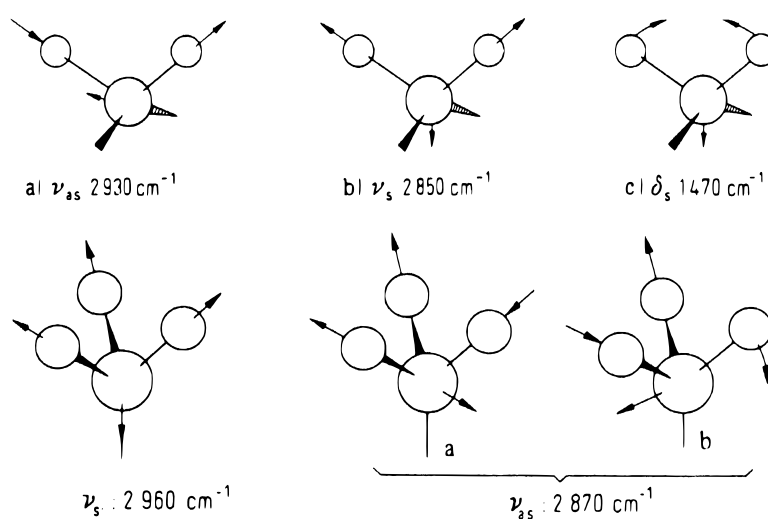


Figure 5.11: Oscillations of the  $\text{CH}_2$  fragments (top) and the methyl groups (bottom) (big sphere  $\rightarrow$  C-atom, small sphere  $\rightarrow$  H-atom) [52]

The strength for the valence bond  $S = \int k(\nu) d\nu$  of liquid alkanes except for methane is proportional to the amount of hydrocarbon atoms per unit volume.  $k(\nu)$  stands for the absorption index which is the imaginary part of the complex refraction index. Investigations of Pinkley et al. [61] have shown that the calculation of the mean value of the bond strength according to the mean amount of the Hydrogen atoms in [mol/litre] has a mean deviation of 6,5 %. Although the mean deviation of the absorption of Helium Neon lasers at 3.39  $\mu\text{m}$  wavelength is slightly higher it is possible to determine the mean amount of Hydrogen atoms per volume from Absorption measurements within this band using the Beer-Lambert law. [52]

### The Beer-Lambert law

For coherent light using wavelength  $\lambda$  directed through an absorbing medium in a geometrically defined measurement volume, where L is the penetrating length,  $\alpha(p, t, \lambda)$  the corresponding absorption coefficient of the absorbing medium and C the molar concentration the Beer Lambert Law can be formulated:

$$\frac{I}{I_0} = e^{-\alpha(\lambda) C L} \quad (5.15)$$

$I/I_0$  stands for the intensity ratio or extinction ratio and is the relation between incoming and outgoing light. The relation of the above introduced absorption coefficient  $\alpha(p, t, \lambda)$  and the absorption index  $k(\nu)$  is expressed in

$$k(\nu) = \frac{\alpha(\lambda)C}{4\pi\nu} = \frac{\alpha(\lambda)C\lambda}{4\pi} \quad (5.16)$$

Solving this equation for the mean concentration in the line of sight results in

$$C = \frac{\ln(\frac{I}{I_0})}{\alpha L} \quad (5.17)$$

Knowing the deflation of the light intensity, the characteristic absorption coefficient and the penetrating length L through the medium the concentration C can be determined. [52]

#### 5.2.1.2 Evaporation model

##### The $d^2$ law

In case of a droplet introduced into an environment where temperature and pressure exceed the evaporation limits of the liquid, it starts to vaporize and forms a gaseous fuel air mixture. This effect is related to several physical effects which makes it quite difficult to form a mathematical model for this process. A quite simple approach to model the evaporation mechanisms is the so called  $d^2$  law.

This law describing the simple evaporation of an isolated single droplet has been developed by Spalding in 1951 [50] and assumes the following simplifications for his approach [56]:

- A perfect sphericity of the isolated droplet being immobile in a static gaseous environment, which results in an one dimensional system
- The droplet consists of a mono-composant liquid
- The process is quasistationary
- The evaporation is faster than the transport of the vapor in the surrounding air
- Heat flux by radiation is negligible
- No gas is soluted in the liquid phase
- The droplet temperature is constant and uniform
- Gas properties such as the vapor density  $\rho_{vap}$  and the diffusion coefficient  $D$  are constant and the Lewis number  $L_e = \lambda_{vap}/\rho_{vap} C_{p-vap} D$  equals 1
- The process is isobar

Firstly the droplet is surrounded by air only, the ambient heat contributes to the heating of the droplet as well as to the evaporation. It is considered that the evaporation happens instantaneously at the droplet surface which results in a local vapor air mixture which is then transferred by convection with a radial velocity only, the so called Stefan-flow. While  $Y_{l,r}$  stands for the vapor mass fraction for the given radius  $r$ ,  $d_{drop}$  for the droplet diameter,  $Y_{l,\infty}$  for the mass fraction at infinity and  $Y_{l,s}$  for the mass fraction at the surface, the evaporation rate is expressed as follows:

$$\frac{dm_{drop}}{dt} = -2 \pi d_{drop} \rho_{vap} D \ln\left(\frac{1 - Y_{l,\infty}}{1 - Y_{l,s}}\right) \quad (5.18)$$

The droplet mass can be expressed as a function of its diameter

$$m_{drop} = \rho_{drop} \frac{\pi d_{drop}^3}{6} \quad (5.19)$$

A combination of these two equations and a final integration of the resulted expression leads to the so called  $d^2$  law:

$$d_{drop}^2 = d_{drop,0}^2 - \frac{8\rho_{vap}D}{\rho_{drop}} \ln\left(\frac{1 - Y_{l,\infty}}{1 - Y_{l,s}}\right) t = d_{drop,0}^2 - C_e t \quad (5.20)$$

As a consequence it is sufficient to determine  $C_e$  in order to obtain the evaporation time of a droplet. It can be calculated using the law of Clausius - Clapeyron, which provides the saturated vapor pressure and the vapor mass fraction at the surface  $Y_{l,s}$  under the given conditions. By using this law the time span for the complete evaporation of a droplet with known diameter can be estimated. Therefore the left hand side of equation ( 5.20 ) can be set to zero:

$$\tau_{ev} = \frac{d_{drop,0}^2}{C_e} \quad (5.21)$$

Another important value is the Spalding number  $B_M$  which characterizes the mass exchange at the droplet surface

$$B_M = \frac{Y_{1,s} - Y_{1,\infty}}{1 - Y_{1,s}} \quad (5.22)$$

And the Spalding number for heat transfer  $B_T$

$$B_T = \frac{c_{p-vap} (T_\infty - T_{surf})}{L_v} \quad (5.23)$$

With the hereby used assumption of a Lewis number  $L_e = 1$  these two numbers become equal. This model implies very rigorous simplifications and can only be applied to very restricted cases.

### Influence of convection

One of the main inconveniences of the above mentioned correlation is the assumption of a static gaseous phase surrounding the droplet. It has been proven experimentally that there is a drastic influence of convection on the evaporation process. Modelling this influence as proposed by Frackowiak [51] includes the presence of a gaseous film around the droplet in which the thermal and mass transfer takes place. In order to describe these transfer processes inside this film the dimensionless numbers of Nusselt and Sherwood are defined. Using the thermal ( $\delta_T$ ) and mass ( $\delta_M$ ) film thicknesses results in the following definitions:

$$Nu_m = 2 + \frac{d_{drop}}{\delta_T} \quad (5.24)$$

$$Sh_m = 2 + \frac{d_{drop}}{\delta_M} \quad (5.25)$$

These numbers replace the factor 2 in equation ( 5.18 ) for the evaporation rate. As a consequence the boundary layers are approaching an infinite value and  $Nu_m$  and  $Sh_m$  become 2 which is equal to the original expression for the static gaseous phase around the droplet.

Several investigations derived different approaches for these numbers, for example Clift et al. postulated the numbers suchlike:

$$Nu_m = 1 + (1 + Re_p Pr)^{\frac{1}{3}} f(Re_p) \quad (5.26)$$

$$Sh_m = 1 + (1 + Re_p Sc)^{\frac{1}{3}} f(Re_p) \quad (5.27)$$

This kind of definition for the convection model allows to determine global values of the mass and heat transfer. Nevertheless local differences are produced around a droplet by forced convection which are not represented due to the assumption of spherical symmetry.

### The Stefan flow

The Stefan flow transports the vapor in radial direction from the droplet and results therefore in a widening of the boundary layer around the droplet. In order to determine the outcome of this effect the film thicknesses with ( $\delta$ ) and without ( $\delta_0$ ) Stefan flow are compared. A correction function is defined:

$$\frac{\delta}{\delta_0} = f(B) \quad (5.28)$$

$$f(B) = \frac{(1+B)^{0.7} \ln(1+B)}{B} \quad (5.29)$$

B stands for the Spalding number for thermal and mass flow. Using the correction functions  $f_T$  and  $f_M$  the Nusselt and Sherwood numbers can be formulated:

$$Nu^* = 2 + \frac{Nu_m - 2}{f_T} \quad (5.30)$$

$$Sh^* = 2 + \frac{Nu_m - 2}{f_M} \quad (5.31)$$

Finally the resulting equation for the evaporation rate can be written:

$$\frac{dm_{drop}}{dt} = -\pi d_{drop} \rho_{ref} D_{ref} Sh^* \ln(1 + B_M) \quad (5.32)$$

Or with the thermal Spalding number:

$$\frac{dm_{drop}}{dt} = -\pi d_{drop} \frac{\lambda_{ref}}{c_{p,vap} T_{ref}} Nu^* \ln(1 + B_T) \quad (5.33)$$

### 5.2.2 IRE measurement principle in a spray

Fuel-injection systems except for engines fuelled with gaseous combustibles are always characterized by the presence of a two phase flow due to evaporating droplets. For such boundary conditions a simplified consideration of the modes of extinction using the aforementioned Beer Lambert law is not sufficient. Figure 5.12 shows the 3 modes of extinction of induced coherent light on droplets.

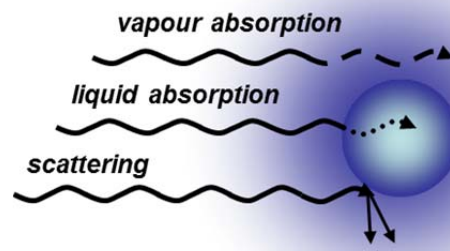


Figure 5.12: Modes of extinction on a droplet

Additionally to the vapor absorption in the boundary zone of the droplet two separate modes of extinction have to be taken into account namely the liquid absorption in the droplet and the light scattering due to the droplet surface.

For this consideration the radiative transport equation can be formulated as follows [53]:

$$\begin{aligned} \left(\frac{\bar{I}_x}{\bar{I}_0}\right)_{\lambda_{abs}} &= \exp \left[ -\bar{C}_n L \frac{\pi}{4} \int_0^\infty Q_{sca} D^2 N(D) dD \right] \text{ Scattering} \\ &* \exp \left[ -\bar{C}_n L \frac{\pi}{4} \int_0^\infty Q_{abs} D^2 N(D) dD \right] \text{ Liquid Absorption} \quad (5.34) \\ &* \exp \left[ -\int_0^l \alpha_{(\lambda,p,T)} c_m(x) dx \right] \text{ Vapor Absorption} \end{aligned}$$

$\bar{C}_n$  stands for the line-of-sight averaged number density,  $N(D)$  for the drop diameter distribution.  $Q_{sca}$  and  $Q_{abs}$  are the scattering and absorption efficiencies. Consequently, the determination of the vapor concentration  $c_m(x)$  (or, after integration, of its integral value  $c_m$ ) requires knowledge of the drop diameter distribution  $N(D)$ , the two extinction efficiencies  $Q_{sca}$  and  $Q_{abs}$  and the line-of-sight averaged number density  $\bar{C}_n$ . The first one can be measured by the use of a laser diffraction technique. The extinction efficiencies are determined by Mie-theory computations, knowing the wavelength dependent refractive index of the droplets from literature if available. The number density may be obtained with an extinction measurement at a non-absorbing wavelength  $\lambda_{na}$  since it is wavelength-independent and in this case scattering by the droplets is the only mode of extinction.

The IR (absorbing) wavelength has been chosen due to the absorption spectrum of most common hydrocarbons lying between 3370 nm and 3500 nm (see Figure 5.13) as mentioned above and the emitting spectrum of commercial HeNe lasers in the infrared range of 3,39  $\mu\text{m}$ .

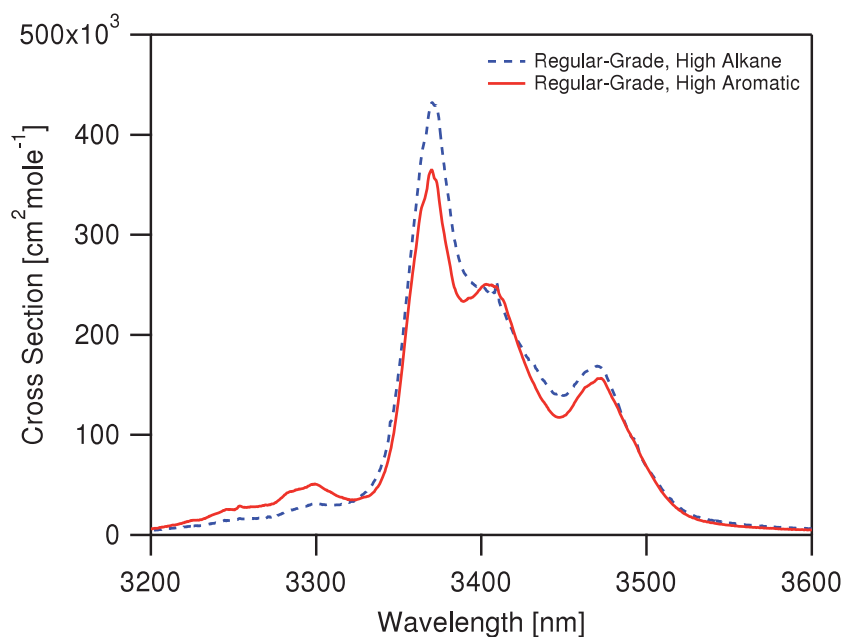


Figure 5.13: Absorption spectrum of typical hydrocarbons in cross section [ $\text{cm}^2/\text{mole}$ ] [59]

As a conclusion we can note that for a determination of the mean concentration value of the fuel vapor  $c_m$ , two extinction measurements, one absorption measurement and two calculations for averaged number density  $\bar{C}_n$  would be necessary. This represents a lot of experimental and numerical effort for just one measurement and would render the IRE practically impossible to use for research or for industrial application. In 1994 Drallmeier published a simplification to the IRE evaluation process [53]. The main hypothesis is that if the line-of-sight extinction due to Mie-scattering is similar for both infrared and visible wavelengths because of the presence of the spray, only infrared light will be absorbed by the fuel vapor, being transparent to visible light. A comparison between line-of-sight intensities  $I_{\text{IR}}$ ,  $I_{\text{VIS}}$  of both wavelengths allows to estimate the vapor concentration.

The simplification is based on a mathematical reformulation of the radiation transport equations for two wavelength ranges. One in the visible range of 633 nm and one for the characteristic absorbing wavelength in the IR range of 3390 nm. firstly for the absorbing wavelength (IR). The optical thickness  $\tau_{\text{ABS}}$  replaces the first two parts of the equation which represent the extinction by scattering and liquid absorption. The absorption efficiencies are combined as  $Q_{\text{ext}}$ .

$$\tau_{\text{ABS}} = \bar{C}_n L \frac{\pi}{4} \int_0^{\infty} Q_{\text{ext}} D^2 \bar{N}(D) dD$$

$$Q_{\text{ext}} = Q_{\text{abs}} + Q_{\text{sca}} \quad (5.35)$$

$$\bar{c}_m(x) = \frac{1}{\alpha L} \left[ -\tau_{\text{ABS}} - \ln \left( \frac{\bar{I}_x}{I_0} \right)_{\lambda_{\text{ABS}}} \right]$$

For the non-absorbing wavelength (NA) it is assumed that there is no extinction of the laser beam due to the vapor and the liquid phase, the beam intensity is only reduced by droplet scattering.

$$\tau_{NA} = \bar{c}_n L \frac{\pi}{4} \int_0^{\infty} Q_{sca} D^2 N(D) dD = \ln \left( \frac{I}{I_0} \right)_{na} \quad (5.36)$$

The optical thickness for the non-absorbing wavelength can be introduced into the equation of the molar vapor concentration for the absorbing wavelength. The ratio  $\tau_{ABS}/\tau_{NA}$  is defined as optical thickness ratio R.

$$\begin{aligned} \bar{c}_m &= \frac{1}{\alpha L} \left[ -\tau_{NA} \left( \frac{\tau_{abs}}{\tau_{na}} \right) - \ln \left( \frac{I}{I_0} \right)_{abs} \right] \\ &= \frac{1}{\alpha L} \left[ -\ln \left( \frac{I}{I_0} \right)_{na} R - \ln \left( \frac{I}{I_0} \right)_{abs} \right] \end{aligned} \quad (5.37)$$

$$R = \int_0^{\infty} \frac{(Q_{ext})_{abs} D^2 \overline{N(D)} dD}{(Q_{ext})_{na} D^2 \overline{N(D)} dD} = \frac{\tau_{abs}}{\tau_{na}} \quad (5.38)$$

Pommersberger [63] calculated the optical efficiencies for absorption, scattering and extinction for Kerosene Jet A1 varying the droplet diameters, based on a method developed by Lui et al. [64] and van de Hulst [65] for visible and infrared light which is presented in Figure 5.14.

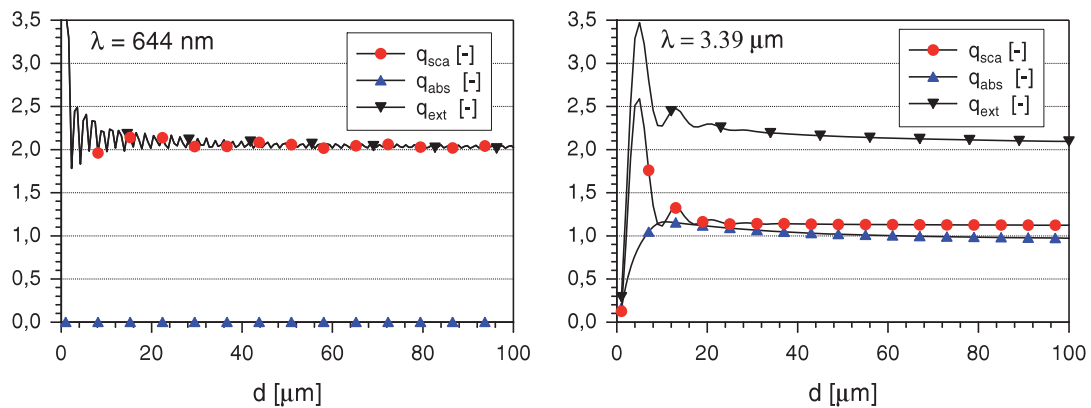


Figure 5.14: Optical efficiencies of absorption scattering and extinction of visible and infrared light on fuel droplets [63]

A typical phase complex refractive index is  $n-ik=1,44-0,067i$  for iso-octane near room temperature. Mie-scattering calculations by Drallmeier [53] varying the real and imaginary part of the refractive index  $m$  for drop sizes between 1 and 200  $\mu\text{m}$  presented in Figure 5.15 show that there is little influence of this parameter variation on the optical thickness ratio. Regardless of the index variations it can be seen that R varies less than 10 % for drops diameters above 30  $\mu\text{m}$ .

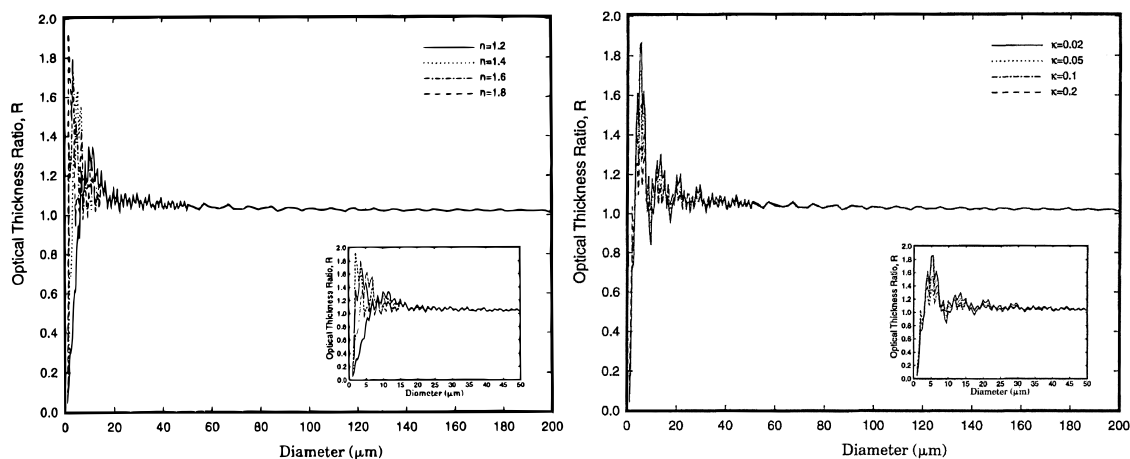


Figure 5.15: Optical thickness ratio / Area mean diameter and a variation of the real part of the liquid phase refractive index  $n$  and the imaginary part of the refractive index  $\kappa$  [53]

Fuel spray drop size distributions can be approximated using Log-normal distributions [66]. equation ( 5.39 ) defines the mathematical formulation of this distribution [66]. Varying the parameters  $\overline{D}_{ng}$  and  $s_g$ . Drallmeier calculated the Optical thickness ratio and identified the area mean diameter as best correlating mean diameter definition.

$$\frac{dN}{dD} = f(D) = \frac{1}{\sqrt{2\pi}Ds_g} \exp - \frac{1}{2s_g^2} (\ln D - \ln \overline{D}_{ng})^2 \quad (5.39)$$

With this definition it was possible to show that the optical thickness ratio  $R$  can be assumed being 1.0 if the area mean drop diameter is  $D_{20} > 20 \mu\text{m}$  implying a measurement error of 10 %. An error analysis will be detailed later on.

$$D_{20} = \left[ \frac{\sum N(D)D^2 dD}{\sum N(D)dD} \right]^{1/2} \quad (5.40)$$

As a result, no more separate scattering measurements or Mie-calculations are required to determine the line-of-sight vapor mole fraction. Taking the mentioned measurement error into account the IRE is reduced to two extinction measurements at the employed wavelengths and presents the basis for real-time analysis of sprays with this technique.

For an extinction characterization only the intensities for both wavelengths have to be measured. These intensities will always be normalized with a reference signal in absence of the spray, which represent the direct transmission intensities that are marked with a "0" underscript. As a consequence the line-of-sight intensities  $I_{VIS}$ ,  $I_{0\ VIS}$ ,  $I_{IR}$  and  $I_{0\ IR}$  have to be measured.  $\alpha_{IR}$  is the vapor absorption coefficient in the IR range, and  $L$  is the length of the laser penetration through the medium. While the product  $\alpha_{IR} L$  is constant at isothermal conditions, the relative concentration can be computed. Since the IRE is a line-of-sight-type technique, the obtained results are integrated over the whole length of the measured area. To get spatially resolved results, deconvolution procedures have to be applied to the data. One of the classic deconvolution schemes for axis-symmetrical geometries such as sprays or spherical objects is the 'Onion-peeling-scheme' as presented by Hammond 1980 [62].

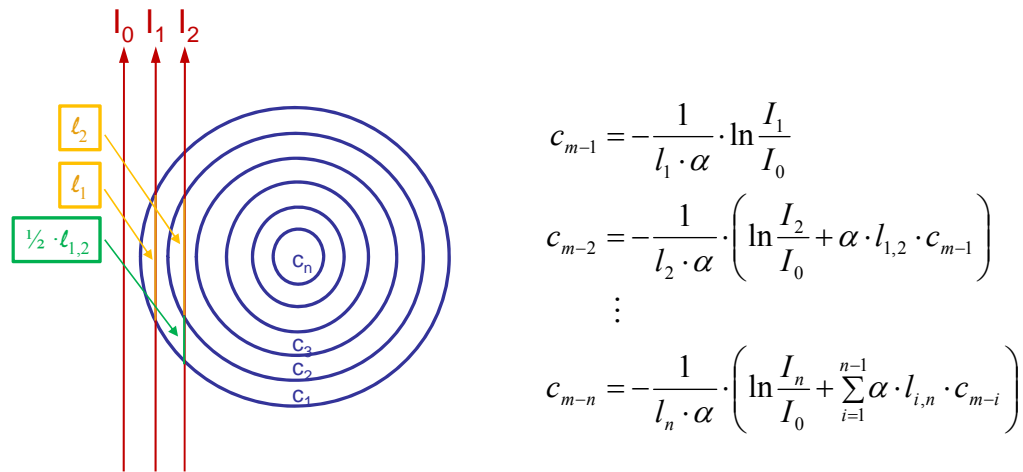


Figure 5.16: Onion Peeling algorithm based on investigations of Hammond [62]

The algorithm takes  $n$  measurement points of the performed grid and divides it into a System of  $n$  equations for  $n$  unknown concentrations. These concentrations are assumed to be constant within the step size of  $dx$  between the measurement points (see Figure 5.16). Taking these assumptions into account it is possible to compute point results for the molar concentrations within the fuel mixing zone.

## 5.2.3 Error analysis

### 5.2.3.1 Fuel composition

One of the main error sources for the determination of the fuel vapor concentration by absorption measurements in kerosene sprays derives from the high diversity of the chemical compositions of kerosene mixtures and the different corresponding boiling points. The strength of the absorption bands of liquid alkanes is proportional to the amount of hydrogen atoms with a deviation of about 6.5 % except for methane where it is nearly 40 % [61]. Due to the fact that the absorption is measured for a fixed wavelength within this absorption band the error can be of a higher magnitude than expected. Pinkley et al. presented absorption maxima of alkanes, which compared to each other are characterized by a standard deviation of 10 %. This value of 10 % is the error for the concentration determined with the Infrared extinction method being proportional to the amount of hydrogen atoms. [52]

### 5.2.3.2 Droplet scattering

Another error source can be found in the absorption of infrared light by the droplets. Brandt calculated the extinction due to the droplets for different pressure levels at elevated temperatures [52]. The mean droplet diameter distributions have been determined by a phase Doppler anemometry characterization. His calculations using a Mie-scattering code from Giese resulted in the following error amounts dependent on different mean diameters in Figure 5.17.

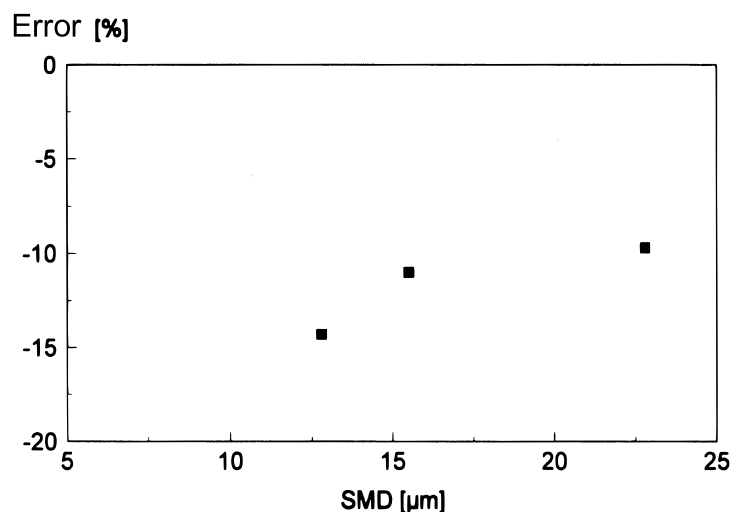


Figure 5.17: Error of the droplet absorption and scattering at a wavelength of  $3.39 \mu\text{m}$  by droplet scattering at a visible range of  $633 \text{ nm}$ . [52]

The corresponding complex refractive indices were  $k + i \cdot n = 1.44 + i \cdot 0$  for  $633 \text{ nm}$  and  $1.44 + i \cdot 0.058$  for  $3.39 \mu\text{m}$  wavelength.

Figure 5.17 shows the error amount that derives from a replacement of the droplet absorption and scattering at  $3.39 \mu\text{m}$  by the scattered light at  $633 \text{ nm}$ . It can be seen that for the measured particle size distributions the amount of extinction is lowered for about 10-15 percent. The deviation tends being higher towards smaller mean particle sizes. For bigger particles the extinction efficiency approaches a value of 2 (see Figure 5.14). As a consequence the error can be assumed being smaller for bigger mean diameters. This measurement error of about 15 % mainly affects dense sprays where the amount of scattered light on the droplets is high. For the requirements of this contribution due to the relatively small extinction of the visible light in comparison to the infrared light, the suchlike achieved error can be denoted with about 1-2 %. [52]

### 5.2.3.3 Pressure and temperature dependency

Figure 5.18 shows the evolution of the absorption coefficient of pure alkanes alongside temperature and pressure variation. It can be seen that the pressure evolution of the absorption coefficient at any temperature does not follow any predictable trend, it is more or less fluctuating. An explanation for this is that while the absorption line is broadened the intensity of the transition remains at a certain level. Consequently the absorption maxima are reduced, while in the boundaries of the band the intensity is increasing. The symmetric valence oscillation frequency of the methylene group is  $2930 \text{ cm}^{-1}$  and the anti-symmetric is  $2850 \text{ cm}^{-1}$ , on the other hand for the methyl group the valence oscillation frequency has an amount of  $2960 \text{ cm}^{-1}$  for the symmetric and  $2870 \text{ cm}^{-1}$  for the anti-symmetric. As a consequence it is not explicit if the widening of the band is leading to a stronger or weaker absorption at  $3.39 \mu\text{m}$  ( $2950 \text{ cm}^{-1}$ ). Brandt denoted the predicted error due to pressure variation being  $< 10 \%$ .

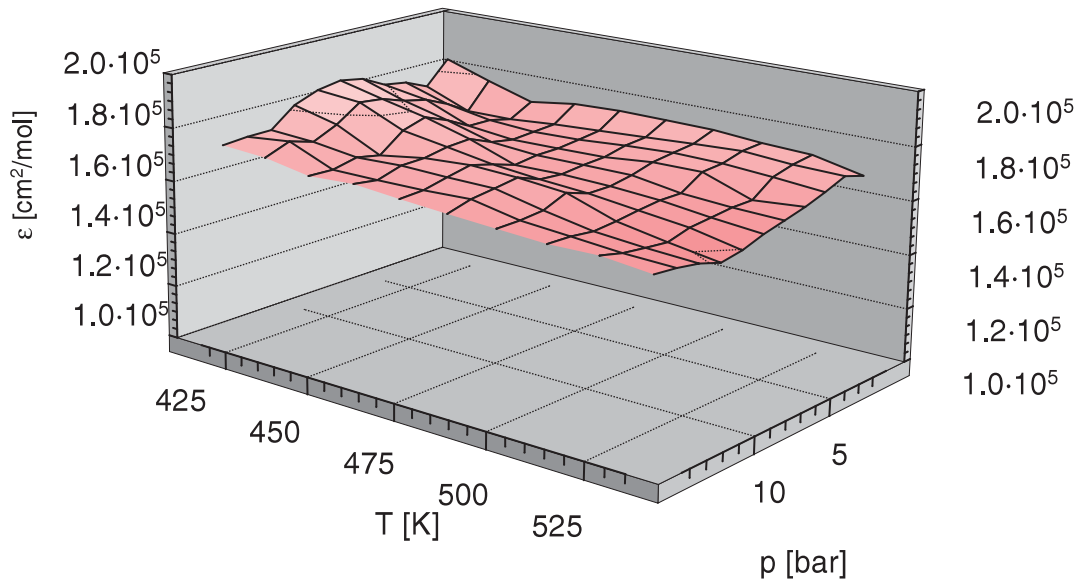


Figure 5.18: Temperature- and pressure evolution of the decadic absorption coefficient of pure alkanes [63]

The temperature evolution of the absorption coefficient tends to smaller values at higher temperatures. Due to the mean velocity of the molecules the absorption line is widened based on a Doppler shift. The velocity distribution of the molecules is defined by the Maxwell distribution. The mean velocity of the molecules increases with rising temperature and this way influences the widening effect of the absorption line. As a consequence the absorption decreases when the temperature of the investigated medium is rising. The Doppler shift leads to a Gaussian-shaped widening of the absorption line which is defined by equation ( 5.41).

$$\delta\tilde{\nu} = \frac{2\tilde{\nu}}{c} \sqrt{\frac{2kT \ln(2)}{m}} \quad (5.41)$$

Taking the molar mass of the kerosene equivalent  $C_{12}H_{23}$   $M = 2.78 \cdot 10^{-25}$  kg/mol the calculation of the line widening at 850 K yields  $\delta\tilde{\nu} = 0.005 \text{ cm}^{-1}$  and is therefore not relevant for the absorption band of the kerosene. Brandt identified the modification of the chemical composition of kerosene vapor due to oxidation effects and thermal cracking of the hydrocarbon-chains as possible reasons for the decreasing influence on the absorption band.

The overall uncertainty is denoted with 20 % error for dense sprays, which can be reduced for this contribution of being around 10 % due to a small amount of droplets in the air-blast injector which is discussed later on. Two other aspects are to be taken into account in case of non-reproducibility of a test case: the motion / deformation of the windows stressed by pressure and temperature gradients, and the possible progressive deposition of dirt on the inner windows, but are not supposed to produce more than 1-2 % of uncertainty. [52]

Despite this quite high amount of uncertainty it can be sad that, compared to other measurement techniques which maybe more precise and reliable (such as Rayleigh scattering/spectrometry), this method is relatively lightweight and suits well for systematic comparisons.

# Chapter 6

## Test Rig

### 6.1 Hot/Cold Flow facility

The test rig in the laboratory of the Institute for Thermal Turbomachinery and Machine Dynamics is part of an open-circuit plant which had initially been installed for experimental investigations on cold subsonic and transonic flows. A separate 3 MW compressor station delivers the pressurized air. It consists of two radial compressors (SC14 and SC20) and one double screw compressor (E1+E2). The electrically driven machines can be connected in a highly flexible configuration. Figure 6.1 (a) shows eligible operational modes for the test facility. Generally, air can be provided continuously from 2.5 kg/s up to 15 kg/s with a pressure ratio up to 2.9 kg/s in parallel and up to 8 kg/s at pressure ratio 10 in serial operation mode. Figure 6.1 (b) represents the compressor station characteristics. The air temperature can be adjusted from 140°C down to 35°C through two coolers. The operation of the current system should be able to analyze cooling systems of turbine blades, combustion chambers or to investigate the behavior of high-temperature resistant sensors embedded in gas-turbines [67].

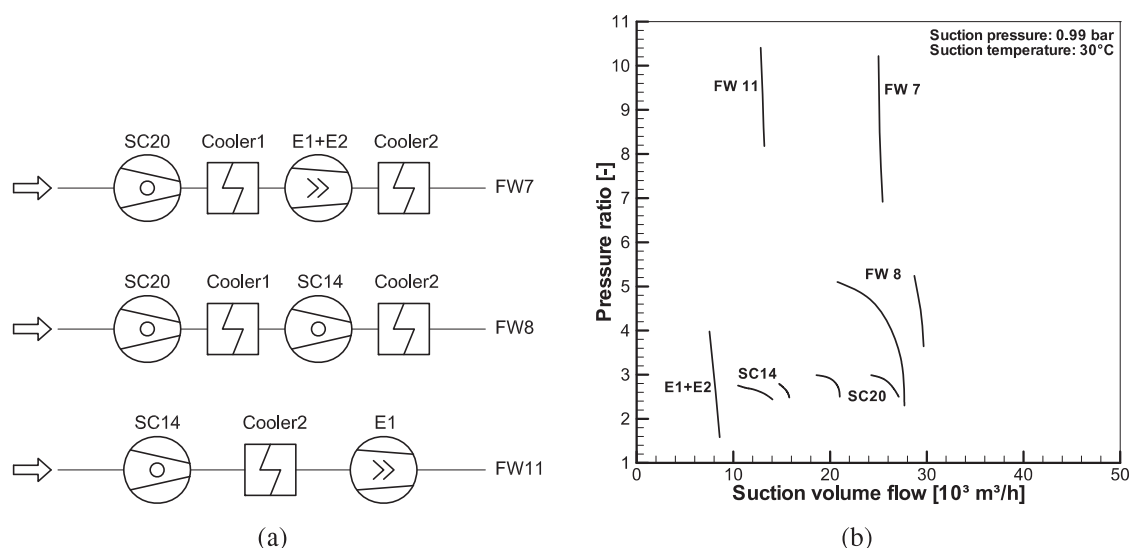


Figure 6.1: (a) Operational modes of the compressor station (b) Characteristics of the compressor station

To fulfill these demands on a modern flow test facility the plant has been extended by an additional piping part which is able to lead the pressurized air flow over a thermal air heater that has been installed on the outside of the institute building. The high pressure air-flow is delivered by the aforementioned compressor station. Leading the pressurized air suchlike by the piping system over the thermal air heater, whose maximum thermal power is denoted with 5MW, allows to realize a maximum system pressure level of 10 bar abs and a maximum temperature level of 750 K in the test cell.

The maximum air flow over the air heater at this test condition is around 3.5 kg/s hot air. The additionally installed part of the open circuit plant is built in parallel of the current system. All operational modes of the compressor station [67] can be used as the adaptation comprises a connection to the high- and low-pressure lines.

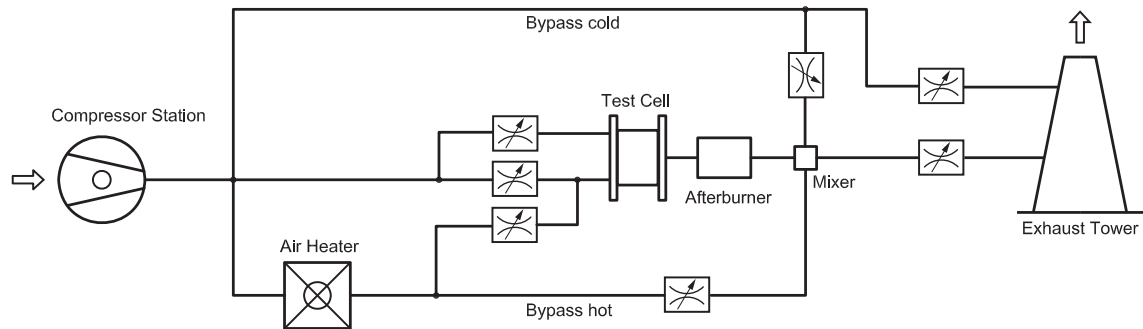


Figure 6.2: Schematic of the test facility

The test rig circuit comprises mainly two line feeds, a hot flow and a cold flow line. Each of these consists of a main line and a corresponding bypass line. The main line for the cold flow is leading directly from the compressor station to the test cell while the hot main line is routed through the air heater first. The bypass lines are split from the main lines before the test cell and are afterwards mixed with the gases obtained inside the test rig. The main intention is to cool down the exhaust gases. The pressure level can be set by a water-cooled butterfly valve. The air flow from the bypass lines to the test cell is regulated by electro-pneumatic valves. The bypass lines and the piping of the air heater are permanent installations. Depending on the application of the test cell the remaining piping can be rearranged or adapted. In case of the investigations for this project an afterburner was installed which is run by methane in order to reduce unburned hydrocarbons in the exhaust-tube, which will later be discussed in detail. A vital arrangement in the whole circuit plant has been the installation of a new fuel supply concept.

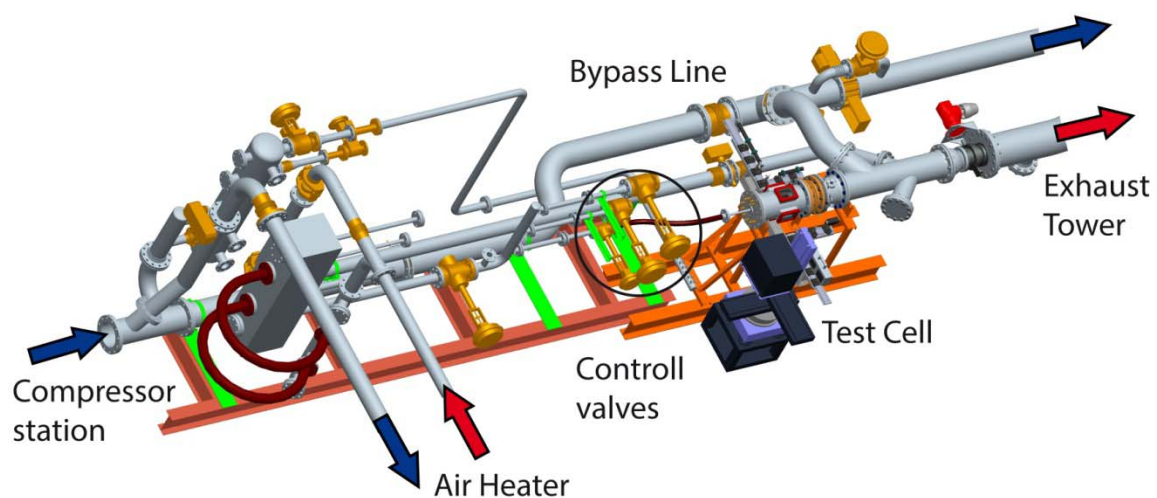


Figure 6.3: 3D Design of the test facility

The Data acquisition and control of the process conditions is performed using a Simatic S7 programmable logic controller (PLC) with appropriate input and output modules. The interface between National Instruments' LabVIEW which is used to visualize and logging the data and the PLC is a DF-Profi-II Profibus card from Comsoft. This setup allows a process update rate of a few ms, by means of which the required process conditions can be comprised in a very stable and precise way.

## 6.2 Fuel supply Feed

The concept of the fuel supply (Figure 6.4 and Figure 6.5) consists of two independent fuel supply feeds with a low and a high pressure pump for each circuit, a surge tank and a recirculation valve and the necessary blocking and safety valves. Both circuits are independently operable and connected with a three way valve. This results in the ability to switch between different fuel types. In this case the tubes leading to the test chamber can be flushed with nitrogen from the internal nitrogen circuit which is connected to the fuel circuit by electromagnetic 3-way valves. With this fuel supply concept it is possible to provide a maximum fuel mass flow of 10 [g/s] at 100 [bar] absolute pressure. The mass flow measurement and regulation is performed by 3 Coriolis mass flow meter/regulator devices (QMBC) delivered by Brooks. The whole setup will be detailed in the following sub-chapter:

### 6.2.1 Schematic of the fuel supply

For a better understanding and overview the illustration of the scheme of the fuel supply feed had been divided into two parts. One illustrates the installations outside the laboratory from the fuel depot area to the combustion laboratory (Figure 6.4) and one for the corresponding installations inside the laboratory (Figure 6.5). The figures are linked at points A and B.

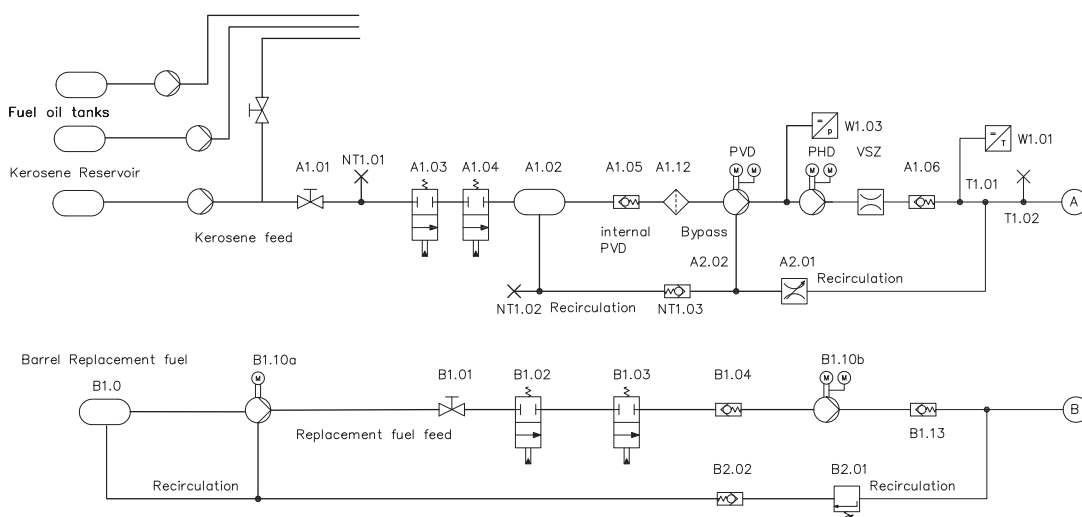


Figure 6.4: Schematic of the fuel supply (fuel depot side)

In the kerosene feed the fuel is aspirated by a low pressure pump from the reservoir over a manually regulated lock-valve and two electromagnetic safety-valves into the surge tank. These valves avoid an overfilling of the tank and are as well connected to the fire prevention installation of the combustion laboratory in order to block the circuit in case of emergency. From this intermediate

tank, into which also the recirculated fuel is led, the mass flow is sucked by a low pressure toothed wheel pump through a non-return valve and a fuel filter (7 micron) into the radial piston pump which is able to provide a hydraulic pressure level of 40-100 bar. Subsequently the flow passes a volumeflow-meter, another non-return valve avoiding a backflow into the fuel pumps, a junction, which is connected to the recirculation feed (where the recirculated fuel flow is regulated by a pressure balance) and an electromagnetic three-way valve. This valve is used to connect the further part of the circuit with its integrated nitrogen supply in order to flush the tubes in case of changing between fuel types.

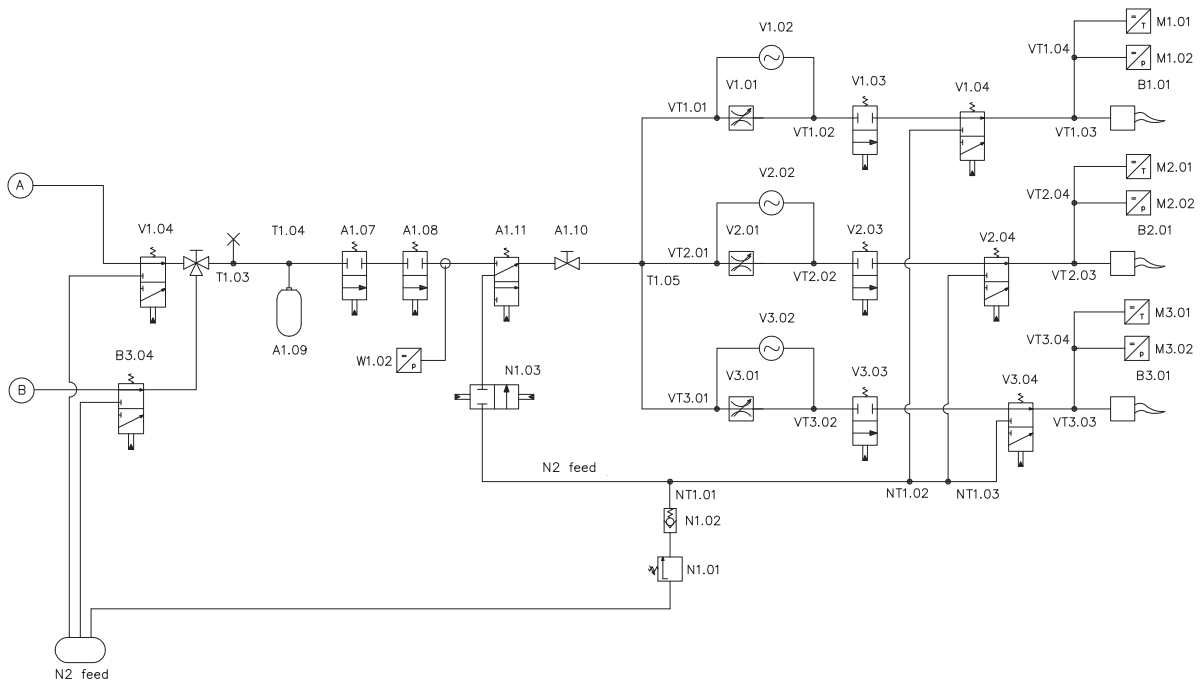


Figure 6.5: Schematic of the fuel supply (laboratory side)

As it can be seen in Figure 6.5, the nitrogen flush can be performed directly before the 3-way valve at T1.03 for the entire system, as well as for the laboratory sector only at V1.04 and A1.11. After the nitrogen 3-way valve a further valve switches between the fuel types. The latter part of the circuit (Figure 6.5 on the right-hand side) consists of 3 combined Coriolis mass flow meters / regulators, lock valves and temperature and pressure measurement devices. The pressure is measured using a piezoresistive sensor and the temperature using a Pt-100 resistance temperature sensor.

The replacement fuel feed is mostly build up comparably, the only difference to mention is that there is no feed orifice to the kerosene reservoir. It is connected directly to a barrel. The standard operating fuel-supply capacity of this unit is denoted with 10 g/s fuel. For this contribution only the kerosene feed has been in use. The required pumps still have to be installed for the alternative fuel circuit. For the Alfa Bird investigations the kerosene surge tanks have been filled with the investigated medium and the tubes flushed with nitrogen in each case.

Generally the fuel supply feed can be divided into 3 parts namely:

1. The fuel tank repository originally for kerosene and light fuel oil feeding the aforementioned air heater

2. The fuel depot room with surge tanks for kerosene and alternative fuels and the corresponding aggregation
3. The laboratory sided instrumentation

### 6.2.1.1 Fuel tank repository

Figure 6.4 on the top shows the symbolic for the fuel oil and kerosene tanks which are installed outside of the institute building. The fuel supply for the thermal air heater which is also installed outside and the kerosene supply are fed by these tanks using fuel pumps. The fuel oil cycle is not connected to the combustion laboratory supply.

The control of these fuel pumps for the kerosene and alternative fuel supply is performed by the control box of the supply feed in the surveillance room. This unit uses fuel level sensors in the surge tanks detecting the minimum and maximum fuel level. If the amount in the surge tank reaches its minimum the pumps are switched on and switched off when reaching the maximum.

### 6.2.1.2 The fuel depot room

The installations in the fuel depot room consist of the required aggregates (pumps, valves etc.) as well as the surge tanks with the aforementioned fuel level sensors and the surge tanks for kerosene and alternative fuels. The amount of liquid flow is detected by a volume flow meter. The data acquisition and control of the pumps is performed by the control box. As control parameters the amplification factor, the dead zone of the actuator as well as the upper and lower threshold for the impulse response can be set in order to optimize the regulating manner depending on the system pressure and required mass flow. These parameters have to be set empirically trying to avoid oscillations in the tubes, which the Coriolis mass flow meters and regulators are very sensitive for.

### 6.2.1.3 Laboratory-sided instrumentation:

The laboratory sided instrumentation is basically represented by the components shown in Figure 6.5, which will be detailed in the list below.

### 6.2.1.4 List of components

#### *Low pressure part:*

- **A/B1.01:**  
Manual blocking valve which separates the high pressure section from the rest of the system.
- **A/B1.02:**  
surge tanks for both circuits (volume 40 liter).
- **A/B1.03 and A/B1.04:**  
electromagnetic safety valves coupled with the laboratory fire system. In case of emergency they block the tanks from the system.
- **A/B1.05:**  
Non-return valve to avoid a backflow of the fuel into the surge tank
- **A/B1.12:**  
Inline Fuel filter (size 7 micron).

- **PVD:**  
Low-pressure pump; Beinlich ZPD 1-5,1-KIN-L-VMAG(60)/VV (maximum volume flow: 1-4 liters/min Kerosene at 3 bar difference pressure)
- **W1.03:**  
Piezoresistive pressure sensor for the surveillance of the low pressure pump (max. 5 bar)
- **PHD:**  
High pressure pump; Beinlich high pressure radial piston type pump TRGD 10/8-6,4-100/F/R/VMAG(75)/FFKM (Maximum volume flow 0,8-4 lit/min Kerosene at 100 bar difference pressure)

### ***High pressure part:***

- **VSZ:**  
Volume flow meter; (VSE 0,1 EP012V 32Q11/4-Ex)
- **A1.06/B1.13:**  
non return valve to avoid a back flow through the fuel pump against its flow direction.
- **W1.01:**  
temperature-sensor.
- **A1.07 and A1.08:**  
electromagnetic safety valves coupled with the laboratory fire system. In case of emergency they block the sector of the supply in the laboratory from the rest of the system.
- **A1.11:**  
3/2 Way safety valve in order to flush the tubes with nitrogen in case of emergency.
- **A1.10:**  
manual block valve to separate the sector of the supply in the laboratory from the rest of the system.
- **Bypass:**  
The pumps can realize quite high volume flows, hence they are over dimensioned in usual cases and pump too much fuel which has to be leaded back over the bypass
- **NT1.03:**  
Connection of the internal bypass of the low pressure pump and the reverse flow of the high pressure pump
- **A/B2.01:**  
manual pressure regulator for the high pressure circuit which can be set from 10-100 bar depending on the used spring for the spring valve.
- **A/B2.02:**  
Non return valve.
- **V1/2/3.03:**  
2/2 Way-Valve for blocking of non-needed fuel circuits during the tests.
- **V1/2/3.04:**  
3/2 Way-Valve for flushing purposes with nitrogen in order to avoid coking of the injection modules after the tests
- **V1/2/3.01:**  
Coriolis flow meter/regulator, Three singular modules are installed in order to run different injection modules simultaneously
- **M1/2/3.01:**

Sensor for the temperature before the injection module

- **M1/2/3.02:**  
Pick-up for the pressure before the injection module.

### 6.3 Combustor design

The main objective of this project concerning our field of responsibility is to obtain qualitative results for the comparison of the evaporation mechanism of several fuel-types. As a consequence it was decided to use an already existing burner-geometry for these investigations. The TIMECOP-AE injection system by TURBOMECA and the MERCATO (Moyen Expérimental de Recherche en Combustion Aérobie par Techniques Optiques) flame tube geometry at ONERA Fauga Mauzac have been chosen to be the best compromise. The burner design is based on a radial swirler with a hollow cone pressure fuel nozzle. Figure 6.6 presents the injection system. The air has a swirl motion with a rate of approximately 0.75. The swirl motion facilitates the liquid atomization, and the system creates a hollow cone spray with a recirculation zone inside the spray. Another effect of the swirl motion is to deposit droplets on the internal wall of the injection system with the formation of a liquid film on the wall. Thus, some droplets of the spray come from the disintegration of the film rather than from the atomization of the liquid jet emanating from the injector nozzle.

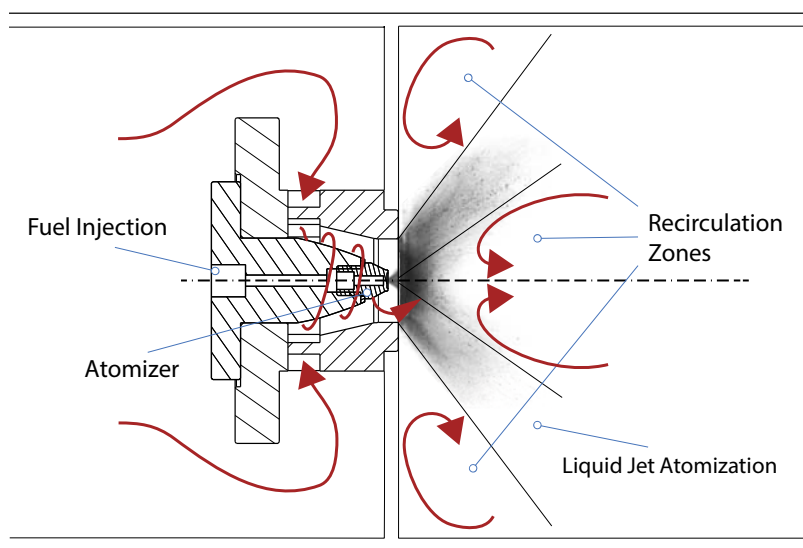


Figure 6.6: TIMECOP burner principle

However in comparison to the Mercato setup some modifications of the flame tube have been performed, such as the change of the rectangular design of the air box to a cylindrical one for manufacturing reasons and the installation of a heat strain resistive axial compensator, also the Delavan pressure atomizer has been replaced by an equivalent from Parker to fit an AMD (Area Mean Diameter) higher  $20\ \mu\text{m}$ . The flame tube has been integrated into the existing pressure casing of the test bench, allowing very quick changing intervalls in case of the necessity of simultaneous investigations in the laboratory. This has been acquired by using an adapter-flange construction to be plugged into the pressure casing. The pressure vessel (Figure 6.9) has a nominal diameter of  $\text{DN} = 300\ \text{mm}$  and a material strength of 10mm to withstand pressures up to 10 bar at elevated temperatures (up to 750 K). The optical access of the existing pressure vessel has been changed

due to the requirements concerning the measurement volume. The windows have been enlarged from a circular to a rectangular design in a dimension of 140 mm x 200 mm.

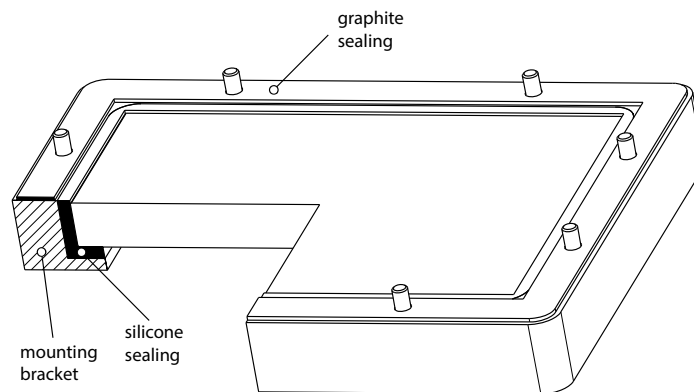


Figure 6.7: Optical access for the pressure vessel

The window panes are made of quartz-glass which is highly pressure and temperature resistive and has a wide range of light transmission according to the interesting wavelengths of 633nm and 3,39 $\mu$ m used for the Infrared Extinction measurement method. The sealing of the windows is made of silicone which is pasted into the mounting bracket and remains elastically. The bracket is mounted on the vessel using an area sealing made of graphite which is highly temperature resistant. The liner of the combustion chamber is rectangularly shaped and made of 2 mm metal sheet bolted to the flange of the air-box (Figure 6.9). It has four perpendicular windows which allow a centered optical access of 180 mm x 100 mm on each side flush with the entrance plane.

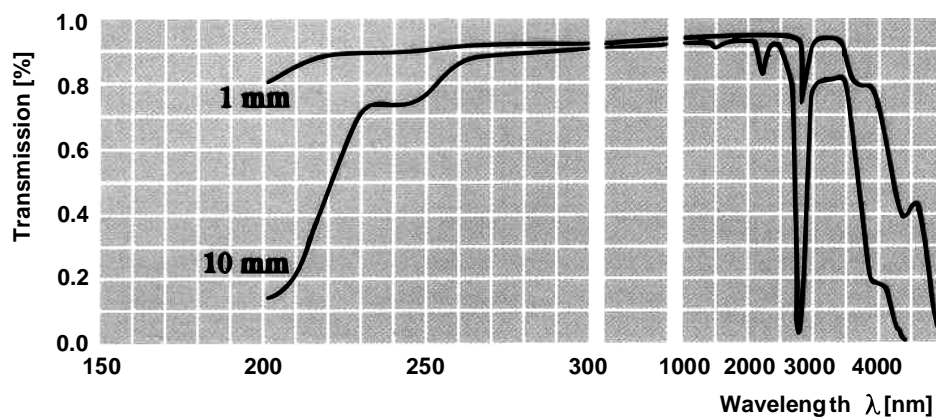


Figure 6.8: Transmission spectrum of quartz glass (Silux SQ1) used for window panes for 1 mm and 10 mm layer thickness [68]

The test specimen is applied with 4 piezoresistive absolute pressure sensors detecting the rotational symmetric mean-value of the pressure and 15 thermocouples (type K) on the interesting positions.

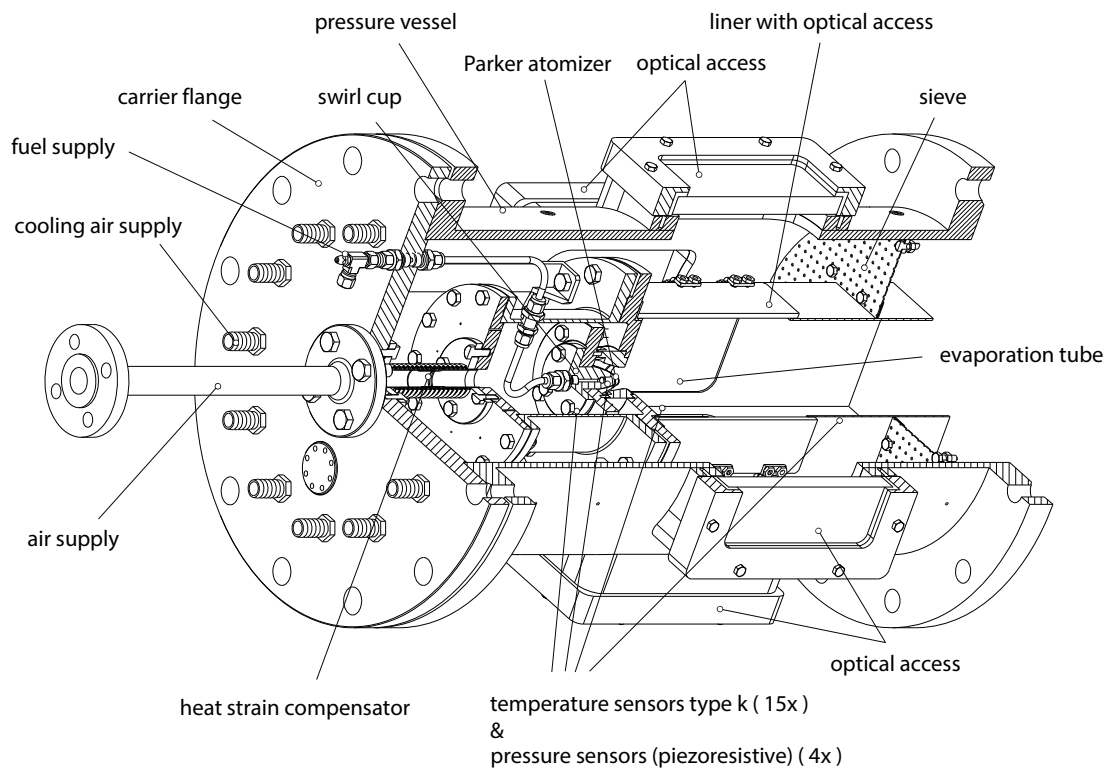


Figure 6.9: Cross-section of the pressure vessel including the Alfa Bird injection system

Since the limiting factor using the IRE method is represented by the minimum Area Mean Diameter  $D_{20} = 20 \mu\text{m}$ , it was necessary to find pressure atomizers which fit into this boundary conditions for each different operation point. The final decision was directed towards Macro-spray Single-Point Nozzles offered by Parker.

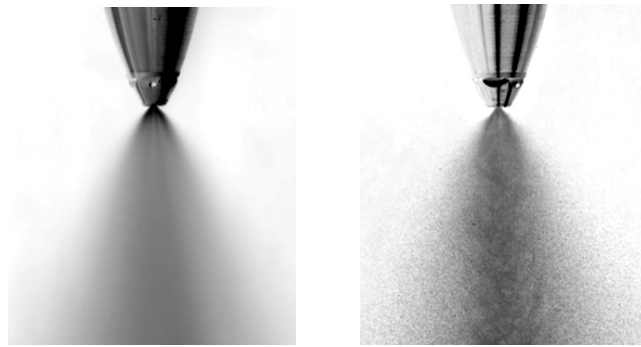


Figure 6.10: Parker Macro-spray nozzle injecting ethanol at 10 bar injection pressure (2 different exposure times)

These type of nozzles are designed to replace pressure swirl-type and impact nozzles and offer smaller droplets and repeatable droplet dispersion patterns at lower pressures than conventional nozzles. The formation of the spray cone is realized by a lamination technology where numerous layers are joined to create a macro lamination stack. For this technology sustainable filtering of the supplied liquids is essential because these type of nozzles cannot be cleaned in an ultrasonic bath. Therefore a 15 and a 7 micron filter have been installed in the fuel supply of the laboratory.

The different fuel mass flow rates which were predetermined by the selected operating conditions (Table 6.1) for the evaporation tests at TU-Graz, resulted in a choice of specific pressure nozzles for each test case.

Table 6.1: Operating conditions TU-Graz

	$p$ [Pa]	$T$ [K]	$V_{ref}$ [m/s]	$\dot{m}_{air}$ [g/s]	$\dot{m}_{kero}$ [g/s]	$\phi$
<b>Tests TU Graz LP</b>	1,00E+05	750	33,36	10,95	0,76	1
<b>Tests TU Graz HP</b>	3,00E+05	750	33,36	32,86	2,27	1
<b>Tests TU Graz VHP</b>	5,00E+05	750	33,36	54,77	3,78	1

Figure 6.11 shows the mean particle diameter distribution (Sauter Mean Diameter SMD) at 50 mm downstream of the injector nozzle depending on the differential pressure of the fuel supply and the test chamber. Using this diagram led to choose nozzles which operate at differential pressure levels of 5 bar and below to still fulfill the threshold of 20  $\mu\text{m}$  for the Area Mean Diameter (D20) (which is even lower than the SMD) for the required fuel mass flow rates.

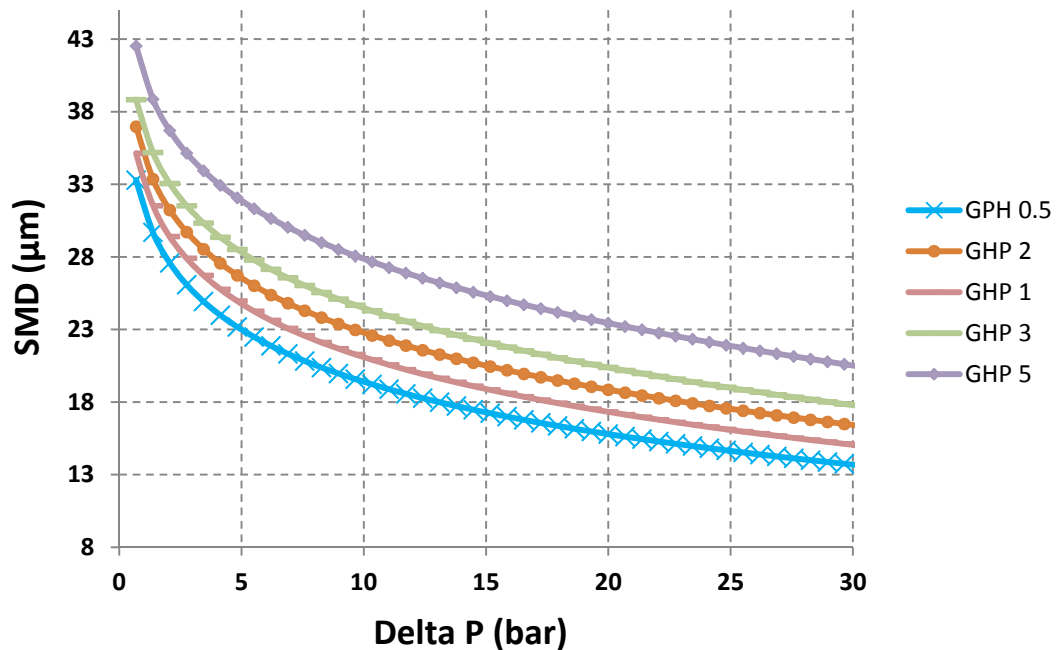


Figure 6.11: Pressure evolution of SMD for different flow numbers

Based on the data sheet of the nozzle supplier, the mass flow rates for different flow numbers of the nozzles varying the pressure levels have been calculated (Table 6.2). The choice was directed to the lowest pressure level at which the required fuel mass flow rates still can be delivered, this resulted in nozzles with flow numbers (GPH - Gallons Per Hour) 1, 2.5 and 5 for TU-Graz and 1.5, 3 and 5 for ONERA.

Table 6.2: Mass flow rates for Jet A1 of macro spray nozzles for different pressure levels

Nozzle Flownumber	Pressure [psi]/ [bar]						
	100	200	300	400	500	750	1000
	6,89	13,79	20,68	27,58	34,47	51,71	68,95
GPH	Massflow [g/s]						
0,5	0,42	0,588	0,756	0,84	0,924	1,176	1,344
1	0,84	1,176	1,428	1,68	1,848	2,268	2,688
1,5	1,26	1,764	2,184	2,52	2,856	3,444	3,948
2	1,68	2,352	2,94	3,36	3,78	4,536	5,292
2,5	2,1	2,94	3,612	4,2	4,704	5,796	6,636
3	2,52	3,528	4,368	5,04	5,628	6,888	7,98
5	4,2	5,964	7,308	8,4	9,408	11,508	13,272

## 6.4 Afterburner design

In the dilution zone an afterburner had to be installed in order to reduce the unburnt hydrocarbons by a controlled pyrolysis, which was necessary according to the Alfa-Bird-related isothermal vaporisation investigations without combustion. Figure 6.12 shows the concept of the test cell and the afterburner.

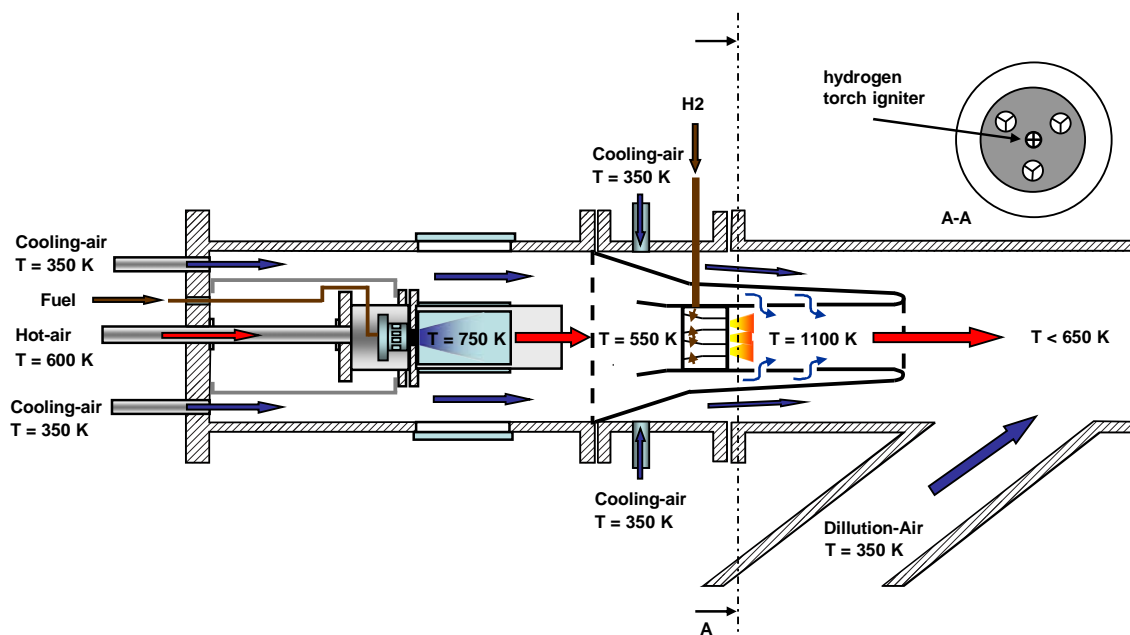


Figure 6.12: schematic overview of the test section

The hot compressed air is guided through the main-tube into the airbox and cooling air is passing alongside the flame tube. Passing the radial swirler, the hot flow is mixed with the investigated fuel using an equivalence ratio of  $\Phi = 1$ . After the liner, the hot fuel / air mixture is diluted by the cooling air. In order to avoid flashback the blend is attenuated till  $\Phi = 0,5$ . The suchlike conditioned flow is introduced into the after burner.

In order to generate a controlled pyrolysis the whole mixture has to be heated up to at least 1100 K [71]. The required thermal power of the burner has been calculated to be approximately 120 kW. To reach this thermal power it is planned to use a circular arrangement of three axial swirl combustors, which have been developed by Lang [77] at the Combustion Department of the institute of thermal turbo machinery and machine dynamics. The functionality and the stability of the existing geometry is well known and the burner stability has been proven.

The burners are operated with methane provided by the internal gas circuit of the laboratory, the operation point is regulated with a pressure reducer and a V-cone flow meter. The mixture is ignited with a lighting-up lance. An online camera system from Panasonic directed to an optical access into the inside of the liner serves for flame surveillance. The exhaust gases coming out of the burner-conglomerate have to be highly diluted because of the uppermost allowed temperature level in the exhaust tower of max. 670 K. For this purpose, compressed dilution air is led into the exhaust tube coming from a side junction.

## 6.5 Thermodynamic dimensioning of the afterburner concept

In this chapter the method of the dimensioning and principle design aspects are explained and detailed. As a predefined base for the final design of the flame tube-afterburner conglomerate the different positions in the Alfa Bird test matrix have been assumed as essential boundary conditions for the entire system including the tube system in the combustion laboratory (Table 6.1). The system is separated into four zones of interest which are treated separately, namely evaporation tube zone, mixing zone, flame tube zone and dilution zone. The thermodynamic calculation and the geometric dimensioning have been performed in Microsoft excel and are based on chemical values for air, water vapor and kerosene taken from the data base Gas Eq [72] and tables of thermodynamics [74].

### 6.5.1 Evaporation tube zone

The basic calculation starts with the system evaporation tube (marked red in Figure 6.13). Taking the predefined boundary conditions (Table 6.1) into account, an energy balance of incoming and outgoing media was performed in order to get the resulting enthalpy flow. The Heat transfer on the walls of the flame tube has been neglected.

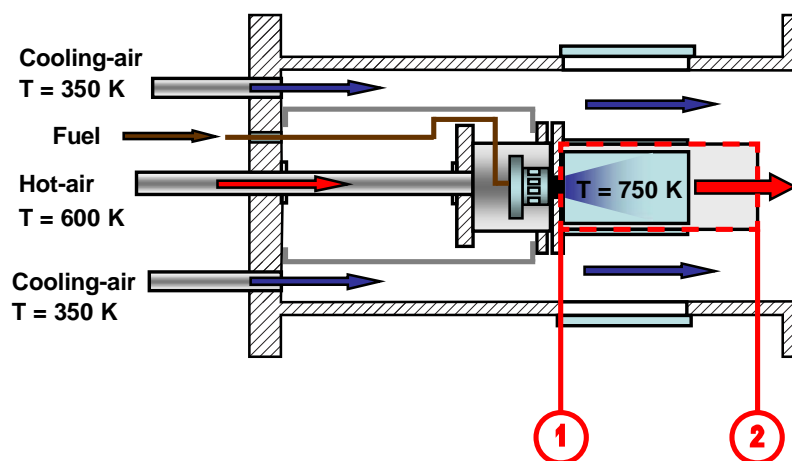


Figure 6.13: Evaporation tube zone

As a consequence of the induction of evaporated fuel its evaporation heat has to be included into the balance. The inducted hot air has to be slightly higher than the required 750 K in order to maintain the temperature level. Equation ( 6.1 ) can be derived from the first law of thermodynamics for open systems and represents the enthalpy balance of the discussed system.

$$Q_a + W = \sum(H_o) - \sum H_{in} + E_{a o} - E_{a in} \quad (6.1)$$

$Q_a$  stands for heat transfer,  $W$  for technical work,  $H$  represents the incoming and outgoing enthalpy and  $E_a$  is the the system immanent energy namely either kinetic or potential energy. While Index 'in' stands for incoming and index 'o' for outgoing.

$$\dot{m}_L h_L + \dot{m}_{kerosene} (h_{kerosene} - r_x) = \dot{m}_{mix} h_{mix}$$

$$\dot{m}_{mix} = \dot{m}_L + \dot{m}_{kerosene} \quad (6.2)$$

$$H_{mix} = \dot{m}_L h_L + \dot{m}_{kerosene} (h_{kerosene} - r) \quad (6.3)$$

The system is assumed being adiabatic and the system immanent energy can be neglected. As a consequence equation ( 6.1 ) can be simplified to equation ( 6.3 ).  $r$  stands for the latent heat of vaporization which is defined as the difference between the specific enthalpy of dry saturated vapor and the boiling fluid which are in equilibrium [69].

$$r(T) = h_{vap}(T, p_s(T)) - h_{liq}(T, p_s(T)) \quad (6.4)$$

The composition of the mixture changes due to the evaporation of the liquid which results in a dependency of the vapor pressure and the heat of vaporization from the actual composition in the liquid. Concerning kerosene, the gradient of latent heat vaporization can be assumed as being temperature dependent only. It is diminishing with increased temperature and vanishes at the critical point. Equation ( 6.5 ) represents an approximation for the specific latent heat of vaporization for kerosene Jet A1 by Watson which has shown pretty good accordance with the experiment [70].

$$r(T) = 333339,03 * (684,26 - T)^{0,38} \quad (6.5)$$

For the calculations the assumption of an ideal gas has been taken into account. Also the incoming energy of the introduced liquid kerosene has been neglected being of minor relevance opposed to the lower heat value of kerosene.

$$dh_{mix} = c_{p_{mix}} * dT \quad (6.6)$$

The heat capacity  $c_p$  of the fuel-air mixture is determined by the summation of its mass fractions  $\mu_i = m_i / m_{ges}$ . Values for kerosene have been replaced by iso octane due to availability reasons which has shown good approximation results.

$$c_{p_{Mix}} = \sum_{i=1}^n c_{p_i} * \mu_i = c_{p_{Air}} * \mu_{Air} + c_{p_{Kerosene}} * \mu_{Kerosene} \quad (6.7)$$

### 6.5.2 Mixing zone

The following zone of interest is the area where the cooling air for the liner and the pressure vessel which is directed between those is mixed with the hot fuel-air mixture coming out of the evaporation tube. For safety reasons the dilution in this zone has to be set to an equivalence ratio of at least  $\phi=0,5$ . Richer mixtures can easily cause flashbacks from the combustion zone in the afterburner to the measurement volume, which has to be avoided because of the optical access windows being sensitive to suchlike shock conditions.

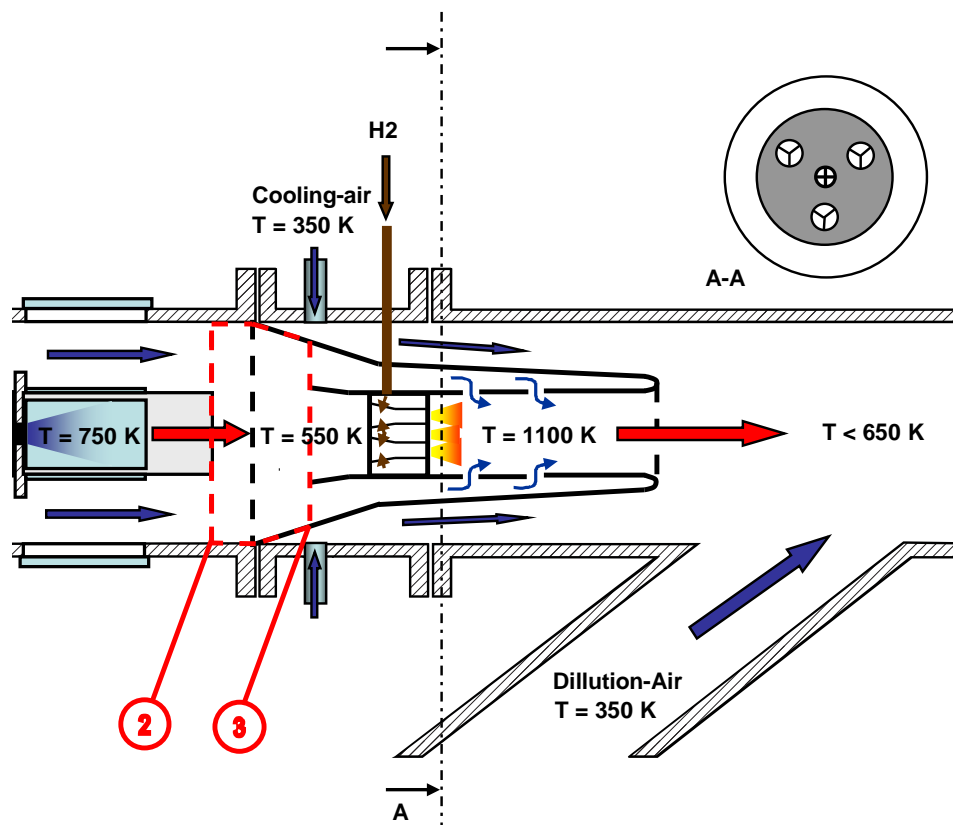


Figure 6.14: Mixing/Dilution Zone [2]

The needed air mass for these requirements can be calculated as follows:

$$L = \frac{L_{min}}{\phi} = \frac{m_{Air}}{m_B} \quad (6.8)$$

L is the amount of air and  $L_{min}$  is the minimum air demand for stoichiometry depending on the used fuel. It was approximated using  $C_{12}H_{23}$  equivalent for kerosene. The enthalpy balance for the mixing zone again is set up as before. Based on the demanded equivalence ratio the needed air

mass can be calculated: The mass flow exiting the evaporation tube zone which includes the mass of air needed for cooling  $\dot{m}_{cool}$  and entering the flame tube zone can be combined as  $\dot{m}_E$ .

$$\dot{m}_E = \dot{m}_{mix} + \dot{m}_{cool} \quad (6.9)$$

$$\dot{m}_{cool} * h_{cool} + \dot{m}_{mix} * h_{mix} = \dot{m}_E * h_E$$

$$\dot{m}_{cool} = \frac{\dot{m}_{mix} * (h_E - h_{mix})}{h_{Luft} - h_E} \quad (6.10)$$

### 6.5.3 Flame tube zone

After the evaporation tube the hot fuel-air mixture is diluted with the cooling air passing between pressure vessel and the specimen. Before being introduced into the afterburner the diluted mixture is separated into a primary and a secondary flow. The primary flow is directed straight through 3 axial swirl combustors (Figure 6.15) in order to assure a stable combustion in the chamber at stoichiometric conditions.

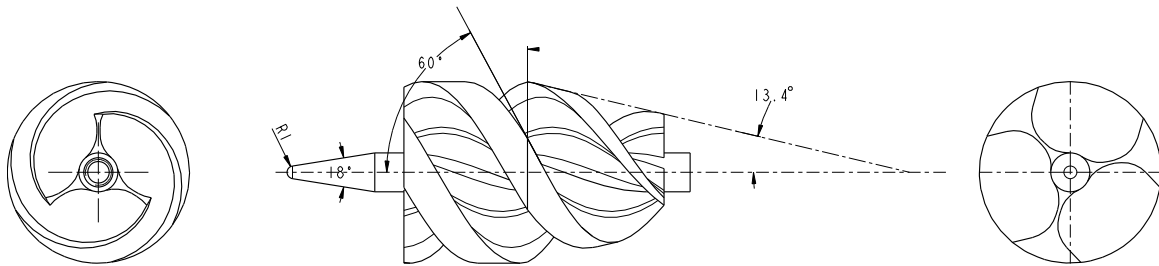


Figure 6.15: Axial swirl geometry

The secondary flow is induced into the liner from which it enters the combustion chamber across boreholes and acts as cooling flow. The hydrocarbon residues in the flow are oxidized due to the high temperatures of the exhaust flow [71]. The position of the boreholes and their distribution is based on empirical values. In order to produce a stoichiometric mixture, methane is added over tubes before the flow is entering the swirlers in the zones of flow acceleration to guarantee that the gas is not pushed back.

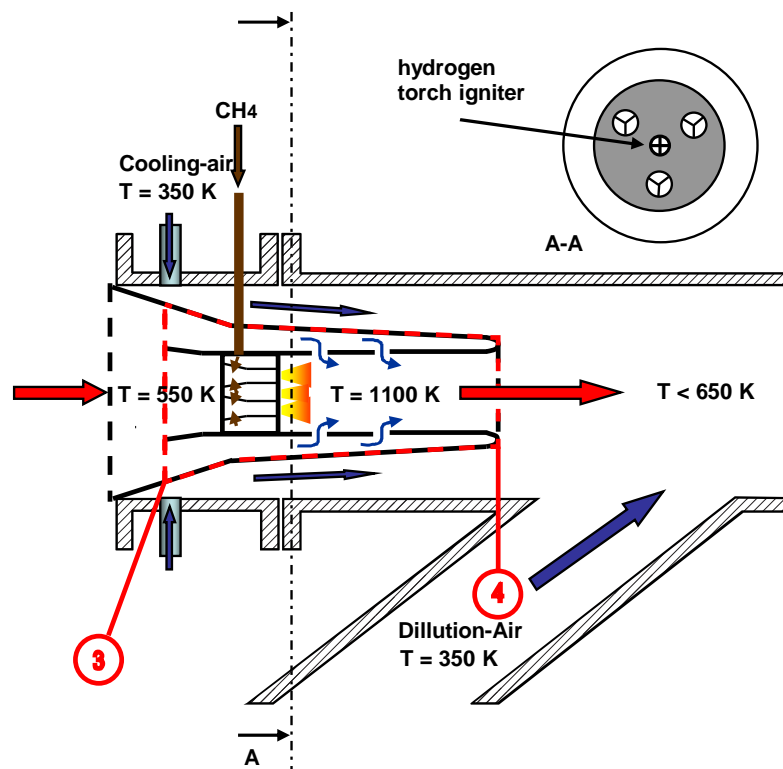


Figure 6.16: Flame Tube zone

As it is shown in Figure 6.16 the required temperature for a safe pyrolysis in the exhaust area shall be around 1100 K.

The dimensioning of the combustion chamber in the flame tube zone is based on the lecture series from Suttrop [75]. This method uses the cycle process in gas turbines (Figure 6.17) which is defined by the outlet conditions of compressed air coming out of the combustor and the maximum temperature for the stator rows. In our case the necessary temperature for a controlled pyrolysis and the pressure levels of the test matrix are the base of the boundary conditions.

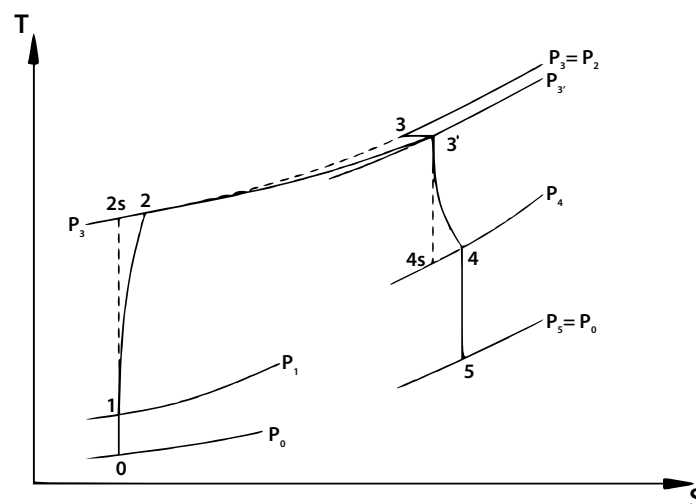


Figure 6.17: Real Brayton-Cycle

The assumptions for compression and expansion and its mechanic efficiencies can here be neglected due to focusing on conditions  $(p_2, T_2)$  to  $(p_3, T_3)$  and having the inlet and outlet mass flows predefined. The main aspects taking into consideration have to be the combustion efficiency. It defines the completion of the combustion and is proportional to the exhaust emissions of carbon monoxide and unburned hydrocarbons. Usually the combustion efficiency in gas turbines lies around 80 – 100% depending on the design type of the combustion chambers. Nowadays regulation departments demand for the efficiency being higher 99 %.

The combustion efficiency is influenced by several factors especially:

- Atomization and Vaporization
- Turbulent mixing of the fuel with air and exhaust emissions
- Chemical reaction
- Heat transfer by convection and radiation

Generally it is assumed that it is a function of time in which the induced fuel is burned. This time is dependent on the amount of time it takes for the evaporation, mixing and its chemical reaction. As a consequence there are several actions influencing the process. Usually one of these actions dominates the combustion process, hence the following methods for the calculation of the efficiency can be used:

- Reaction controlled systems (heat release is based on chemical reaction)
- Mixing controlled systems (Evaporation and mixing are assumed being immediate)
- Evaporation controlled systems (mixing and chemical reaction are assumed being immediate)
- Reaction and evaporation controlled systems (heat release depends on evaporation and chemical reaction)

Due to our system running by methane and being premixed and pre-vaporized, the reaction controlled system is the most suitable system.

The definition of the combustion efficiency in suchlike systems is defined as [76]:

$$\eta_A = \frac{\text{heat release due to combustion}}{\text{Induced chemical combustion energy}} \quad (6.11)$$

For a quick dimensioning of combustion chambers usually two methods are being applied based on empirical values namely:

- Theory of burning velocity
- Theory of homogeneous reactors

### 6.5.3.1 Theory of the burning velocity

This theory includes the following assumptions:

1. The fuel is completely mixed before entering the combustion chamber
2. The evaporation time is infinitely short

3. Once ignited the fuel is burning out completely

An energy balance under these assumptions for  $\eta_A = 1$  results in:

$$\dot{m}_{br} H_u = \dot{m} c_p \Delta T \quad (6.12)$$

And for  $\eta_A < 1$

$$\dot{m}_{br,v} H_u = \dot{m}' c_p \Delta T \quad (6.13)$$

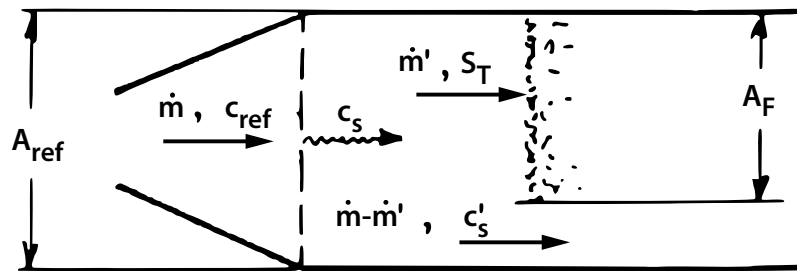


Figure 6.18: Flame front propagation in a combustion chamber [75]

The amount of chemical combustion energy is according to the heat release for both cases. For the combustion efficiency can be written:

$$\eta_A = \frac{\dot{m}_{br,v} H_u}{\dot{m}_{br} H_u} = \frac{\dot{m}' c_p \Delta T}{\dot{m} c_p \Delta T} = \frac{\dot{m}'}{\dot{m}} \quad (6.14)$$

Referring to [75] and based on the law for conservation of mass it can be formulated for  $\dot{m} = \rho A_F S_T$  and  $\dot{m} = \rho A_{ref} c_{ref}$  further calculations and empirical determinations have shown that an approximate definition for the final combustion efficiency results in:

$$\eta_A = f \left[ \frac{p_2^{1,75} A_{ref} d_{ref}^{0,75} e^{\frac{T_2}{300}} H_u}{\dot{m}} \right] \quad (6.15)$$

This definition includes the most important factors for the determination of the combustion efficiency namely operating conditions ( $p_2, T_2$  and  $\dot{m}$ ) and geometry ( $A_{ref}$  and  $d_{ref}$ ) [76].

### 6.5.3.2 The homogeneous reactor

This model assumes that turbulence, mixing and turbulent flame front generation in the combustion chamber are happening at the same time.

The mixing is supposed to happen infinitely fast which results in a good turbulence and mixture, hence it can be defined as homogeneous reactor. An important factor for the devolution of chemical reactions is the reaction time  $t_R$ :

$$t_R = e^{\frac{E}{RT}} \frac{\left(\frac{T}{p}\right)^\nu}{\psi_{br}^\mu - \psi_{O_2}^{\nu-\mu}} \quad (6.16)$$

While the reaction is taking place within the time  $t_R$  the amount of fuel  $\dot{m}_{br,v}$  is burned. The available residency time derives from the mass flow:

$$t = \frac{m}{\dot{m}} = \frac{V \rho}{\dot{m}} = \frac{V p}{\dot{m} R T} \approx \frac{V p}{\dot{m}_{Air} R T} \quad (6.17)$$

In case of a combustion in the homogeneous reactor the residency time has to be of the same amount as the reaction time  $t = t_R$ .

Equalizing ( 6.16 ) and ( 6.17 ) results in a definition of the combustion efficiency [76]:

$$\eta_A = f \left[ \lambda, \frac{V p_2^{1,75} e^{\frac{T_2}{300}}}{\dot{m}_{Air}} \right] \quad (6.18)$$

### 6.5.3.3 Energy balance for the flame tube zone

For the energy balance of this zone a combustion efficiency of  $\eta_A = 1$  has been assumed.

Stoichiometry ( $\phi = 1$ ) in the combustion chamber is difficult to be assured due to the recirculation zones in the chamber which lead back part of the unburned fuel mixed with air coming from the liner boreholes. Stable operation conditions can therefore only be approximated, hence have to be determined experimentally.

A deviation from the stoichiometric conditions can have several advantages and disadvantages dependent on the actual equivalence ratio  $\phi$  which are summarized in Table 6.3.

Table 6.3: Main aspects of the equivalence ratio in the primary zone of combustion chambers [76]

Equivalence ratio	advantages	disadvantages
$\phi < 1$ lean	<ul style="list-style-type: none"> <li>• Clear flame, no smoke</li> <li>• Low flame temperature</li> <li>• Good temperature distribution in the outlet</li> </ul>	<ul style="list-style-type: none"> <li>• Low recirculation velocity → good ignition and stability</li> </ul>
$\phi = 1$ stoichiometric	<ul style="list-style-type: none"> <li>• Good efficiency</li> <li>• Clean combustion, no smoke</li> </ul>	<ul style="list-style-type: none"> <li>• High flame temperature → increased heat transfer on the liner walls</li> <li>• High amount of NOx</li> </ul>
$\phi < 1$ rich	<ul style="list-style-type: none"> <li>• Low recirculation velocity → good ignition and stability</li> </ul>	<ul style="list-style-type: none"> <li>• Flame indulgence</li> <li>• Inefficient combustion and smoke</li> </ul>

For the calculation of the approximated methane consumption for stoichiometry again an energy balance for the system 3-4 (see Figure 6.16) has been performed.

$$\dot{m}_E h_E + \dot{m}_{CH_4} H_{u_{CH_4}} = \dot{m}_{EG} h_{EG}$$

$$\dot{m}_E c_{pE}(T_3) T_3 + \dot{m}_{CH_4} H_{u_{CH_4}} = \dot{m}_{EG} c_{pEG}(T_4) T_4$$

$$\dot{m}_{CH_4} = \frac{\dot{m}_{EG} c_{pEG}(T_4) T_4 - \dot{m}_E c_{pE}(T_3) T_3}{H_{u_{CH_4}}} \quad (6.19)$$

Primarily for an approximation it can be assumed ideal gas boundary conditions and the introduction of methane mass as being of minor relevance. It can be assumed that nearly 50 percent of the secondary mass flow through the liner is participating in the combustion due to zones of recirculation (see Figure 6.19) [76].

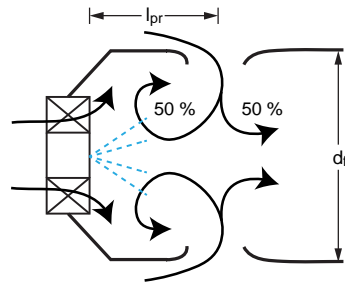


Figure 6.19: Separation of the secondary mass flow in the primary zone

A re-calculation taking the aforementioned simplifications and the recirculation of 50 % of the secondary flow into account leads to ( 6.20 ) for the required amount of methane in the primary zone.

$$\dot{m}_{CH_4} = \frac{(T'_4 - T_3) (\dot{m}_{primary} + 0,5 \dot{m}_{secondary}) c_{pAir}}{H_{u_{CH_4}}} \quad (6.20)$$

For the equivalence ratio it can be written:

$$L = \frac{L_{min}}{\Phi} = \frac{\dot{m}_{Air}}{\dot{m}_{CH_4}} \quad (6.21)$$

Additionally the temperature after the complete mixing with the secondary air can be simplified as:

$$T_4 \cong \frac{0,5 \dot{m}_{primary} c_p(T_3) T_3 + (\dot{m}_E - 0,5 \dot{m}_{primary}) c_p(T'_4) T'_4}{\dot{m}_E c_p(T_4)} \quad (6.22)$$

### 6.5.4 Dilution zone

The exhaust gases and the cooling air for the liner of the afterburner unit are induced into dilution zone which is the area where the cold bypass air from the compressor station (dilution air) is mixed with the hot exhaust gases from the combustion chamber. For this zone again an enthalpy balance has been performed in order to determine the required cold air mass from the bypass to guarantee that the uppermost temperature in the exhaust tower of approximately 650 K is not reached.

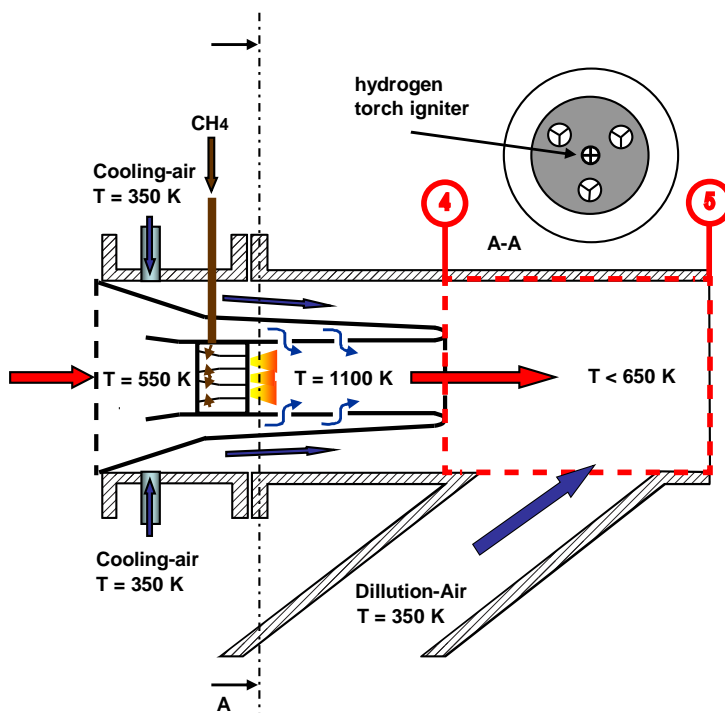


Figure 6.20: Dilution Zone

Energy balance of the system is presented in ( 6.23 ) (index EG stands for exhaust gases and dil for diluted):

$$\dot{m}_{EG_{dil}} = \dot{m}_{Air} + \dot{m}_{EG} \quad (6.23)$$

$$\dot{m}_{Air} = \frac{\dot{m}_{EG} * (h_{EG_{dil}} - h_{EG})}{h_{Air} - h_{EG_{dil}}} \quad (6.24)$$

$$\dot{m}_{Air} * h_{Air} + \dot{m}_{EG} * h_{EG} = \dot{m}_{EG_{dil}} * h_{EG_{dil}}$$

Including the definition for the specific heat capacity at constant pressure results in equation ( 6.25 )

$$\dot{m}_{Air} = \dot{m}_{EG} * \frac{T_{EG_{dil}} * cp_{EG_{dil}} - T_{EG} * cp_{EG}}{T_{Air} * cp_{Air} - T_{EG_{dil}} * cp_{EG_{dil}}} \quad (6.25)$$

### 6.5.5 Geometric dimensioning of the combustion chamber

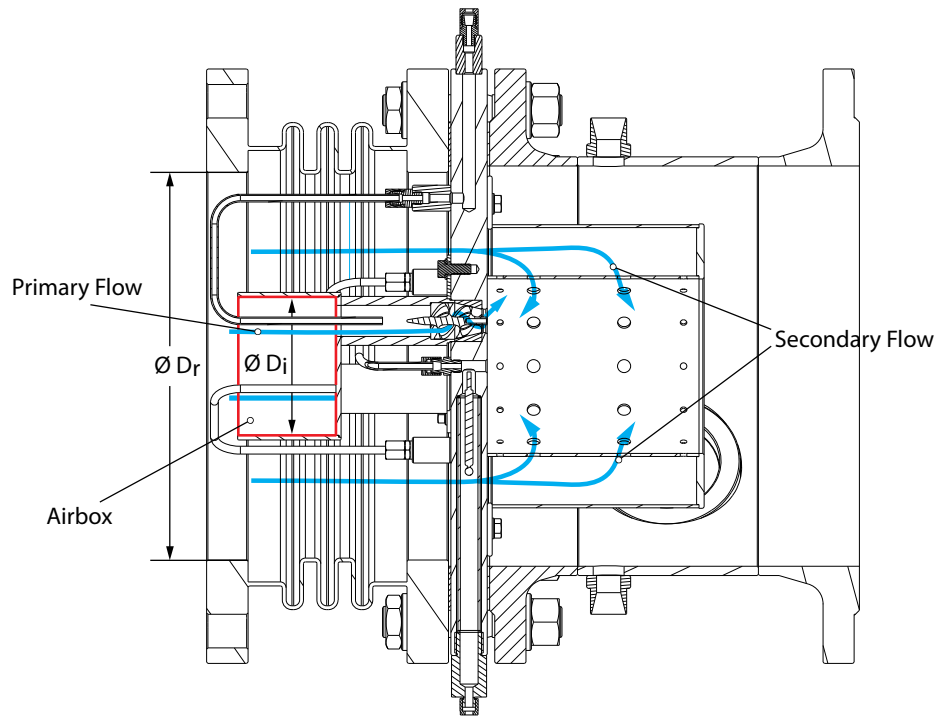


Figure 6.21: Cross section of the After Burner

The exiting mass flow is separated into primary and secondary flow by the airbox shown in Figure 6.21. The primary flow then is directed through the axial swirl generators. The velocity inside the swirler nozzles has to be kept under the maximum velocity of 7,2 m/s (Table 6.4), because otherwise stability of the combustion process cannot be assured.

The aspired equivalence ratio for the process lies at around  $\phi = 0,6 - 0,8$ . The assumption is a lean combustion of methane which is enriched by the hydrocarbon residues coming from the evaporation tube. Table 6.4 lists the geometric boundary conditions for the setup.

Table 6.4: Boundary conditions for geometric dimensioning

Inlet temperature	$T_{EG}$	556,9 [K]
Inlet diameter	$D_R$	0,30 [m]
Inlet face	$A_{Tube}$	0,07 [m <sup>2</sup> ]
Swirl generator diameter	$d_{Swirl}$	0,024 [m]
Swirl generator face	$A_{Swirl}$	0,00045 [m <sup>2</sup> ]
Volume flow	$V_{Tube}$	0,0352 [m <sup>3</sup> /s]
Mean Flow Velocity	$w_{Tube}$	0,498 [m/s]
Maximum velocity in the swirl generator	$w_{smax}$	7,2 [m/s]

A general simplification includes the assumption that the cooling air and the fuel air mixture from the evaporation process is completely mixed before being split up into primary and secondary flow and entering the afterburner.

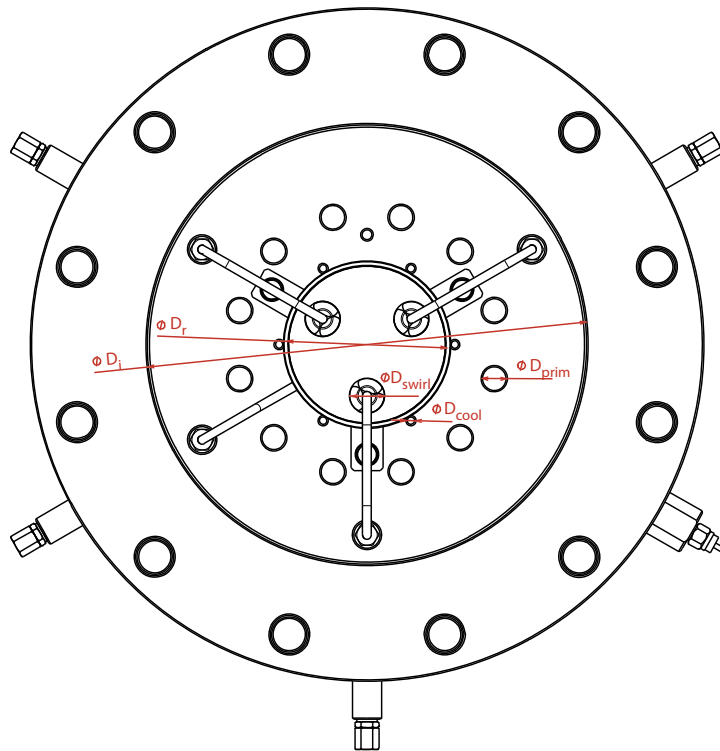


Figure 6.22: Front view (inlet) of the afterburner showing important diameters

For the geometric dimensioning firstly the listed boundary conditions had to be considered. Using three axial swirl generators with a fixed diameter and taking their maximum flow velocity for stable operation into account resulted in a diameter of 130 mm for the air-box. Based on this geometric ratio also the primary and secondary mass flow ratio have been approximated.

$$\frac{\dot{m}_{EG}}{\dot{m}_{Prim}} = \frac{A_{tube} - A_{Airbox}}{A_{Airbox}} \quad (6.26)$$

$$\frac{\frac{D_r^2 \pi}{4} - \frac{D_i^2 \pi}{4}}{12 * \frac{D_{Prim}^2 \pi}{4} + 6 * \frac{D_{cool}^2 \pi}{4}} = \frac{\frac{D_i^2 \pi}{4}}{3 * \frac{D_{swirl}^2 \pi}{4}} \quad (6.27)$$

The ratio of the inlet face of the airbox and the swirler faces for the primary flow is of the same extent as the ratio of the tube face and the boreholes for the secondary flow (see Figure 6.23 ). The secondary flow has been split into the flow passing the liner and cooling boreholes in a face ratio of 95% to 5%.

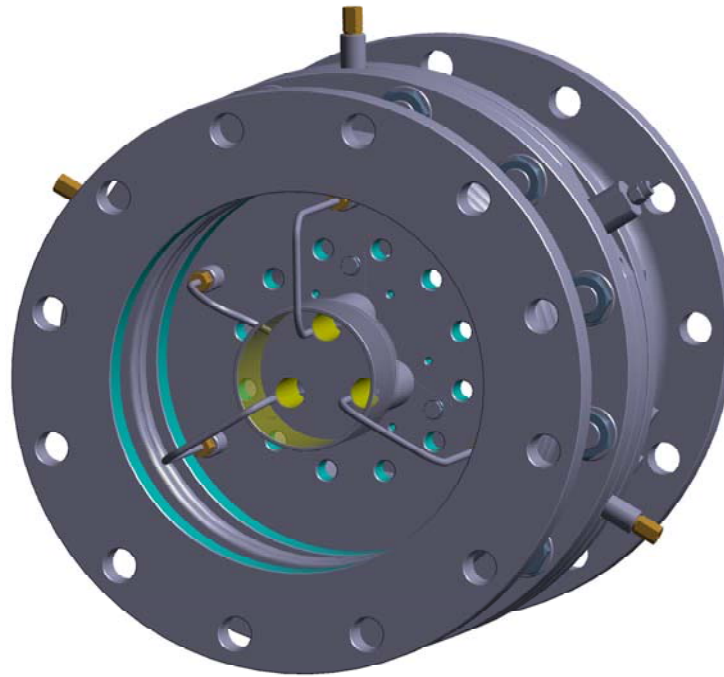


Figure 6.23: Inlet faces for the primary (yellow) and secondary (blue) mass flow

The sum of the faces for the secondary flow into the liner serve as initial size for the dimensioning of the boreholes for the primary and secondary boreholes in the liner.

Principally the distribution in the liner is divided into 4 rows of 12 radial-symmetrically positioned holes each. 2 rows for cooling, one for introducing the primary zone of the flame tube and one for the dilution zone (see Figure 6.24).

The distribution of the mass flow through the different boreholes is listed in Table 6.5.

Table 6.5: Distribution of the mass flow entering the line

	1 <sup>st</sup> cooling row	Primary holes	Mixing holes	2 <sup>nd</sup> cooling row
Distribution of secondary flow	10%	40%	40%	10%

The length of the primary zone has been set to  $L_{\text{prim}} = 0.5 D_L$  using the diameter of the liner  $D_L$ , based on empirical values taken from [76]. The optimal distance of the primary holes from the inlet face was determined experimentally by observing the cooling zone and trying to avoid zones of increased glowing inside the liner. For this purpose several liners using different geometries have been constructed and tested. The liner presented in Figure 6.24 and Figure 6.25 is the initial version, the cooling holes are positioned close to the head plate and the positions of the primary holes have been varied stepwise in downstream direction. The optimal position for these boreholes has been found after several tests to be lying at 58 mm distance from the head plate.

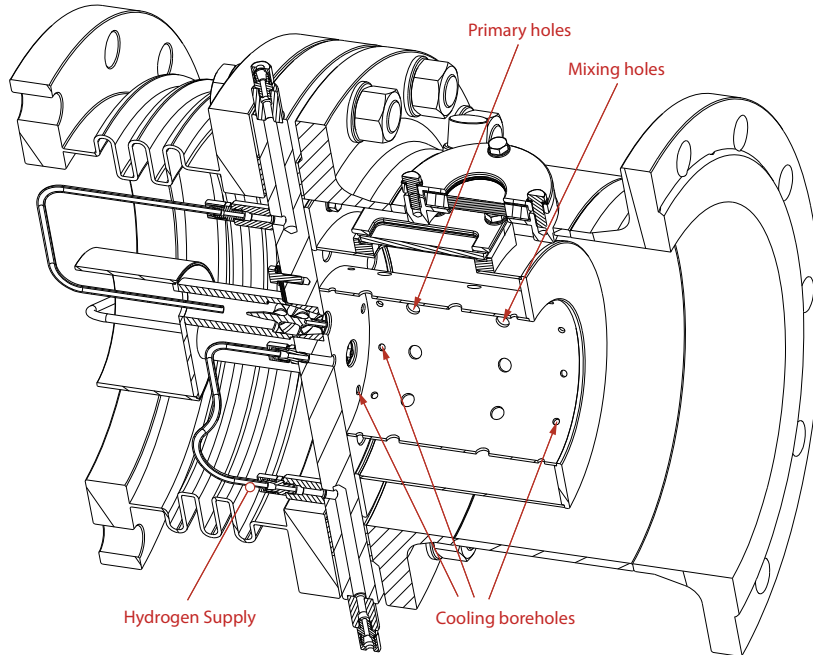


Figure 6.24: Definition of the bores for the primary and secondary zone of the flame tube

### 6.5.6 Optical access and ignition

Figure 6.25 shows the cross section of the various parts in the combustion chamber, starting from left to right including the air box and the fuel supply injecting methane to the swirler inlet. An optical access had to be included due to the required flame surveillance which has been performed using an online camera system from Panasonic directed into the afterburner passing quartz windows. This camera system is connected to the control room of the laboratory where it is monitored.

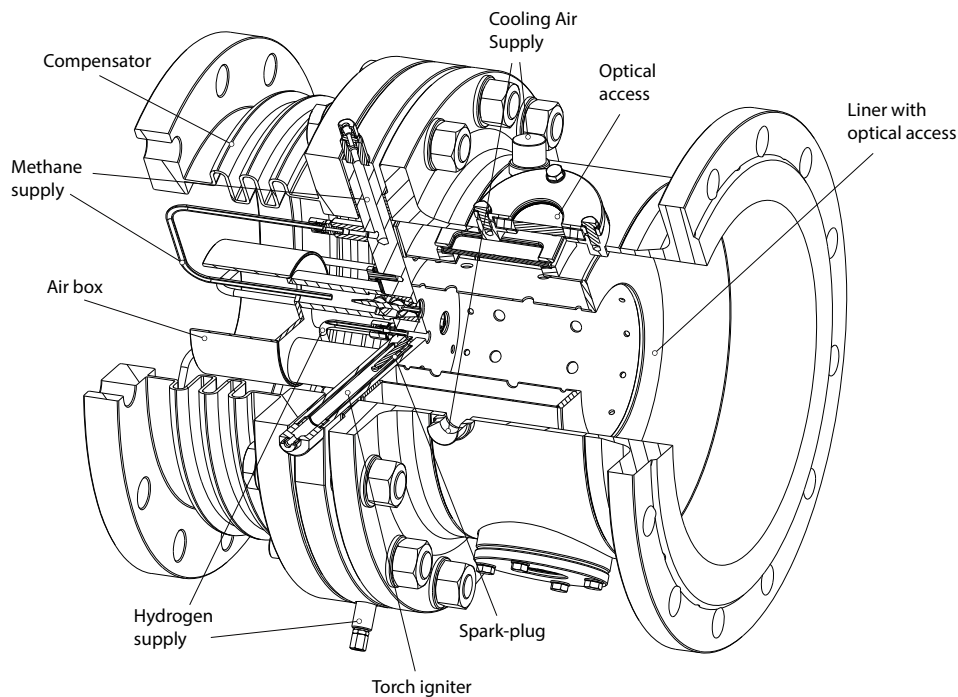


Figure 6.25: Cross section of the main components in the afterburner unit

Two optical access windows on the pressure vessel and two according windows on the liner have been installed. The principle for the outer window fixation is analogous to the evaporation chamber windows, the only difference is that they are circular and not rectangular. On the inside the windows are clipped and sealed with graphite sealing material. The positioning of the windows has been realized in an inclination which allows to direct the visual path of the detecting device through the pressure vessel and the flame tube without interfering with the flow conditions in the inside of the chamber. The system detects the flame illumination reflected through the primary holes. In case of flame blow out, the fuel supply is stopped and flushed with nitrogen for safety reasons.

Because of optical access windows being sensitive to regular detonation ignition devices, which are typically used for these types of combustion chambers, another system had to be used. An appropriate alternative was found in a continuous torch igniter which had been developed by Audrey Camps [73]. Instead of methane, hydrogen was used because of its advantageous properties of having broader ignition boundaries, which was necessary due to ignition problems during evaporation tests using methane under pressure.

The principle of the setup can be seen in Figure 6.25. The spark plug is fixed orthogonally in the flange of the combustion chamber and can be changed easily from the outside. The fuel supply injects hydrogen in flow direction in the center of the three axial swirl generators. The ignition device uses the fuel supply tube wall as ground for the ignition. In order to avoid a short circuit before the spark plug, the entire bore for the plug has been embedded in a ceramic isolation being highly heat resistive.

The schematic of the ignition system is shown in Figure 6.26. The hydrogen supply is directed over a three way valve also connected to the nitrogen supply. Both circuits are opened and closed using solenoid valves. They are actuated by a Möller Easy 412-DC-DR control relay. Nitrogen is used as purge gas for safety reasons. If the ignition is not successful after a few seconds, the com-

bustor is flushed with nitrogen to prevent a detonation of the gases in the combustion chamber. The control relay also activates the ignition box (Type Beru Zündgerät, with a secondary circuit delivering 7.5 kV and 40 mA). If the box is started the spark produces a continuous arc discharge. The spark plug delivers a power of 300 W, which is rather low compared to conventional ignition systems in aero engines (common systems use 200 V and 200 A  $\rightarrow$  0.4 MW [78]). Only combustible is routed through the ignition system, the necessary air for an inflammable mixture is taken from the recirculation zones of the swirl generators, pushing air backwards to the spark plug.

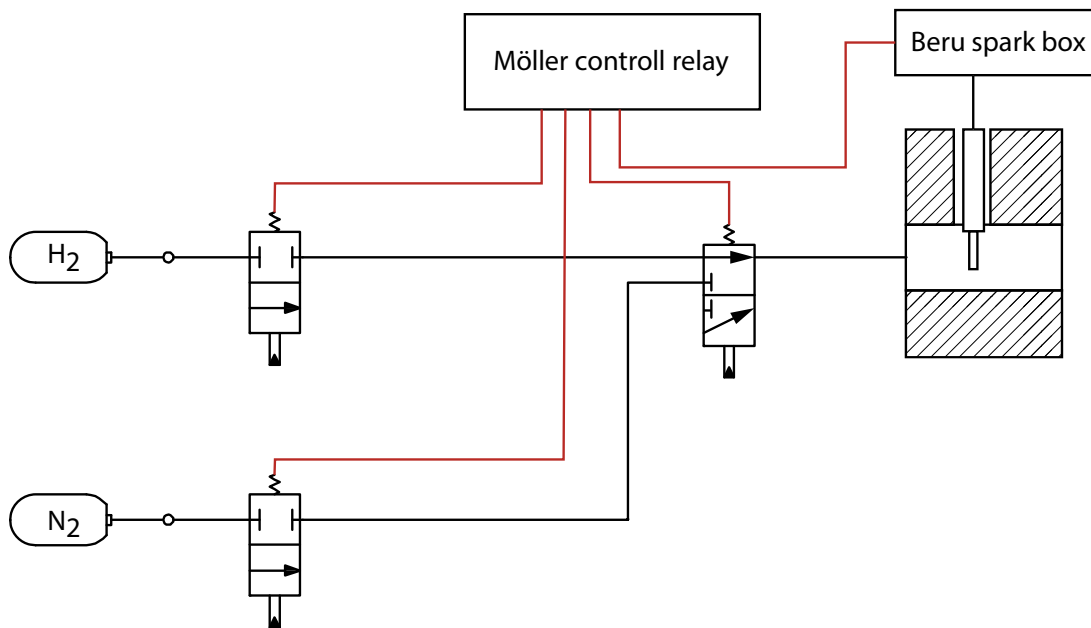


Figure 6.26: Schematic of the ignition control

# Chapter 7

## Initialisation and Main Flow Analysis

### 7.1 Atmospheric tests of ignition of the radial swirl combustor

In order to verify the chosen operation point an ignition test with the test combustor has been performed outside the laboratory at atmospheric pressure and ambient temperature  $T = 290$  K. supply. The tests have been made without liner (free-jet) and with liner (confined-jet). For the fuel supply, a surge tank filled with ethanol has been used. The necessary fuel pressure was provided using a nitrogen pressure cylinder. The fuel mass flow was controlled and measured by a manual rotameter.

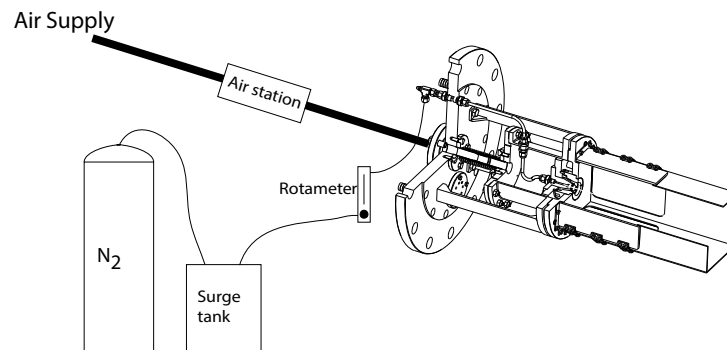


Figure 7.1: Test configuration

In the pictures below a variation of the airflow can be seen at constant fuel mass flow being regulated to the required reduced mass flow rate.

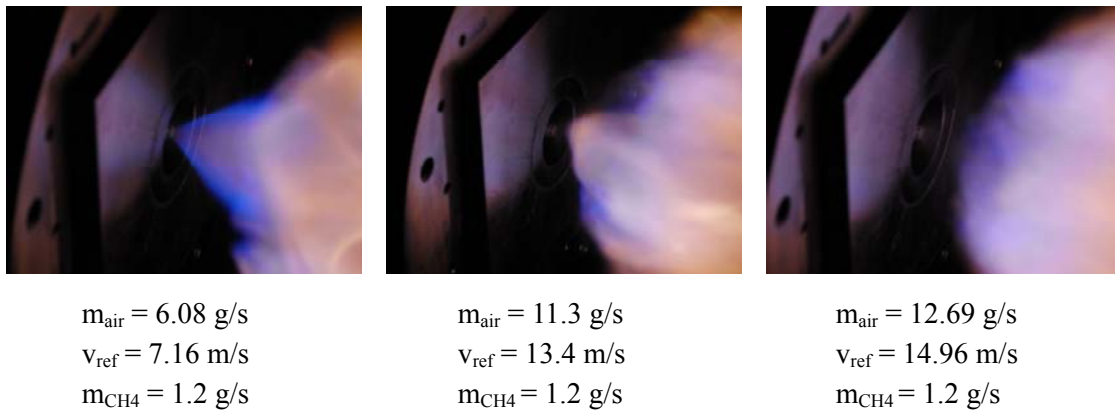


Figure 7.2: Free-jet combustion-test varying air-mass flow

At ambient conditions and in absence of cooling air, a part load operation was chosen which explains the relatively low reference velocities in comparison to the test case. The flame attaches in free-jet-mode at the tip of the pressure nozzle at part load and stabilizes around the internal recirculation zone. When augmenting the load, the flame gets a lifted structure (Figure 7.2). Under confined conditions, the absence of ambient surrounding air to be entrained allows the flame to attach to the outer diameter of the injector.

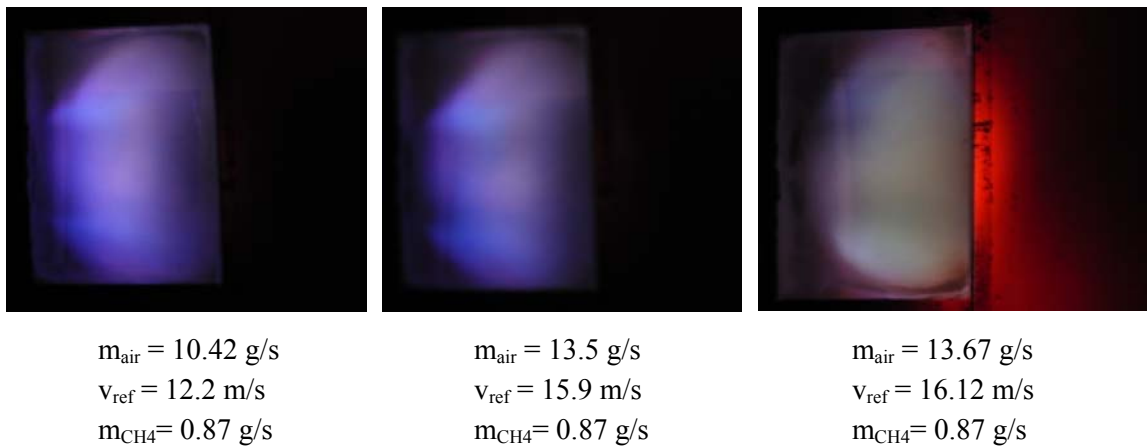


Figure 7.3: Confined-jet combustion-test varying air-mass flow

## 7.2 LDA Measurements

Before integrating the manufactured test chamber with the timecop air-blast combustor into the pressure vessel of the combustion laboratory, it was necessary to test the geometry for manufacturing reliability and comparability with the already manufactured version of the project partner ONERA. This was obligatory considering a final comparison of the evaporation measurement results of the chosen alternative fuel types from TU Graz with the atomization measurement results from the partner institution. To accomplish these requirements LDA measurements of the flow velocity components in 3 directions have been performed on free-jet and confined-jet configuration under atmospheric conditions and compared to existing data from ONERA Toulouse.

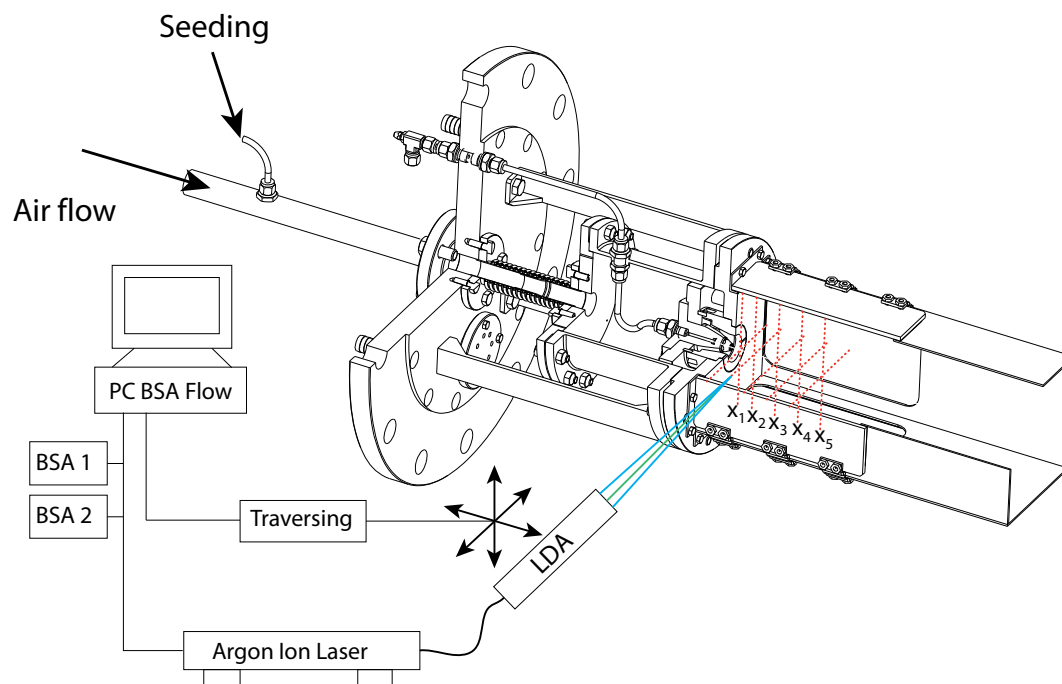


Figure 7.4: LDA Setup for flow analysis at ambient conditions

Figure 7.4 shows the LDA setup which was used for these purposes. The measurements were realized using a two-component LDA system (Dantec FiberFlow with two BSA processors BSA 1 and

BSA 2) and the data acquisition was done using the BSA-Flow software. Droplets of DEHS oil (Di-Ethyl-Hexyl-Sebacin-Ester) with a nominal diameter of  $0.3 \mu\text{m}$  were added as seeding material to the flow before the entrance of the airbox. The orientation of the laser optics has been changed to a rotation of  $45^\circ$  in order to improve the signal quality due to detecting nearly the same velocity magnitude in both fringe patterns. The positioning of the laser optics is performed with a Dantec lightweight traverse unit which can be moved in 3 directions fully automated using BSA-Flow. The acquired data is transferred to Matlab for further analysis.

The flow conditions in the radial swirl combustor were assumed being characterized by rotational symmetry. As a consequence the flow field has been detected alongside crossed lines at 5 different positions from the entrance plane ( $x_1=6 \text{ mm}$  /  $x_2=26 \text{ mm}$  /  $x_3=56 \text{ mm}$  /  $x_4=86 \text{ mm}$  /  $x_5=116 \text{ mm}$ ) (see Figure 7.4). The measurement grid for confined jet and free jet configuration are slightly different due to a visibility difference caused by the mounted liner. For free jet a constant measurement grid has been used with a constant radial step size of 2 mm. For confined jet configuration the grid has been the same for the outer zones but in the center ( $\pm 20 \text{ mm}$  from spray axis) it has been resolved in a finer manner.

The mass flow rate addressing to the reduced mass flow rate  $WR = 0.3$  has been regulated with a V-cone flow-meter and a manual pressure reducer. The compressed air was taken from the internal air circuit of the institute. Pressure and temperature have been measured steadily in order to adapt the operation points.

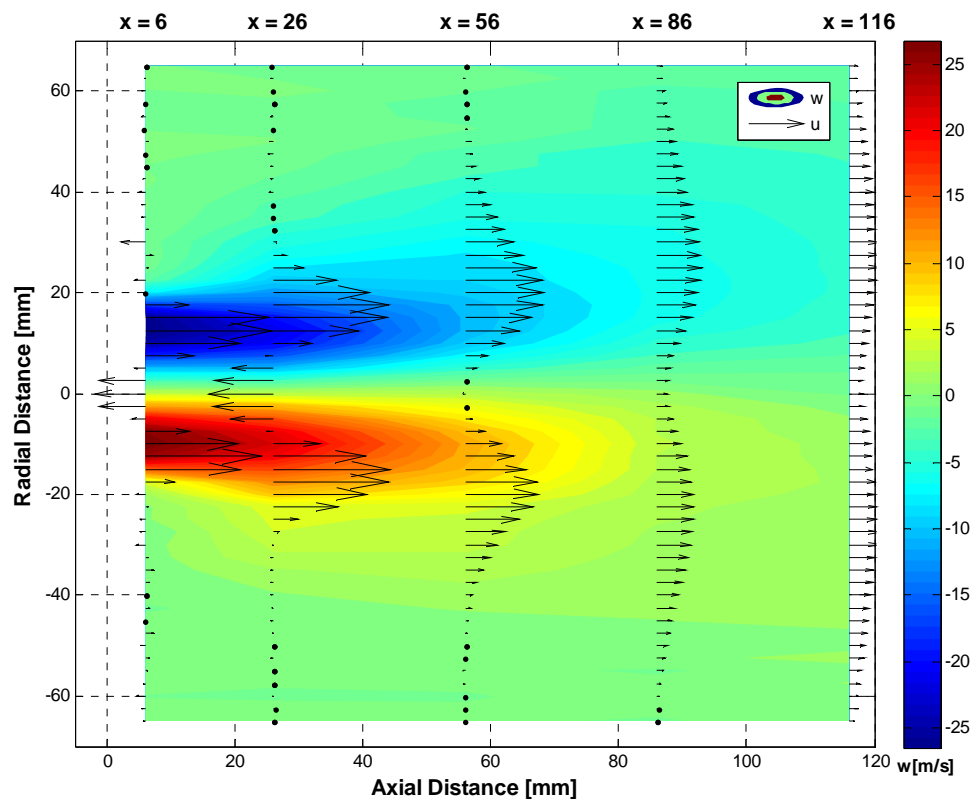


Figure 7.5: Radial-distribution of the axial velocity  $u$ , and the out of plane component  $w$  in free-jet configuration.

Figure 7.5 presents the LDA measurement results for the free jet configuration. The axial velocity distributions shown here as vector plot are mean values calculated out of the two results for  $u$  de-

rived from the orthogonal measurement cross taking its rotational symmetry into account. The out-of-plane-component  $w$  is plotted as colormap. The profiles for free jet configuration are very homogeneous and show a good symmetry alongside the spray axis ( $r=0$  mm).

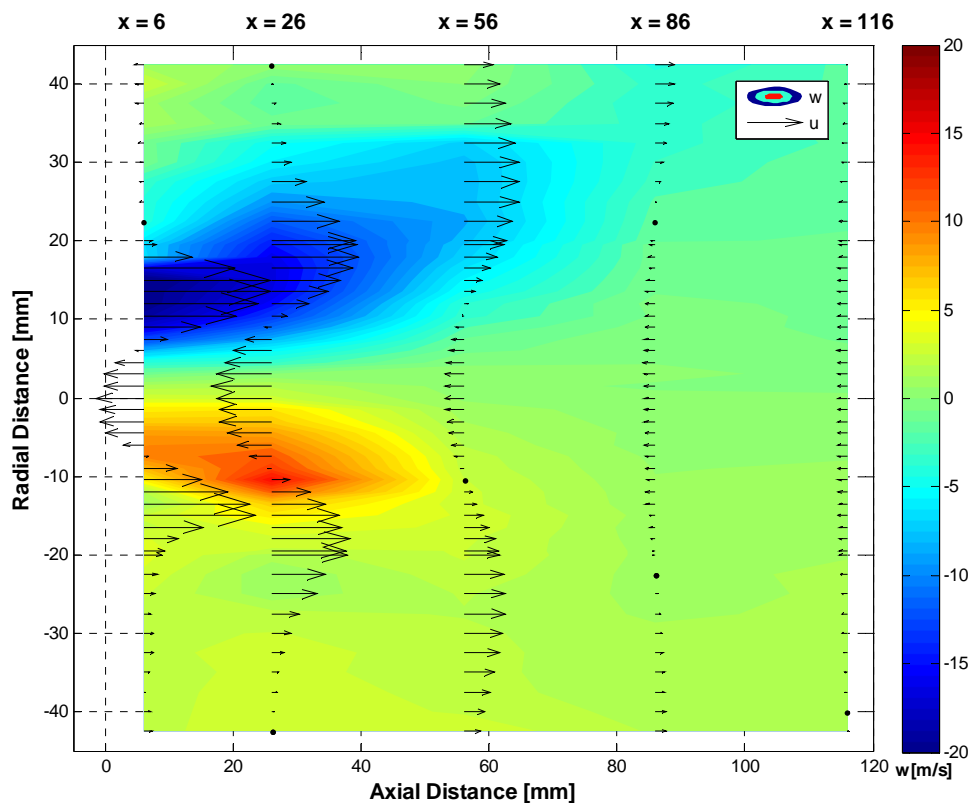


Figure 7.6: Radial-distribution of the axial velocity  $u$ , and the out of plane component  $w$  in free-jet configuration.

Figure 7.6 present the measurement results for the confined jet configuration. Again the distribution of the axial velocity has been determined using mean values. The vector plot again is very symmetric alongside the spray axis despite some deviations at the axial position close to the entrance plane. The colormap distribution of the out-of-plane-component  $w$  shows asymmetric behavior which is assumed to be caused by the rectangular shape of the liner.

$$S = \frac{2}{D_{sw}} \frac{\int_0^{2\pi} \int_1^{D_{swirl}/2} w r^2 \rho u dr d\theta}{\int_0^{2\pi} \int_1^{D_{swirl}/2} \rho u^2 dr d\theta + \int_0^{2\pi} \int_1^{D_{swirl}/2} r p dr d\theta} \quad (7.1)$$

An important factor for a flow field comparison of combustor geometries is represented by the swirl number, which is defined in ( 7.1 ) [76]. The ranges of the swirl are typically characterized by the threshold of  $S = 0,6$ .  $S < 0,6$  represents usually a very weak respectively non-swirl-stabilized flow, which means no zones of recirculation, while  $S > 0,6$  stands for a strong swirl number and in its case a swirl stabilized flow  $\rightarrow$  strong recirculation. The Swirl number has been determined for position  $x = 26$ mm ( $x/D_{swirl}=1$ ) from the entrance plane for both liner configurations. Results of this calculations were  $S = 0.78$  for confined-jet configuration and  $S = 0.74$  for free-jet configuration, which can be interpreted in a good swirl stabilization for both cases.

The results of this flow characterization have shown very good accordance to the existing data from the partner institution and could therefore set the path towards an installation of the whole conglomerate in the laboratory setup.

### 7.3 Setup Initialisation Test

Before entering the complex test set up, including the test cell, the after burner and the ignition device into the test rig of the combustion laboratory, it was necessary to initiate the setup and prove the functionality. Therefore again a provisional test setup has been installed outside the department building (Figure 7.7). The test cell including the evaporation tube was connected with the afterburner and all necessary methane and kerosene supply feeds have been connected. For the hot air needed in the evaporation tube an electric air heater was connected to the inlet air supply connected to the pressure vessel. This device uses the heater outlet temperature as control variable and was plugged in the 400 V high voltage supply. The air supply was taken from the internal pressurized air circuit from the laboratory and the mass flow was regulated by a rotameter installed before the electric air heater. Pressure and temperature of the supply air have been measured with a piezo-resistive absolute pressure pickup and a PT 100 temperature sensor installed before the rotameter. The cooling air was also taken from the internal circuit and the necessary temperature and pressure taken from the same measurement position as for the hot air due to deriving from the same supply circuit. The cooling air again was regulated by a rotameter and split up into several inlet tubes being positioned circumferentially on the pressure vessel.

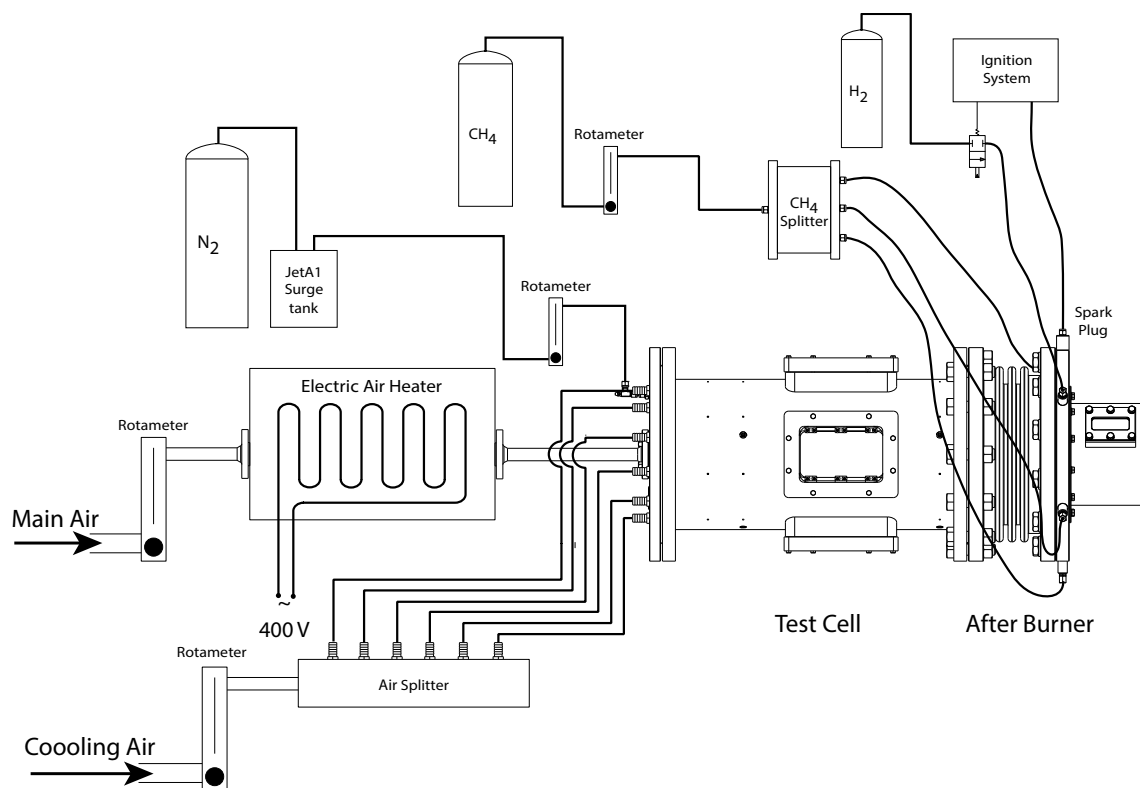


Figure 7.7: Initialisation Test setup



air mass flow cold	[g/s]	12,28	12,28	12,28	12,28	12,28	12,28
air to fuel ratio test chamber	Lambda		1,002	1,002	1,002	1,002	1,002
equivalence ratio test chamber	Phi		0,998	0,998	0,998	0,998	0,998
air to fuel ratio afterburner (global)	Lambda	6,219	1,576	1,683	1,798	1,862	1,928
equivalence ratio afterburner	Phi	0,161	0,635	0,594	0,556	0,537	0,519

## 7.4 IRE measurements with ultrasonic injector

For the familiarization into the used IRE measurement technique, an internship of several months at ONERA Toulouse has been performed funded by the European Commission's Marie curie fellow-ship.

At ONERA Toulouse a test bench has been built up based on a setup originally used at DLR Cologne [49] in order to investigate fuel concentrations in a monodisperse as well as in a polydisperse fuel spray. For this contribution only results connected to the latter were of general interest. Figure 7.1 shows the principle of the measurement setup.

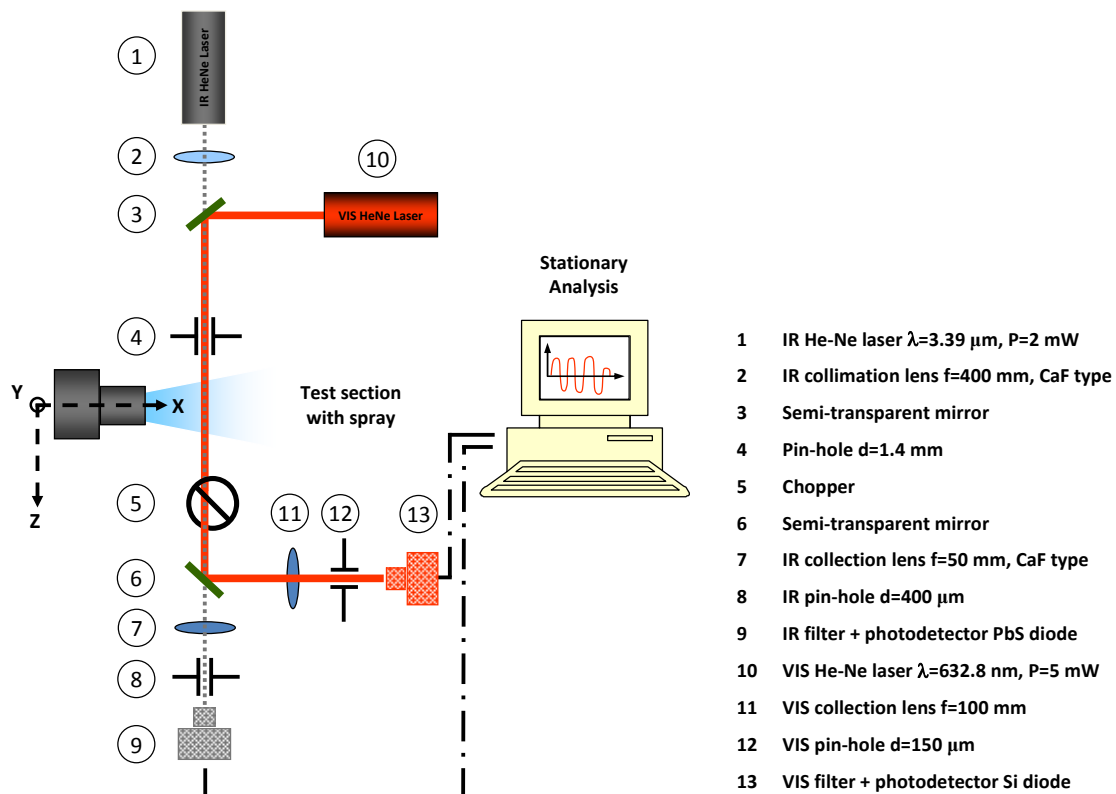


Figure 7.9: Schematic of the test bench

Two Laser light sources from Thorlabs, one for the visual range at 633 nm and one for the Infra-red wavelength at 3390 nm are employed (Table 7.2).

Table 7.2: Technical data of the laser sources

Description	H339P2	HRP050
Wavelength [nm]	3392	632,8
Polarisation	linear>500:1	linear>500:1
Power [mW]	2	5
Beam diameter [mm]	2.02	0.8
Operating Voltage [VDC]	2800	2400
Operating Current [mA]	6,5	5,25
Length [mm]	533,4	425,5
Diameter [mm]	44,5	44,5

These two light paths are centered using semitransparent mirrors. A signal chopper rotating with a tunable frequency range from 1 Hz to 6 kHz produces a time dependent signal which is used as main trigger source. The temporal resolved signal is detected by photo diodes. The visible detector is a Si-type photodiode which operates at ambient temperature with an output signal of 0,42 A/W and an optimal spectral range from 600 to 900 nm. Due to the low power output of the laser, the diode is connected to an integrated low-noise preamplifier/evaluation circuit. The transimpedance is 15 kV/A. To measure the amount of infrared radiation a PbSe-photoconductive detector is

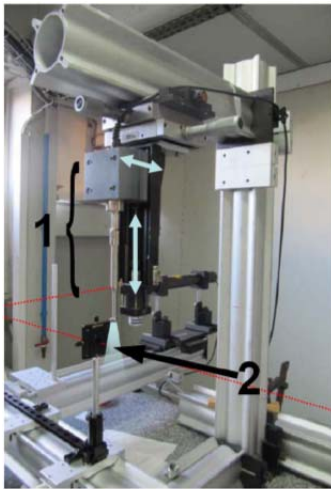


Figure 7.10: (1) Injector  
(2) Pinhole

employed. Its output signal reaches a maximum at an optimal wavelength range between 3 and 3,7  $\mu\text{m}$ . To minimize thermal noise it is embedded in a thermoelectric heat sink which regulates the operating temperature. Again, due to the low laser power, a pre-amplifying device follows the diode. The transfer, conditioning and storage of the pre-amplified signals are assured by a three-component acquisition system from National Instruments. It consists of a connector box, which bundles the incoming signals, the acquisition hardware, for digitalization and conditioning, and the acquisition software to control the hardware parameters and to store the processed data. The connector box: To connect the experimental signals to the PC-system a connector box type NI BNC-2090A is employed. Sixteen analog input BNC connectors provide access for sixteen single-ended or eight differential channels. In this work the second option is used to further eliminate signal noise. The channels were calibrated by a stabilized tension generator for a range of

$\pm 10$  [V] with an average error of less than 0.1 [%]. For transmission of the signals to the acquisition card inside the PC two 68pin connectors are available.

The acquisition hardware consists of a data acquisition (DAQ) device NI 6289 PCI card of National Instruments M-Series. It allows to scan up to 32 analog input channels at 500k [samples/second] maximum at 18 bit. Timing resolution is 50[ns] at an accuracy of 50 [ppm] of the sample rate. In the present experiments, the acquisition rate was kept below 250[khz] for three channels simultaneously to avoid buffer overflow at data storage.

The acquisition software: The last element in the acquisition chain is a Labview<sup>TM</sup>-based software tool which allows the experimenter to control the main acquisition parameters and to store

the data. A modular layout of the source code has been chosen to facilitate the implementation of additional acquisition channels. The acquired data is stored in the Labview-native .tdms format. This file structure is optimized to store a maximum of values and their metadata in smaller files than the regular text formats. Conversion tools for most software packages (including MS Office and Matlab) are provided [56].

The poly disperse spray cone is passed through the concentric laser beams (VIS and IR) which are static. The atomizer nozzle is moved from the left end to the right end of the cone varying horizontal and vertical positions. The fuel supply pressure is denoted with 1.5 bar and is delivered by a pressurized air reservoir which avoids pressure oscillations. The fuel temperature is held at 60°C using a continuous flow heater. The temperature is measured at the injector head before and after each testing series using a thermocouple. The fuel is injected into ambient conditions of approximately 1 bar air pressure at a temperature of 20°C. The spray is generated using an ultrasonic atomizer from Sonics (USVC 130 AT). This atomizer is equipped with a flat tip nozzle allowing a maximum volume flow rate of 1.67 ml/s.

Figure 7.11 shows the droplet size distributions of the injector varying the radial distance ( $y$ ) from the spray center ( $y = 0$ ) [58].

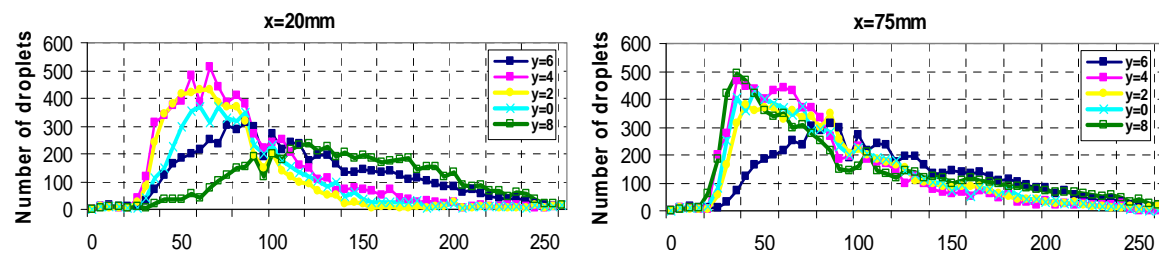


Figure 7.11: Radial Evolution of Droplet size [ $\mu\text{m}$ ] distribution at  $x = 20\text{mm}$  (top) and  $x = 75\text{mm}$  (bottom) n-octane  $\dot{m} = 35 \text{ ml/min}$  [58]

Figure 7.12 shows the diameter mean values as a function of the radial distance which both had been measured in the frame of the investigations of Bodoc [58]

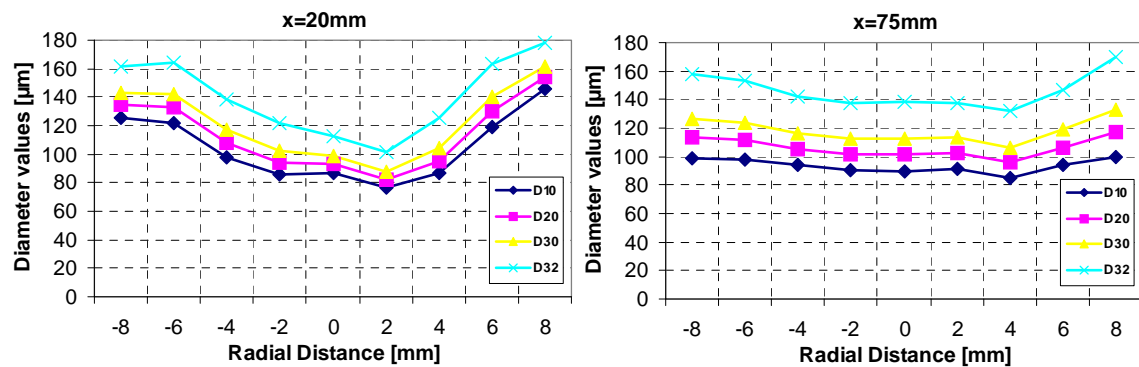


Figure 7.12: Mean values of the droplet diameters determined by PDA at  $x=20\text{mm}$  (top) and  $x=75\text{mm}$  (bottom) n-octane  $\dot{m}=35 \text{ ml/min}$  [58]

The injector uses a piezoelectric ceramic to generate oscillations with ultrasonic frequency (20 kHz). The oscillation is transferred to the liquid film which covers the injector head (see Figure 7.13). This film, submitted to the high frequency oscillations, creates a wave pattern at the surface. When critical amplitude is reached, the waves degenerate and droplets of liquid are ejected

from the liquid surface. The size distribution and the spray expansion are controlled by the amplitude of the generator excitation and by the liquid flow rate.

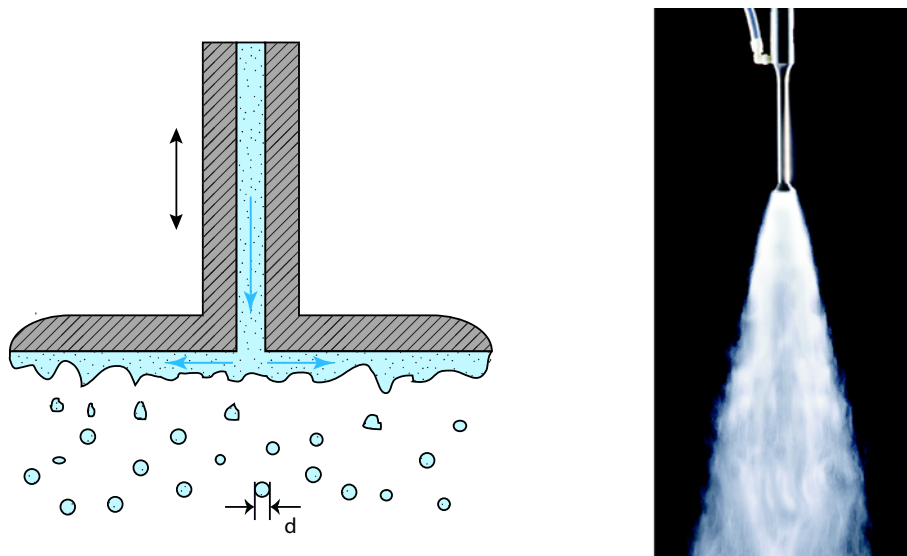


Figure 7.13: Ultrasonic atomizer Sonics USVC 130 AT

The amplitude which regulates the spray cone angle is tunable in percentage steps. Higher amplitude produces a bigger spray-cone angle. The optimum referring to the stability of the cone has been found between 28 % and 35 % amplitude. The liquid flow is regulated by a manually tunable rotameter. It has to be calibrated for different liquid types.

The diagrams demonstrate that the injector fulfills the assumption of a droplet mean size distribution higher than  $20\ \mu\text{m}$  for flows  $\geq 35\ \text{ml/min}$ . The measurements in Figure 7.12 have been done at a vertical position of 20 mm and 75 mm from the injector head varying ten radial positions. For illustration reasons only five positions are presented. In Figure 7.12 the resulting mean diameter values of the particular radial positions are diagrammed also at a vertical position of 20 mm and 75 mm from the injector head.

For the position  $x = 20\ \text{mm}$  also a simulation of the fuel evaporation has been done for this particular injector. In order to compare the results of the extinction measurements with the simulation results it was especially focused on this position.

#### 7.4.1 Beam Analysis

The prepared optical setup has been assembled and tested. A very important requirement to guarantee the certainty of the measurement results is a precise alignment of the laser beams. Therefore the lasers have been aligned several times iteratively, using the visual part of the IR device.

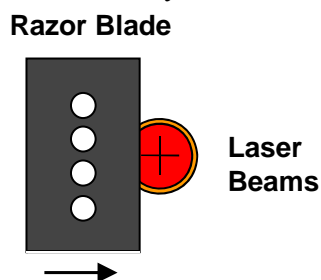


Figure 7.14: Beam diameter measurement

the lasers have been aligned several times iteratively, using the visual part of the IR device.

The methodology was to position the IR beam first by using a cross line which is mounted on a movable carrier on the measurement rail. The IR laser has been moved that way that the visual part of the light was concentric with the cross line on several positions of the rail. The mirrors (Figure 7.9) were disassembled because of the reflection of the visual part of the IR light. After this alignment the mirrors were remounted and the visual laser

beam was positioned the same way as the IR laser before by using the cross line. After this alignment the pinhole was mounted and the laser diodes were moved to the position with the maximum signal intensity, then the pinholes in front of the laser diodes were remounted and moved to the maximum intensity position. This procedure has been repeated several times in order to improve the concentricity of the beams. In order to analyze the beam diameter and the concentric and parallel positioning of the laser paths, a razorblade method (Figure 7.14) has been used with a step-wise displacement ( $dx = 0.1\text{mm}$ ) towards the laser light and the extinction of the beam was measured at several axial positions.

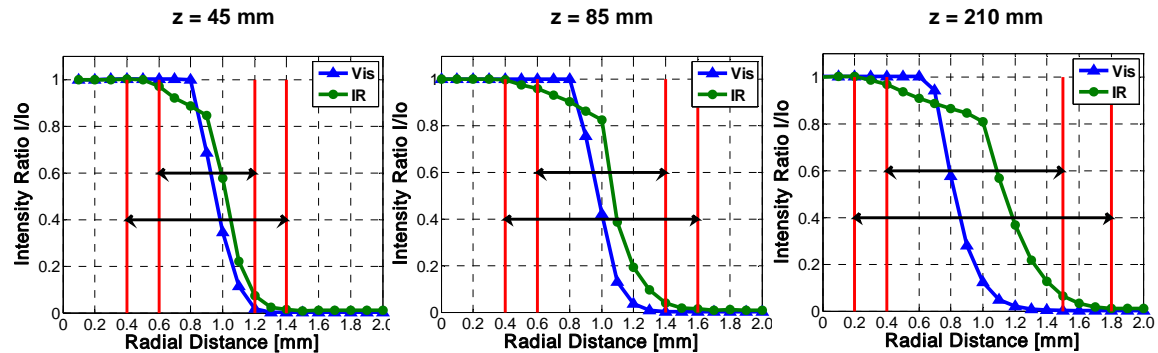


Figure 7.15: Beam diameter / diffraction analysis with razorblade (from left to right) for positions  $z_1 = 45\text{mm}$  /  $z_2 = 85\text{mm}$  /  $z_3 = 210\text{mm}$

The measurements have been done at horizontal positions 45 mm, 85mm and 210 mm distance from the pinhole (Figure 7.15). Leading laser light through a circular aperture such as a pinhole, results in a diffraction of the beam which is characterized by intensity rings around the main light profile (Gaussian). The first ring around the profile determines the limit of the Airy disk. Preliminary calculations for the expected diameter of this ring have been done (Figure 7.16).

Distance Pinhole	Beam Diameter IR [mm]	Beam Diameter VIS [mm]
<b>Calculated beam diameter</b>		
45 mm	1,36	1,07
85 mm	1,7	1,13
210mm	2,736	1,324
<b>Measured Beam diameter</b>		
45 mm	1	0,6
85 mm	1,1	0,7
210mm	1,6	1,1

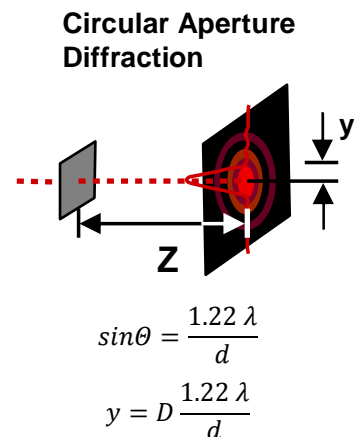


Figure 7.16: Calculation of the circular aperture diffraction / comparison with measurements

The results show that there is a difference between the measurements and the calculation which is assumed to be caused by an imprecise focalization between the lens and the pinhole as well as in the diffracted shape of the beam due to the use of only one collection lens.

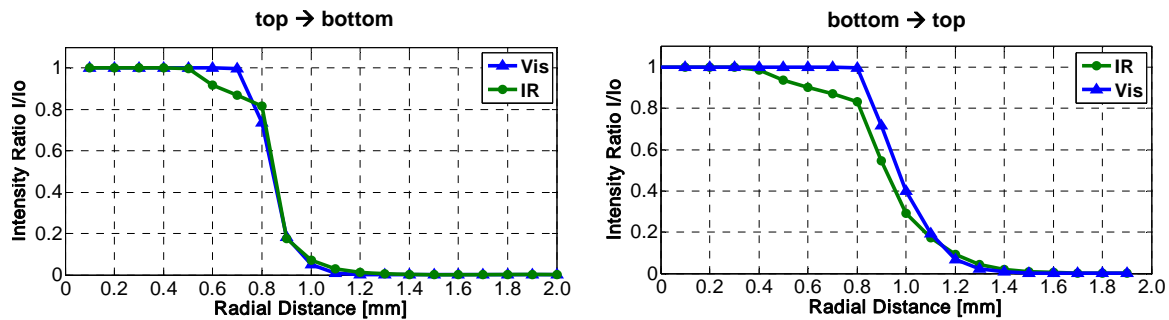


Figure 7.17: Laser beam analysis with razorblade in vertical direction

In order to analyze the concentric positioning this measurement procedure was repeated at an axial distance of 45 mm from the pinhole for all directions (top  $\rightarrow$  bottom, bottom  $\rightarrow$  top, left  $\rightarrow$  right, right  $\rightarrow$  left) (Figure 7.17 and Figure 7.18).

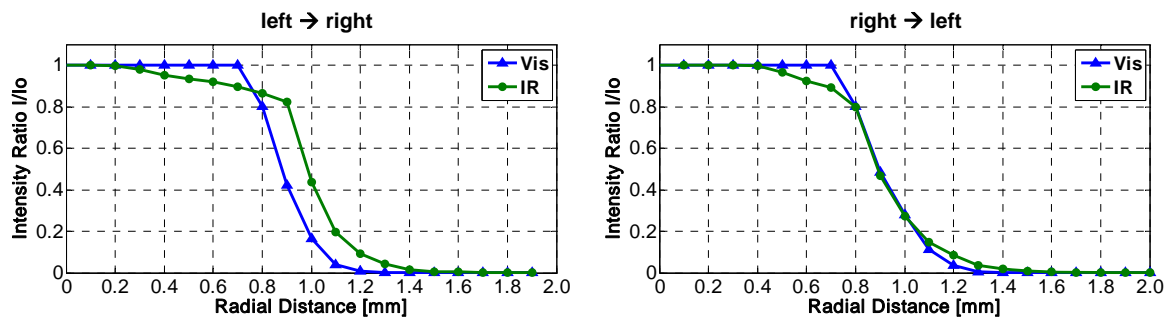


Figure 7.18: Laser beam analysis with razorblade in horizontal direction

The trend of the measured extinction values is asymmetric for the VIS as well as for the IR range. Especially for the visual range the curves have an unsteady run at about 0.7 mm. This effect occurs for all four directions, which neglects the assumption that the beam shape could have an influence on this. There is no reasonable explanation for this tendency. However, the results have shown a very good alignment with a maximum eccentricity of 0.05 mm.

#### 7.4.2 Tests on the fuel spray

After the iterative alignment and the positioning analysis results, the tests on the real fuel vapor spray have been started. As a testing fuel n-octane has been used. The methodology was to vary the injection parameters such as fuel mass flow, amplitude excitation of the piezo-actuator, horizontal distance from the main pinhole (Figure 7.9 Nr. 4) and vertical distance from the beam center in order to investigate the influencing parameters on the concentration value measurement. The laser devices are stationary while the injector is movable in three axes. The presented measurement series have been produced by passing the spray cone through the laser beams from one end to another. The Injector has been displaced stepwise with  $dx = 1$  mm including a radial range of 40 mm (-20 mm  $\rightarrow$  20 mm radial distance). Figure 7.19 shows the first variation of the fuel mass flow. It can be seen that at low fuel mass flows the intensity ratio  $I/I_0$  for the visual range is smaller than for the IR range which would lead to a negative vapor concentration calculation  $\rightarrow$  equation ( 5.37 ). This tendency is detectable over the whole range of the spray cone. Increasing

the mass flow resulted in a different intensity ratio at 30 ml/min and further in an inversion of the results at 35 ml/min.

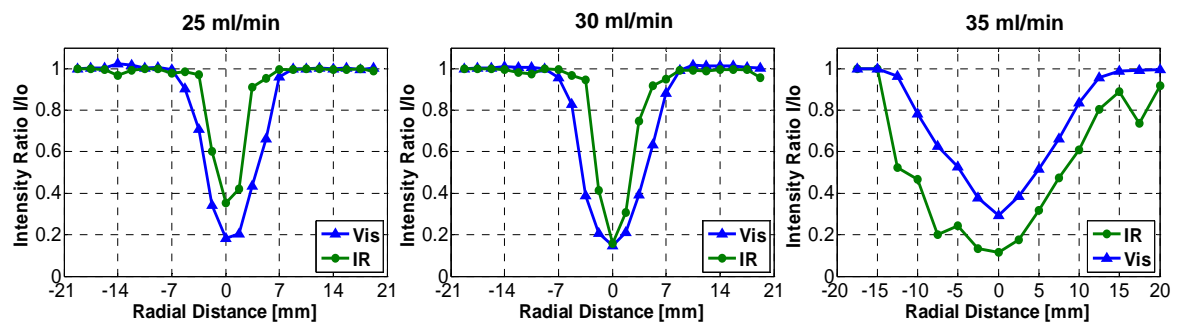


Figure 7.19: Extinction measurements of a n-octane spray produced by an ultrasonic injector / variation of the fuel mass flow (25 / 30 / 35 ml/min) at 20 mm vertical distance from the beam center to the injector head and 45 mm horizontal distance from the spray center to the main pinhole.

It is assumed that for very low mass flow rates the area mean diameter  $D_{20}$  of the spray does not fulfill the assumption of being higher than  $20 \mu\text{m}$ . The inversion of the extinction results takes place at 35 ml/min which is exactly the value that has been investigated in the anticipated injection simulation analysis of ONERA Toulouse. This allows a direct comparison with the simulation results which is going to be presented later.

The variation of the excitation amplitude parameter of the injector is presented in Figure 7.20. It can be seen here that it seems to influence only the spray cone shape as it is described in the injector manual. A higher excitation amplitude results in a broader spray cone, which can be identified focusing on the transition of the curve form from 28 % to 31 % amplitude. The difference between 31% and 35% is not significant. It is assumed that the area mean diameter  $D_{20}$  fulfills the boundary condition of being higher than  $20 \mu\text{m}$  due to the tendency of the extinction to be in a correct relation, which means a positive vapor concentration over the whole spray cone in all amplitude variation series.

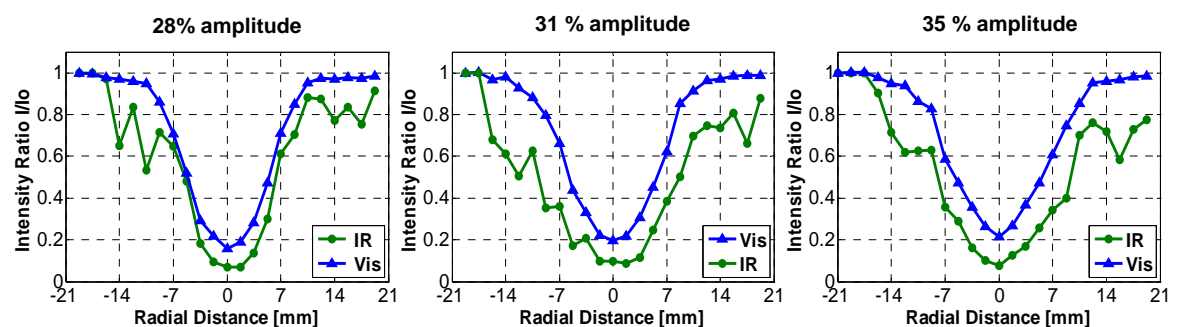


Figure 7.20: Extinction measurements of a n-octane spray produced by an ultrasonic injector / variation of the injection parameter (28 / 31 / 35 % amplitude) at 20 mm vertical distance from the beam center to the injector head and 45 mm horizontal distance from the spray center to the main pinhole.

Further measurement series focused on the mass flow rate at 35 ml/min. Also, the influence of the polarization has been investigated by a systematical changing of the polarization direction of the visible laser beam. The polarization filter has been installed between the laser and the first mirror

of the visible light path. There were no influences detectable concerning the polarization direction. Having found this stable injection parameter configuration, more measurements have been done to be able to present homogeneous curve results, which was difficult due to the instability of the injector. However there has still been a divergence on the right hand side of the curve (Figure 7.21 (left)). The extinction for the IR range remained at a certain level. The explanation for this phenomenon is that the ambient vapor concentration reaches a non-negligible level after the duration of half an hour for one measurement series.

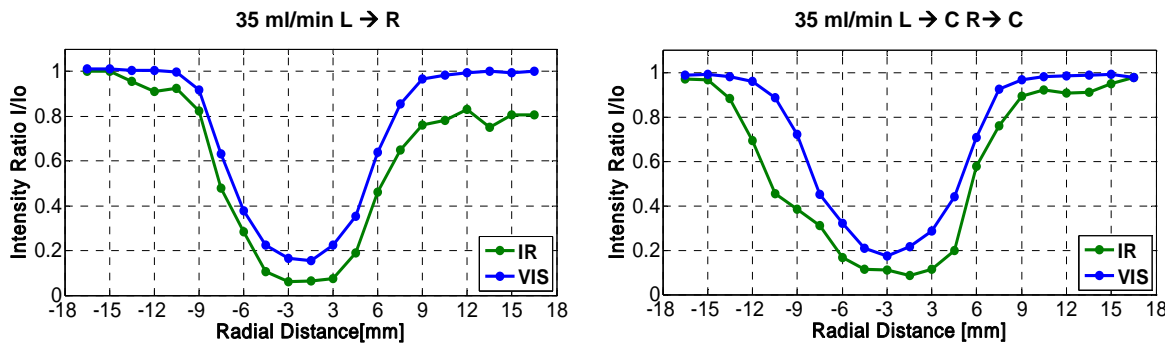


Figure 7.21: Stable extinction measurements at 35 ml/min from left to right (left) / from left to center and right to center (right)

For the following series the movement of the injector has been changed from the left hand side of the spray cone to the center and then from the right hand side of the cone to the center. The remaining vapor was blown outside of the detection area by pressurized air in the middle of the series before changing the direction. Figure 7.21 shows the suchlike achieved results. There is a significant change on the right side of the curve noticeable.

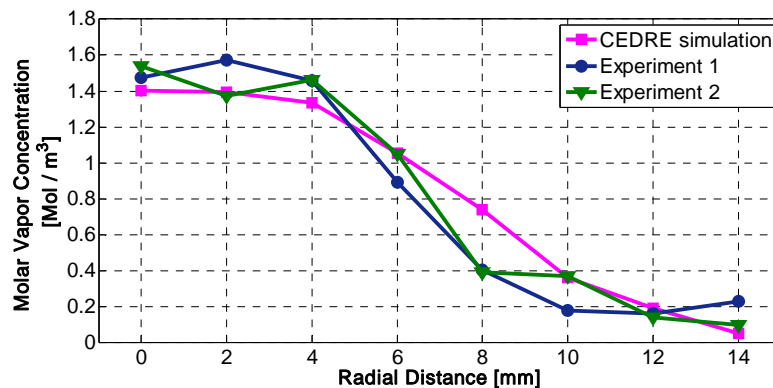


Figure 7.22: Comparison of deconvolution results with simulation results

The measurements presented in Figure 7.21 on the right have been repeated several times with the same fuel mass flow rate (35 ml/min) and the same ambient and boundary conditions. The suchlike achieved results have been deconvoluted by the above presented Onion-Peeling algorithm and the most homogeneous results (concerning the injector stability) have been compared with the simulation results of Bodoc [58] achieved with CEDRE code at ONERA Toulouse.

Figure 7.22 shows the deconvoluted results of the measurements performed at the very end of the investigation. Experiment 1 (blue marked) and Experiment 2 (green marked) have been performed serially. The absolute values of the vapor fraction between these two series show a difference of

about 10 % to 12 % (except for points at radial distance 10 mm and 14 mm with 50 %), which is in quite good accordance taking into account an assumed measurement error of about 10 % for the complete IRE measurement chain. The comparison of the numerical simulation results (magenta) achieved by Bodoc [58] using preheated (60°C) n-octane at a fuel mass flow rate of 35 ml/min and the experiments 1 and 2 shows a similar tendency with a difference of approximately +/- 0,2 Mol/m<sup>3</sup> between the point results, except for point 8 mm radial distance with +/-0,35 Mol/m<sup>3</sup> difference.

## Chapter 8

# IRE measurements

### 8.1 Setup

The measurement setup used for the vapor measurement investigations in the laboratory of TU Graz is principally identical to the one used for the aforementioned preliminary investigations at ONERA Toulouse concerning the evaporation of n-octane. A slight change had been performed in the optical setup. As a major problem in the original setup has been identified in the dominant diffraction of the laser beams especially in the infrared range an inverse Gallilean beam expander (Figure 8.1) has been installed in the IR path instead of the collimation lens after the outlet of the IR laser.

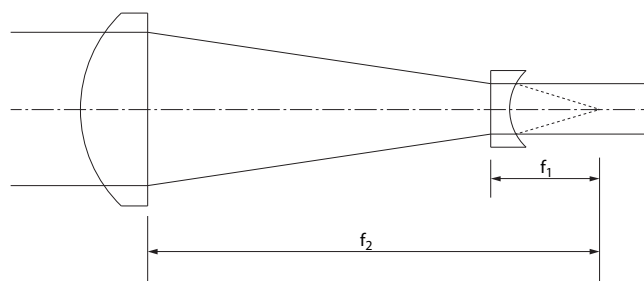


Figure 8.1: Inverse Gallilean Beam expander

With this beam expander it is possible to compensate the beam diffraction defined by equation ( 8.1 ) in which  $w_0$  is the initial beam diameter and  $\lambda_z$  the according wavelength. Also the Gaussian beam diameter of the IR laser can be reduced to the same amount as it is for the visual range.

$$w(z) = w_0 \left[ 1 + \left( \frac{\lambda_z}{\pi w_0} \right)^2 \right]^{\frac{1}{2}} \quad (8.1)$$

Due to the signal slightly lying in the saturation range of the diodes, intensity filters have been used for both, the visual and the infrared paths to reduce saturation effects. For the visual range standard neutral density filters were installed while for the IR range a series of infrared transmissible quartz glass was positioned after the beam expander. Concerning the data acquisition and post processing routines, identical components and software has been used as explained in chapter 0.

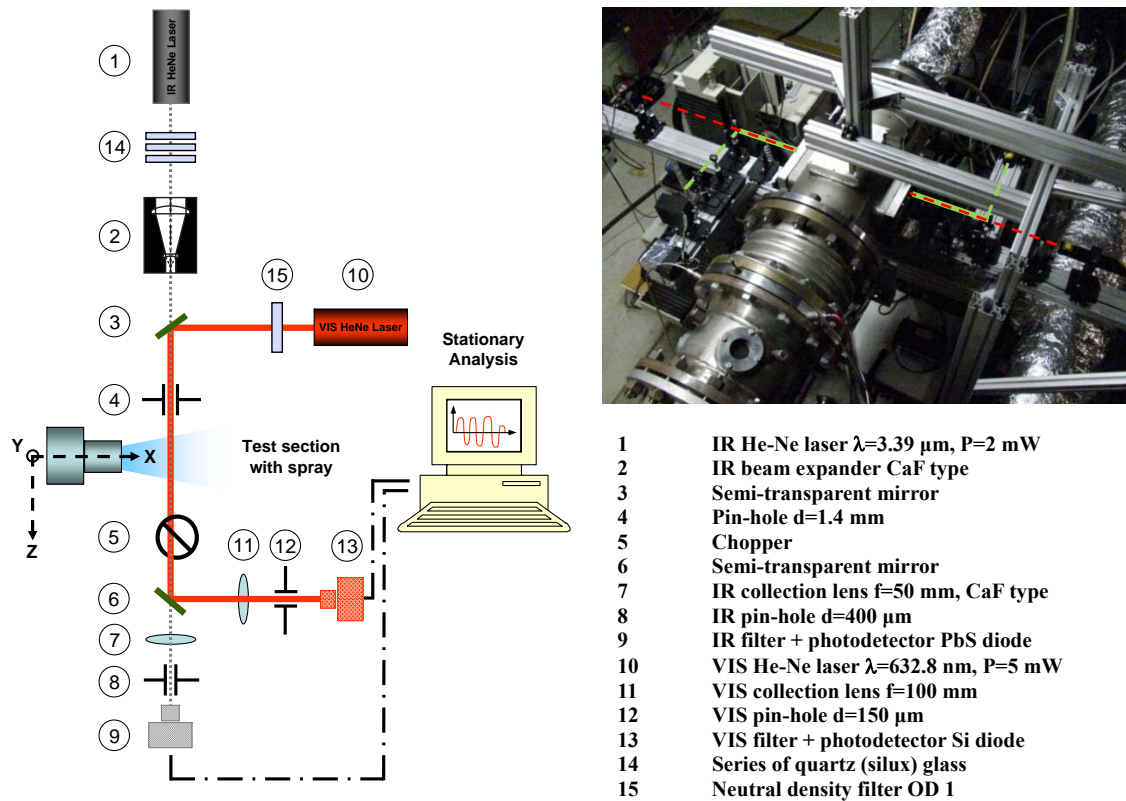


Figure 8.2: Schematic of the test bench (left) / Picture of the manufactured setup (right)

The Mercato test chamber has been integrated into the existing test rig which means it is static and not movable. As a consequence the measurement setup has to be moved to detect the interesting factors at the required points in the grid. Therefore a CNC Traversing unit from Franke has been installed in the laboratory.

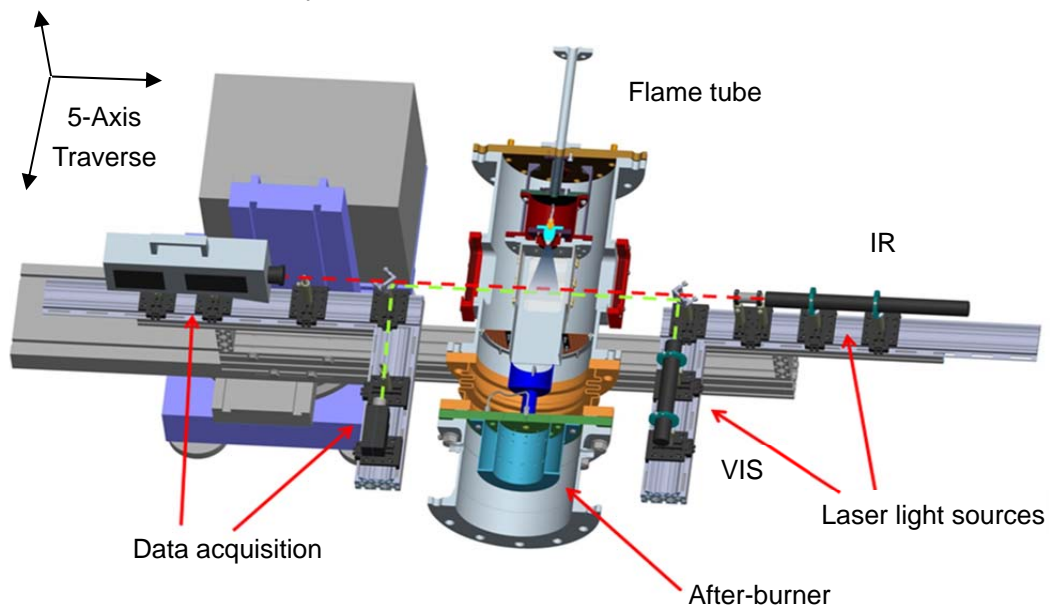


Figure 8.3: 3D CAD Model of the setup

With this unit it is possible to move the setup in 3 translational and 1 rotational axis within the entire measurement grid. So the optimal signal quality influenced by mirroring effects on the win-

dows was able to be located by moving the setup in 4 directions. Since sensitivity of the system to ambient vibrations is identified to be a major influence on the signal stability, a mechanical decoupling of the test rig was necessary. To effectively decouple this load from the vibrations in the stands, four pneumatically adjustable elastomer supports were fixed at the corners of the unit.

As the spray analysis of ONERA has shown the distribution of mean particle diameters (SMD) is tending towards values below 20  $\mu\text{m}$  at a distance of 30 mm downstream of injection outlet (IO). The lowest mean particle diameter being a limiting factor for the use of this technique resulted in a planned measurement grid which focuses on the distances  $x=6$  mm and  $x=15$  mm from IO. This choice for the formation of the measurement grid has been identified as the best compromise taking into account the coincidence of position 15 mm with ONERA's grid positions 15 mm and 30mm and the measurement grid for the Laser Doppler Anemometry measurements performed for this contribution starting at 6 mm from injection outlet.

$$\bar{c}_m = \frac{1}{\alpha(p, T)L} \ln \left( \frac{(I/I_0)_{VIS}}{(I/I_0)_{IR}} \right) \quad (8.2)$$

An additional measurement grid line is positioned at  $x=156$  mm in order to determine the absorption coefficient. Figure 8.4 shows a spray visualization at 5 bar and 553K injecting the reference fuel FSJF with an equivalence ratio of  $\phi=1$ . Blue marked is the spray axis and the red lines represent the positioning of the measurement points. It is assumed that the fuel air mixture at position 156 mm is completely evaporated and homogeneous.

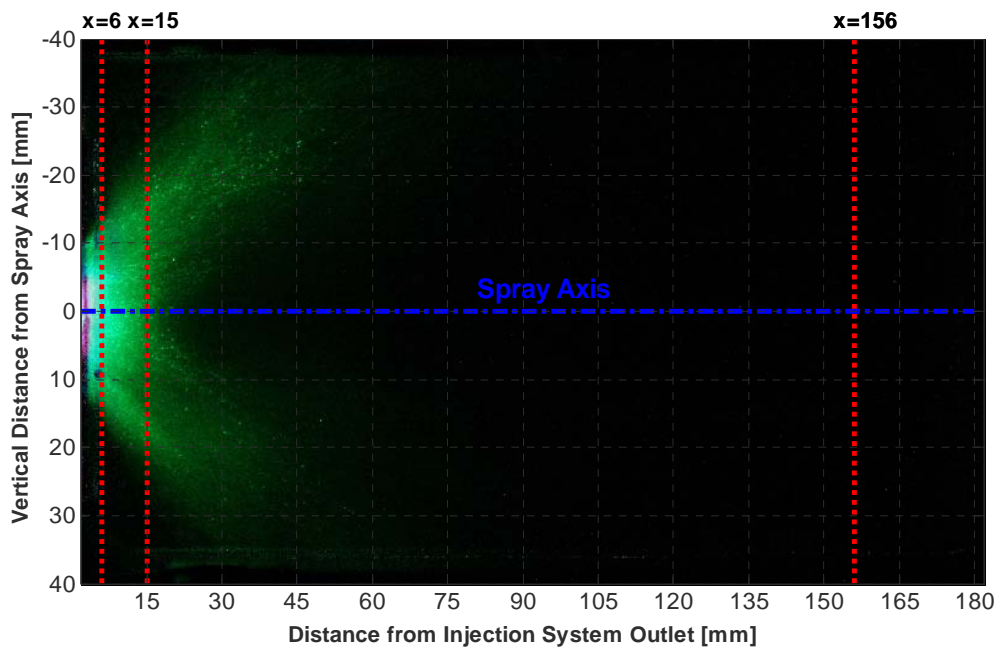


Figure 8.4: Spray visualization (FT-SPK 5 bar 553K) with superimposed measurement grid

Knowing the injected fuel mass flow, the air volume flow at constant pressure and temperature level in the test chamber allows to determine the molar vapor concentration  $C_m$  in the volume. By measuring the extinction of the IR light at this position (while the visual light is not affected due to not having any droplets here) it is possible to determine the absorption coefficient by using equation ( 8.2 ). The measured extinction is averaged over the whole volume and results in a

mean absorption coefficient  $\alpha(p, t, \lambda)$  (Figure 8.5). Having determined this coefficient now, it is possible to calculate the molar vapor concentration  $C_m$  with the data for the visual and IR extinction at each point in the measurement grid.

## 8.1.1 Results

### 8.1.1.1 Determination of the Absorption Coefficient [ $\text{cm}^2/\text{mol}$ ]

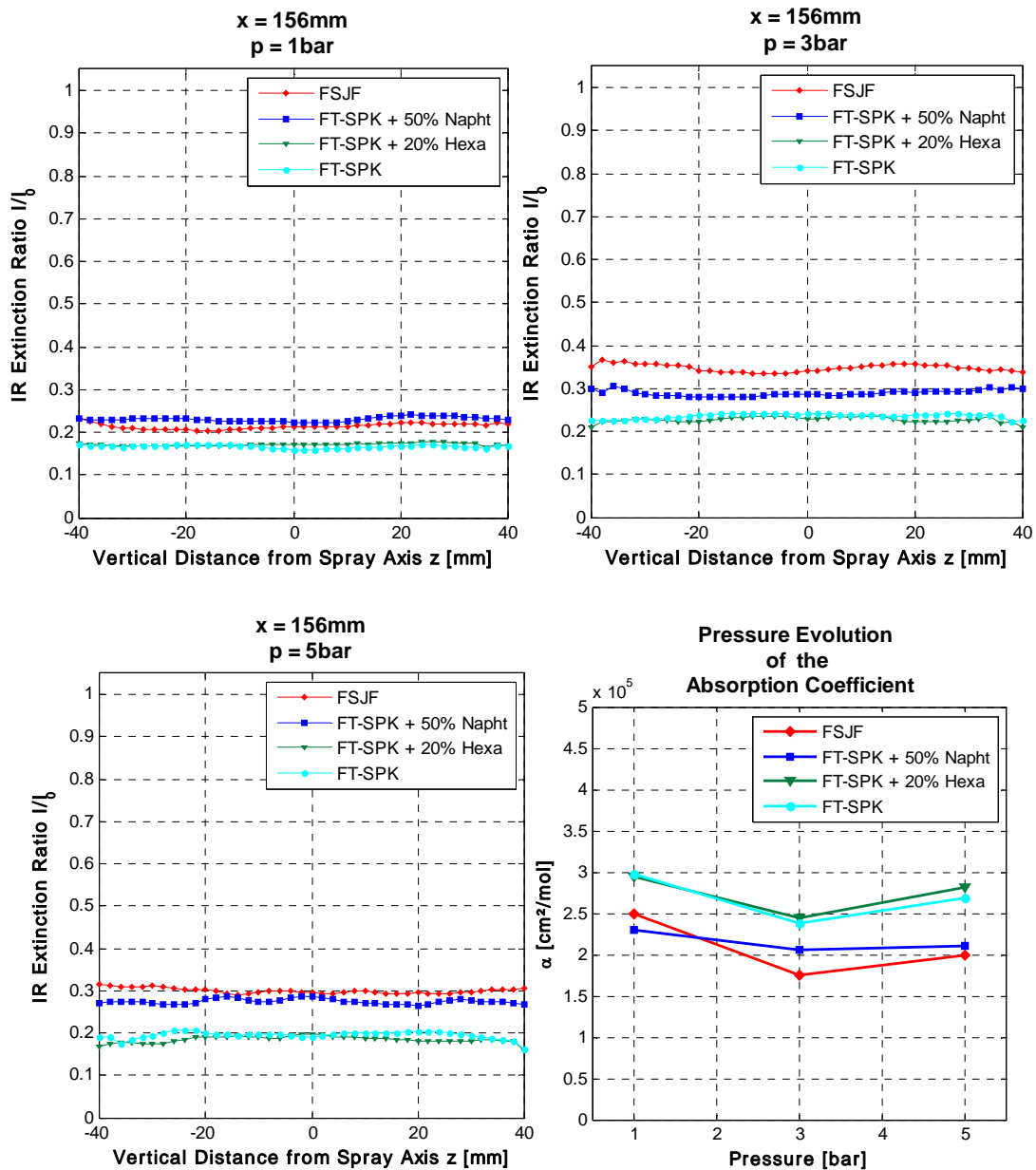


Figure 8.5: IR Absorption measurements at  $x=156\text{mm}$  downstream of injector outlet for 3 pressure levels (Top Left/ Right/ Bottom Left) and resulting absorption coefficients (BR) ( $T=553\text{K}$ )

The results of the extinction measurements for the IR wavelength at position  $x = 156\text{ mm}$  at 1 bar, 3 bar and 5 bar and elevated temperature are presented in Figure 8.5. The IR signal is proportional

to the presence of fuel vapor (equation ( 8.2 )) and the measured intensity ratios show that the distribution of the fuel vapor concentration is homogeneous over the full height of the measured volume. Only in the boundary region a slight diminution of the extinction can be detected which is assumed to be caused by the boundary layer of the flow field. The determined absorption coefficients coincide with averaged values for comparable fuels taken from literature. They show a pressure dependency which has the same trend for all four fuel samples (Figure 8.5 bottom/right). Only for FT-SPK + % 50 naphthenic cut the tendency for the absorption coefficient is characterized by a small deviation at 1 bar pressure level resulting in a flat devolution compared to the other fuel samples. The tendencies of the absorption coefficients to have higher values at atmospheric pressure and the minima at 3 bar absolute pressure are assumed to be caused by different oscillation and rotation states in the molecules for several pressure levels which are responsible for the absorption spectra and also depending on the different complex chemical compositions of the tested fuel samples.

### 8.1.1.2 Determination of molar vapor concentrations $C_m$ [mol/cm<sup>2</sup>]

Concerning the actual measurements of the molar vapor concentration for the proposed fuel samples the afore determined absorption coefficients together with the penetrating length  $L$  of the laser beams through the measurement volume serve as the required parameters for solving the simplified Beer Lambert law (equation ( 8.2 )) by measuring the extinction ratios  $I/I_0$  for the visual and the IR path. This has been performed for positions  $x = 6$  mm and  $x = 15$  mm axial distance from injection outlet at 1, 3 and 5 bar absolute pressure. The following figures (Figure 8.6 - Figure 8.11) present the extinction measurement results on the left hand side for the IR and the visual optical path and the calculated molar vapor concentrations of the fuel samples on the right hand side.

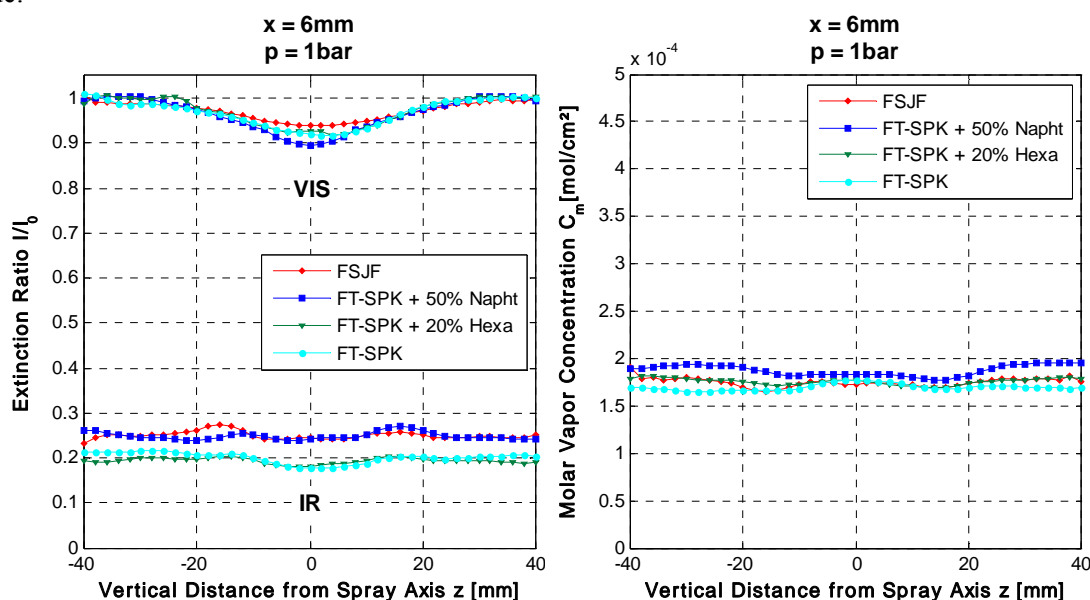


Figure 8.6: Extinction ratios in the visible and IR range for the different fuels (left)/Calculated molar vapor concentration (right) at atmospheric pressure 6mm downstream of IO ( $T=553$ K)

In Figure 8.6 the measurement results for the first position  $x = 6$  mm from injection outlet at atmospheric pressure are presented. It can be seen here that the visual signal on the right hand side,

which is characterizing the droplet density due to diffraction on the droplet surfaces, shows a very homogeneous curve for all samples with a maximum of extinction respectively minimum of extinction ratio in the middle. From the detected IR signal derive very high values of extinction, which leads to the assumption of an intense recirculation of fuel vapor due to also being present in the boundary zones of the combustor. Around the zones of the hollow cone which has its boundaries at around  $z = +15/-15$  mm (compared with Figure 7.6) it can be seen that the extinction is lower due to high flow velocities in stream direction (out of recirculation zone). Calculating the mean molar vapor concentration using equation ( 8.2 ) results in the diagram on the left hand side of Figure 8.6. The curves for the concentrations coincide except for FT-SPK + 50% naphthenic cut which seems to evaporate slightly better than the others. As a consequence of the remaining vapor in the boundary zones it is not possible to perform an Abel transform to obtain point results. This transform algorithm requires zones of zero concentration values in the boundaries and therefore only line of sight results in mol/ cm<sup>2</sup> are presented here.

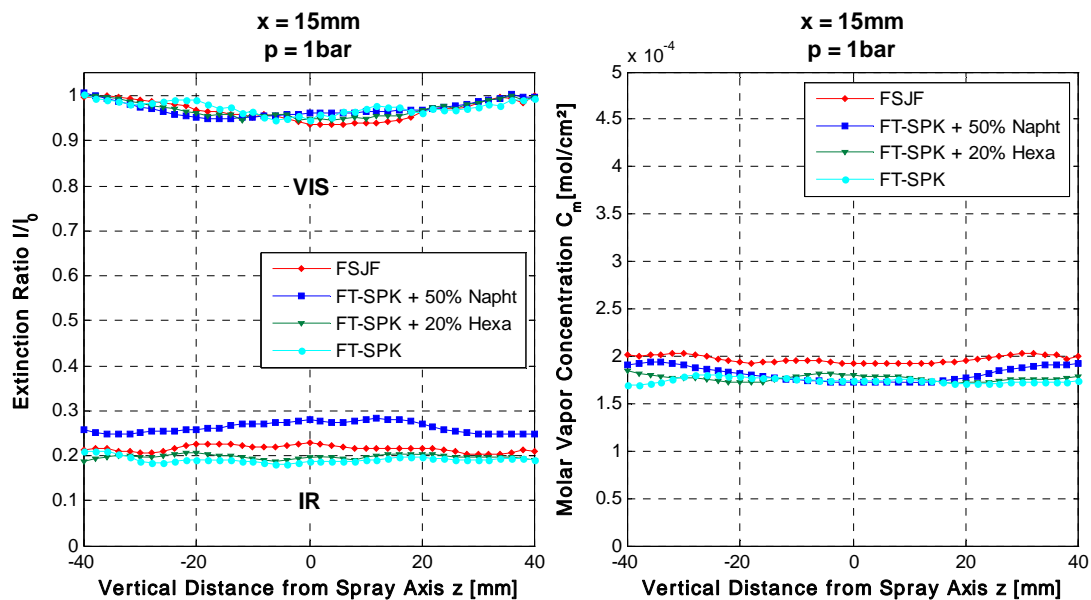


Figure 8.7: Extinction ratios in the visible and IR range for the different fuels (left)/Calculated molar vapor concentration (right) at atmospheric pressure 15mm downstream of IO ( $T=553\text{K}$ )

Figure 8.7 presents the measurement results for position  $x = 15$  mm from IO at atmospheric pressure and elevated temperature. Compared to position  $x = 6$  mm it can be seen that the curves for the visual signal are already broader and less homogeneous. The gradients of the IR signals do not show a distinct reproducibility of the hollow cone structure in the flow. The determination of the molar vapor concentration on the right hand side again is similar to position  $x = 6$  mm. The IR signal for the red curve representing FSJF shows a deviation in comparison to Figure 8.6, which can be explained on one hand by the different chemical composition and therefore a different absorption behavior and on the other hand by stability problems of the PbSe - photodiode as well as the IR laser. However the final results for the concentration values remain within the measurement accuracy limits of this technique.

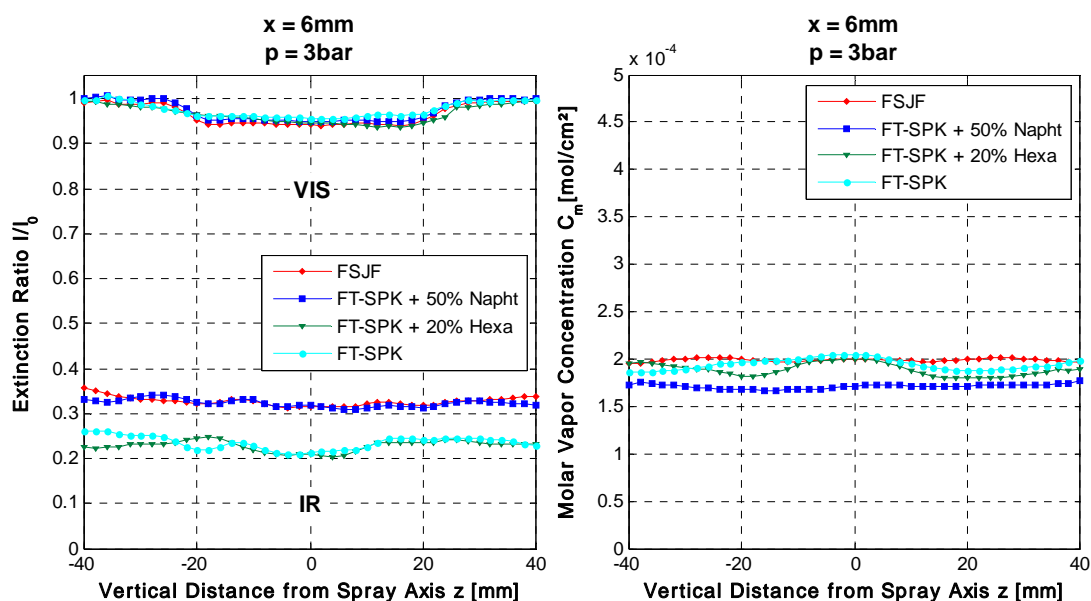


Figure 8.8: Extinction ratios in the visible and IR range for the different fuels (left)/Calculated molar vapor concentration (right) at 3 bar absolute pressure 6mm downstream of IO ( $T=553\text{K}$ )

In Figure 8.8 the results of the extinction measurements at 3 bar are shown. It can be seen here that the droplet density again characterized by the signal of the visual path changes at elevated pressure compared to atmospheric conditions. The shape is broader and less accentuated in the middle. For the IR extinction ratio again the tendencies for maxima at  $z = -15/+15$  mm can be identified but also in a less accentuated way. The molar vapor concentration tends towards higher values in the middle which can be explained by a better recirculation in the cone under pressure.

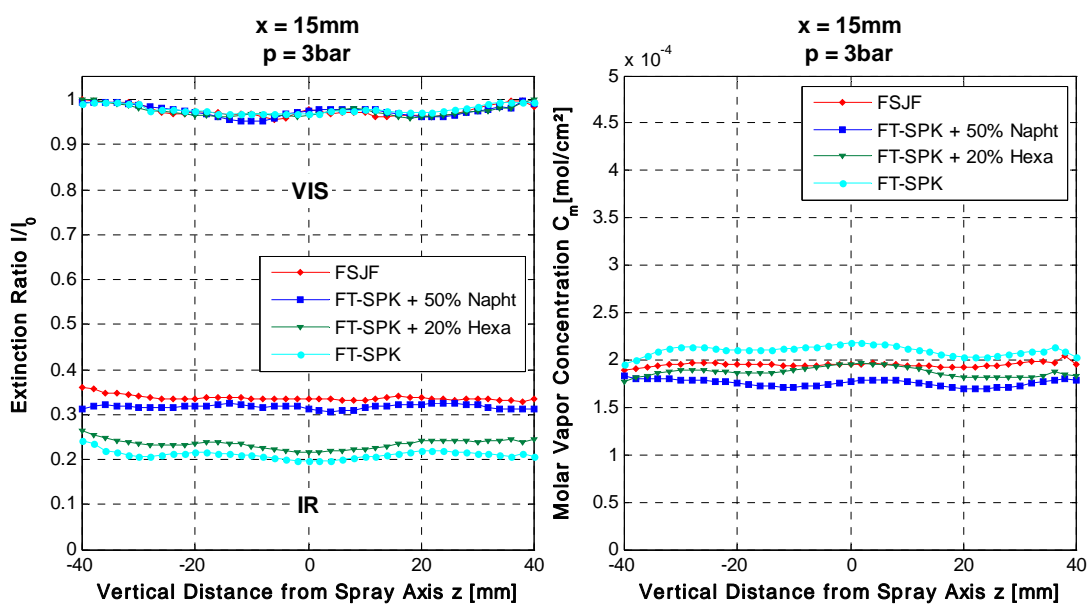


Figure 8.9: Extinction ratios in the visible and IR range for the different fuels (left)/Calculated molar vapor concentration (right) at 3 bar absolute pressure 15mm downstream of IO ( $T=553\text{K}$ )

Opposed to the behavior at atmospheric pressure the results for the 15 mm downstream position are less deviating from position  $x = 6$  mm (Figure 8.9). The visual signal devolution is again slightly broader and the extinction minima at around  $z = -15/+15$  mm still detectable. The concentration curves are pretty similar to Figure 8.8.

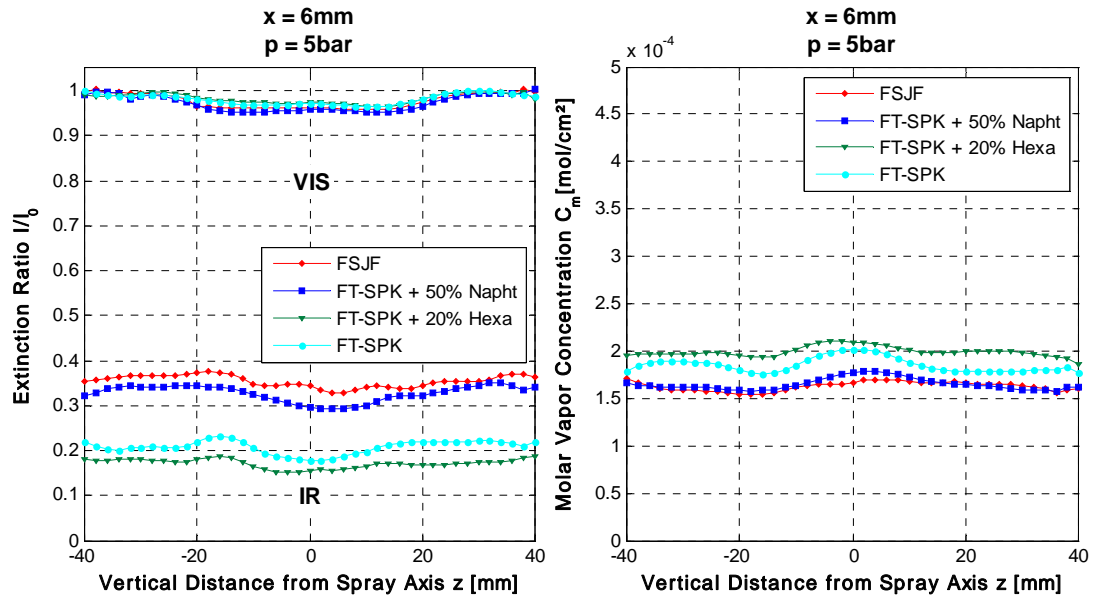


Figure 8.10: Extinction ratios in the visible and IR range for the different fuels (left)/Calculated molar vapor concentration (right) at 5 bar absolute pressure 6mm downstream of IO ( $T=553$ K)

The results of the measurements at higher pressure level respectively 5 bar at  $x = 6$  mm (Figure 8.10) reveal a near identical behavior in comparison to level 3 bar. Again it can be observed a flat and narrow signal in the visual range the obligatory maxima in the extinction ratio for the IR path and the concentration maxima in the middle of the cone. For position  $x = 15$  mm from IO at 5 bar in Figure 8.11 the devolution of the detected intensities in the visual and IR range are analogue to pressure level 3 bar. It shows a broader devolution of the visual signal while the maxima in the IR range around  $z = -15/+15$  mm can still be detected.

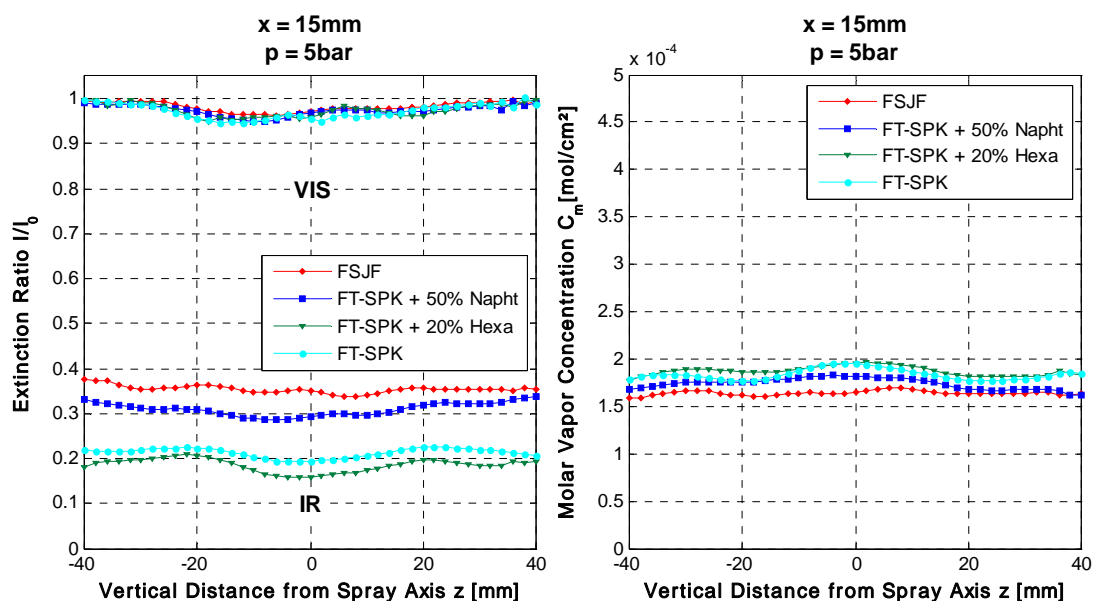


Figure 8.11: Extinction ratios in the visible and IR range for the different fuels (left)/Calculated molar vapor concentration (right) at 5 bar absolute pressure 15 mm downstream of IO ( $T=553\text{K}$ )

Finally the arithmetic mean values for the cross section of the molar vapor concentrations for the entire test matrix determined and presented in Figure 8.6 - Figure 8.11 have been computed and revealed in Figure 8.12.

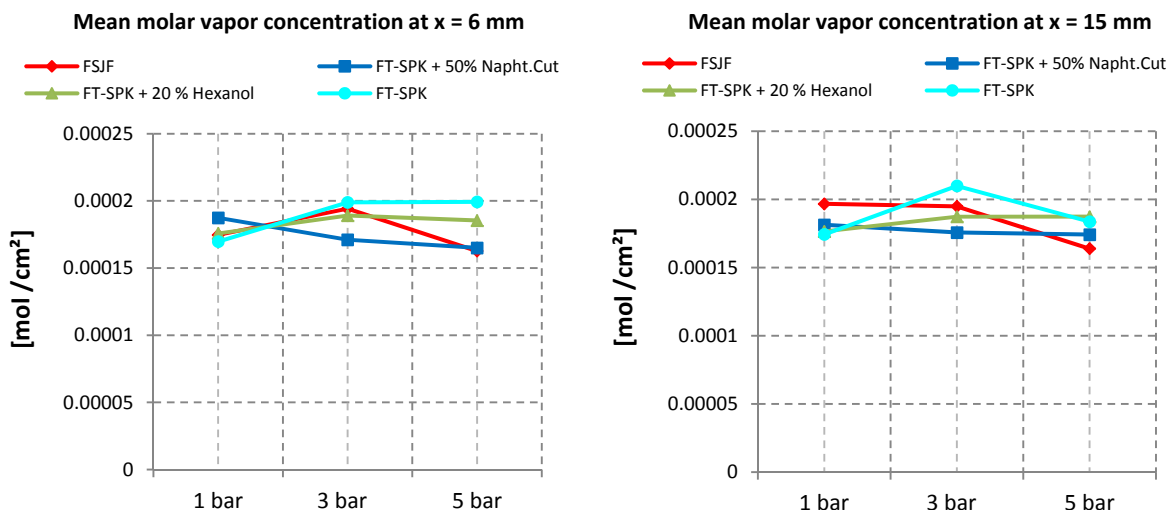


Figure 8.12: Mean values of the line of sight molar vapor concentrations of the fuel samples for different pressure values at  $x = 6\text{ mm}$  from IO (left) /  $x = 15\text{ mm}$  from IO (right)

The pressure dependency of the evaporation of the different fuel samples represented here by the mean values of their molar vapor concentration distribution is similar for both axial distances (Figure 8.12 left and right). However the comparability of the curves between the fuels is reduced, only for FT-SPK + 20 % Hexanol and FT-SPK + 50 % Naphtenic Cut a similar behavior has been detected. FT-SPK and FSJF show deviations at atmospheric pressure and high pressure (5 bar). These deviations of the measured results are again identified in the complex and very different

chemical compositions of the fuel samples resulting in different quantum states of the molecules and in the error due to the surrounding conditions, such as window displacements and different geometric preconditions produced by heat strain, which varies according to the different durations of the measurement campaigns and as a consequence different amounts of heat input. Also the measurement technique's accuracy of around 10 % has to be mentioned as an influencing factor of these results.

Summarizing the aforementioned results it can be said that the fuels show similar trends within the operational matrix. The fluctuations between the samples can be assumed as being of minor relevance since they remain inside the measurement technique's uncertainty. No dramatic influence on fuel placement as a function of the injected fuel was observed. Therefore, no contradiction regarding the injection hardware can be expected. Standard air blast injectors might be used with these products.

However having to choose the most promising fuel of these tested samples concerning the evaporation it had been identified in the FT-SPK fuel due to its best concordance pertaining to its trend in the test matrix towards the reference fuel FSJF from Sasol.

## Chapter 9

### Summary / Results

In the frame of the European Commission's FP 7 (7<sup>th</sup> Framework Program) project Alfa Bird (EU FP7: ACP/-6A-2008-213266) whose principal issues were concerned on a selection and general characterization of possible alternative fuels for aircrafts, an extensive study of the evaporation behaviour of the fuel surrogates in comparison to conventional jet fuel (here fully synthetic jet fuel based on a gas liquefaction process produced by Sasol in South Africa) had been performed.

The underlying work for this contribution was started with an extensive study addressing to existing investigations pertaining to alternatives to conventional fossil-based standard jet fuels as well as on the existence and development of new technologies especially on the combustor sector for jet engines.

The experimental part within the work for this thesis concentrated on the assessment of the suitability concerning the evaporation of the chosen alternative fuels for conventional aircraft engines. An evaporation analysis of the chosen fuel types in cooperation with Onera Fauga Mauzac (who focused on the atomization of these products) had been performed.

For these purposes an evaporation test bench had to be installed in the combustion laboratory of the Institute for Thermal Turbomachinery and Machine Dynamics at Graz University of Technology.

Firstly a new combustion chamber, based on a hollow cone radial swirl-type combustor geometry for an isothermal evaporation analysis had been designed and manufactured. An already existing test rig for hot compressed air tests had been extended with a new setup, being able to perform simultaneous tests of different fuel types. Therefore a new precise fuel supply had been integrated using Coriolis mass flow meters/regulators.

Due to the underlying tests of the evaporation being without combustion it was necessary to reduce the unburned fuel/air mixture representing an increased explosion risk inside the exhaust path of the combustion laboratory. Therefore an afterburner unit was designed, manufactured and installed downstream of the evaporation chamber before entering the exhaust tube. This unit was run by a mixture of methane and the tested fuel sample.

Before starting the required test campaigns all included test rig components were initiated and tested. Visualizations and setup tests have proven working order of all interacting compounds.

For the characterization of the evaporation a non-industrial used measurement technique had to be applied called Infrared Extinction method. Before being used in this context the technique had to be validated. An already existing setup at Onera Toulouse had been investigated in the frame of a 4 month internship at ONERA Toulouse financed by ECCOMET (Marie Curie Early Stage Research Training Fellowship; Contract # MEST-CT-2005-020426). Within these validation tests an ultrasonic injector evaporating n-octane at atmospheric conditions had been used.

Extensive optimizations and measurements have been successful and the achieved results have shown very good accordance to existing simulation results also performed at ONERA Toulouse. These results were published at ASME conference in Vancouver 2011 and published in the ASME journal.

Starting with tests in the combustion laboratory it was found out that the required test matrix postulated by the Alfa Bird consortium had to be changed due to physical limits of the measurement

technique as well as to the fact that at temperatures being higher than 600 K auto ignition tendencies were observed. Therefore the temperature in the combustion chamber had been reduced to 553 K. The IRE measurement technique applied to the combustion chamber was problematic due to the low laser power in the IR range. As a consequence the IR light was completely absorbed when directed through the measurement volume addressing to a global equivalence ratio of  $\Phi = 1$ . Referring to this the fuel mass flow rates in the test matrix had to be reduced to the least possible amount which was limited by the lowest available flow number of the parker injectors.

As this kind of combustor geometry is characterized by distinct zones of recirculation another problematic occurred related to the required onion peeling scheme for point results, which needs an area of zero fuel concentration in the boundary zones. The high amount of recirculation and low flow velocities resulted in a constant concentration of remaining fuel vapor in the boundaries. Therefore only line of sight results could be presented. However for a qualitative comparison of the chosen alternative fuel types despite the aforementioned constraints the results were sufficient. The suchlike achieved evaporation results of the fuels based on the final Alfa Bird test matrix have shown very good accordance to existing atomization data of ONERA Toulouse for all 4 different fuel types. The final outcome of the study can therefore be characterized by a principal approval of the chosen fuel types for conventional jet engine combustors. The fuels show similar behaviour with minor deviations at all different testing conditions. FT-SPK has shown the best accordance to the results for the reference fuel FSJF.

For future investigations in the evaporation process using the IRE measurement technique it has to be said, that the laser power especially in the IR range has to be adapted to the underlying geometry of the combustion chamber and the principal setup has to be improved concerning the stability of the laser signal and the photodiodes. Using combustor geometries with high zones of recirculation, as it was the case for this study also is identified as being problematic due to the necessity of zones of zero vapor concentration in the boundary zones.

Recommendations for future measurement setups using the IRE method consist firstly in the use of microbolometer arrays instead of simple photodiodes in order to analyze the beam shape and to improve and facilitate the centering of the laser beams and secondly in the use of a beam splitter and a second detector before entering the measurement volume in order to observe the stability of the used lasers for the visual and the infrared path each and as a consequence being able to compensate it within the post processing procedure.

## Chapter 10 Bibliography

- [1] IPCC Synthesis Report, 2007
- [2] Lee ,S.D. et al., Aviation and global climate change in the 21<sup>st</sup> century, *Atmospheric Environment* 43, 3520-3537, 2009
- [3] Sieber, J., Newac overview. Power point presentation, MTU Aero engines, 2010
- [4] Lefebvre, A.H, *Gas Turbine Combustion*, Second Edition, Taylor & Francis Group, 1999.
- [5] Walsh, P.P. and Fletcher, P., *Gas Turbine Performance*, Blackwell Publishing, Second edition, 2004.
- [6] Penner, J.E., Lister, D.H., Griggs, D.J., Dokken, D.J., McFarland, M. (Eds.), IPCC, 1999 - Aviation and the Global Atmosphere. Cambridge University Press, UK, 1999, pp 373.
- [7] Pachauri, R.K and Reisinger, A., *Climate Change 2007: Synthesis Report. Contribution of Working Groups I, II and III to the Fourth Assessment. Intergovernmental Panel on Climate Change (IPCC)*. Geneva, Switzerland, 2007.
- [8] Metz, B., Davidson, O.R., Bosch, P.R., Dave, R., Meyer, L.A., *Climate Change 2007: Mitigation. Contribution of Working Group III to the Fourth Assessment Report. IPCC, 2007: Intergovernmental Panel on Climate Change*. Cambridge University Press, Cambridge, United Kingdom and New York, NY, USA, 2007.
- [9] Donnerhack, S., Presentation „Beiträge der Flugtriebwerke zur Schadstoffreduktion im Luftverkehr, Workshop „Flugverkehr und Luftqualität - Partikel- und Stickoxidemissionen, UBA Berlin 2005
- [10] Smith, C.E., Talpallikar, M.V., Holdeman, J.D, A CFD study of jet mixing in reduced flow areas for lower combustor emissions. Joint Propulsion Conference. AIAA 91-2460, 1991.
- [11] ITS Karlsruhe, Homepages, 2006.
- [12] Lefebvre, A.H, *Atomization and Sprays*. Taylor & Francis Group, 1989.
- [13] Giuliani, F., Becker, J. and Hassa, C, Investigation of vapour phase, LOPOCOTEP deliverable 4.15. EU FP6 - GROWTH Project. DLR-IB-325-04-04, 2004.
- [14] Schubiger, R. et al., Rußbildung und Oxidation bei der dieselmotorischen Verbrennung, *MTZ* (63) 05-2002, p. 342 – 352.
- [15] Airbus Presentation “Alternative fuels for aircrafts”. Preparation of the Alfa-Bird project, 2007.
- [16] Rachner, M., Die Eigenschaften von Kerosin Jet A-1. Technical Report ISRN DLR-Mitt.-98-01, ISSN 1434-8462, Institute of Propulsion Technology, DLR Cologne, Germany, 1998.

- [17] Lang, A., Lecourt, R., Giuliani, F., Statistical evaluation of ignition phenomena in turbojet engines. In ASME Turbo Expo 2010: Power for Land, Sea and Air. Glasgow, UK, June 2010. GT2010-23229.
- [18] Spadaccini, L.J. and TeVelde, J.A., Autoignition characteristics of aircraft-type fuels. *Combustion and Flame*, 46:283–300, 1982.
- [19] Guin, C. Characterisation of autoignition and flashback in premixed injection systems. Applied vehicle technology panel symposium, 1999.
- [20] Giuliani, F., Advanced Gas Turbine Combustion Management - Towards Real-Time Monitored Combustors with extended Operation Range. Graz University of Technology, Habil.-Sch, 2010.
- [21] Glaude, P.-A., Fournet, R., Bounaceur, R., Molière, M., Adiabatic flame temperature from biofuels and fossil fuels and derived effect on NO<sub>x</sub> emissions. *Fuel Processing Technology*, Vol. 91, Issue 2, 2010, pp. 229-235.
- [22] Bolszo, C. D., McDonell, V. G., Evaluation of plain-jet airblast atomization and evaporation of alternative fuels in a small gas turbine engine application. *Atomization and Sprays*, Vol. 19, Issue 8, 2009, pp 771-785.
- [23] Park, S. H., Kim, H. J., Suh, H. K., Lee C. S., A study on the fuel injection and atomization characteristics of soy bean oil methyl ester (SME). *International Journal of Heat and Fluid Flow* 30, 2009, pp. 108-116.
- [24] No, S.-Y., How vegetable oils and their derivatives affect spray characteristics in CI engines – A review. *Atomization and Spray*, Vol. 21, Issue 1, 2011, pp. 87-105.
- [25] Knothe, G., Biodiesel and renewable diesel: A comparison. *Progress in Energy and Combustion Science*, Vol. 36, Issue 3, 2010, pp. 364-373.
- [26] Neste Oil, Home pages. [www.nesteoil.fi](http://www.nesteoil.fi) (Cited 31.05.2012)
- [27] Aatola, H., Larmi, M., Sarjovaara, T., Mikkonen, S., Hydrotreated Vegetable Oil (HVO) as a Renewable Diesel Fuel: Trade-off between NO<sub>x</sub>, Particulate Emission, and Fuel Consumption of a Heavy Duty Engine. SAE Technical Paper 2008-01-2500. 12 p.
- [28] Lindfors, L. P., High quality transportation fuels from renewable feedstock. XXIst World Energy Congress, 2010.
- [29] Rantanen, L., Linnaila, R., Aakko, P., Harju, T., NExBTL – Biodiesel fuel of the second-generation. SAE Technical Paper 2005-01-3771. 18 p.
- [30] Moliere, M., Vierling, M., Aboujaib, M., Patil, P., Eranki, A., Campbell, A., Trivedi, R., Nainani, A., Roy, S., Pandey, N., Gas turbines in alternative fuel application: Bio-ethanol field test. ASME Turbo Expo, 2009, GT200-59047.
- [31] Padala, S., Kook, S., Hawkes, E. R., Effect of ethanol and ambient pressure on port-fuel-injection sprays in an optically accessible intake chamber. *Atomization and Spray*, Vol. 21, Issue 5, 2011, pp. 427-445

- [32] Zhang, J., Yao, S., Patel, H., Fang, T., An experimental study on gasoline direct-injection spray and atomization characteristics of alcohol fuels and isooctane. *Atomization and Spray*, Vol 21, Issue 5, 2011, pp. 363-374.
- [33] Nojoumi H., Dincer, I., Naterer, G.F., Greenhouse gas emissions assessment of hydrogen and kerosene-fueled aircraft propulsion. *International Journal of Hydrogen Energy*, Vol. 34, Issue 3, 2009, pp. 1363-1369.
- [34] Yılmaz, I., Ilbas, M., Tastan, M., Tarhan, C., Investigation of hydrogen usage in aviation industry. *Energy Convers Manage*, 2012.
- [35] Janic, M., The potential of liquid hydrogen for the future carbon-neutral' air transport system. *Transportation Research Part D: Transport and Environment*, Vol. 13, Issue 7, 2008, pp. 428-435.
- [36] Moses, C. A., Roets, P. N., Properties, characteristics and combustion performance of Sasol fully synthetic jet fuel. *Proceedings of ASME Turbo Expo 2008, Power for Land, Sea and Air GT2008-50545*, 2008.
- [37] Chitkara, R. et al., Comparison of the performance of a real airblast nozzle working with normal/alternative fuel at atmospheric', ALFA-BIRD report D 2.1.2, Karlsruhe 2011
- [38] Dagaut, P., Diévert, P., Hajdi Ali, K., Leroy, V., Experimental database on the kinetics of reformulated kerosene combustion. ALFA-BIRD report (D10) D2.1.1, Orléans, 2010.
- [39] Karlsruhe Institute of Technology , Comparison of the performance (stability and emissions) of a real airblast nozzle working with normal/alternative fuel at atmospheric pressure ALFA-BIRD report D2.1.2, Karlsruhe, 2011.
- [40] Thomson, M., Dworkin, S., Zabeti, P., Dagaut, P., Diévert, P., Hadj Ali, K., Leroy, V., Experimental database on the effect of fuel reformulation on pollutants emissions: Specification of pollutants formed by reformulated kerosene, ALFA-BIRD report (D19) D2.1.4, Orléans, 2010.
- [41] D'Herbigny, F.-X., Bismes, F. Rouzaud, ONERA Contribution – Spray atomization and evaporation from atmospheric to high pressure: LACOM experiments. ALFA-BIRD report D2.1.7, Le Fauga-Mauzac, 2011.
- [42] Thellier, L., Report on evaluation of Well to Tank greenhouse gas emissions. ALFA-BIRD report, Rueil-Malmaison, 2012.
- [43] Stratton, R. W., Wong, H. M., Hileman, J. I., Life Cycle Greenhouse Gas Emissions from Alternative Jet Fuels., PARTNER Project 28 report, Version 1.2, 2010.
- [44] ICAO, 1993: International Standards and Recommended Practices--Environmental Protection. Annex 16 to the Convention on International Civil Aviation, Volume II: Aircraft Engine Emissions, 2nd ed. International Civil Aviation Organization, Montreal, Canada, July 1993, 63 pp.
- [45] Starck, L. et al., Overview of possible alternative fuels and selection of alternative fuels
- [46] Bogers, P. and Bauldreay, J., Results of the analysis of the initial fuel matrix - selection of the most promising fuels', ALFA-BIRD report D 1.1.2, Thornton 2009

- [47] Ruck, B., Laser-Doppler-Anemometrie, AT-Fachverlag, 1987
- [48] DANTEC homepage ,LDA Presentation, <http://www.dantecdynamics.com>
- [49] Giuliani, F., Bhayaraju, U. and C. Hassa, Analysis of air-blasted kerosene vapor concentration at realistic gas turbine conditions using laser infra-red absorption., Proceedings of the European Combustion Meeting.
- [50] Spalding, D., Combustion of fuel particles, Fuel, vol. 30, 1951.
- [51] Frackowiak, B., Approche experimentale et simulation numerique des effets d'interaction entre gouttes en evaporation, Phd thesis, 'Ecole Nationale Sup'erieure de l'A'eronautique et de l'Espace, Toulouse, 2007.
- [52] Brandt, M., Lasermesstechnische Untersuchung der Kerosin-verdampfung und -mischung für die magere Vormischbrennung unter erhöhtem Druck, FB 1999-25, DLR, Institute of Propulsion Technology, DLR Cologne, Germany, 1999
- [53] Drallmeier, J., Hydrocarbon vapor measurements in fuel sprays: a simplification of the infrared extinction technique, Applied Optics, vol. 33, No.30, pp. 7175–7179, 1994.
- [54] Hammond-jr., D.; Deconvolution technique for line-of-sight optical scattering measurements in axisymmetric sprays, Applied Optics, vol. 20, No.3, pp. 493–499, 1981
- [55] Fernandez, V.G., Berthoumieu and P., Lavergne, G., Liquid sheet disintegration at high pressure: An experimental approach C. R. Mecanique 337 (2009) 481—491
- [56] Wagner, B., Fuel vapor concentration measurements on droplets by Infrared Extinction, doctoral thesis University of Toulouse; 10. december 2009
- [57] Skinner, M., Use of infrared analysers for continuous measurement of the concentration of carbon monoxide in a moist and dusty atmosphere, Modern Utilization of Infrared Technology V, vol. 197, pp. 281–286, 1979.
- [58] Bodoc, V., Wilms, J., Biscos, Y., Lavergne, G. and Rouzaud, O., Experimental and numerical investigation of a monocomponent polydisperse spray, Proceedings of the 22nd European Conference on Liquid and Atomization and Sprays, Como Italy, 2008.
- [59] Klingbeil, A., Mid-IR Laser Absorption Diagnostics For Hydrocarbon Vapor Sensing in Harsh Environments, Phd thesis, Stanford University, Cambridge, MA, 2007
- [60] Günzler H., Böck H.. IR-Spektroskopie 2.Auflage, Weinheim, Verlag Chemie, ISBN 3-527-21089-X,1983
- [61] Pinkley, L.W., Sethna, P.P, Williams D., 'Infrared band intensities of saturated Hydrocarbons', Journal of physical chemistry, Vol 82, 1978.
- [62] Hammond-jr., D., Deconvolution technique for line-of-sight optical scattering measurements in axisymmetric sprays, Applied Optics, vol. 20, No.3, pp. 493–499, 1981
- [63] Pommersberger, K., Untersuchung der Gemischaufbereitung in Gasturbinenbrennkammern unter Berücksichtigung der Eigenschaften kommerzieller Flüssigbrennstoffe, Dissertation Karlsruhe Instiutue of Technology (KIT), 2003

- [64] Lui, C. W., Clarkson, M. und Nicholls, R. W. (1996): An approximation for spectral extinction of atmospheric aerosols. *Journal of Quantitative Spectroscopy & Radiative Transfer*, Bd. 55, S. 519–531.
- [65] van de Hulst, H. C. (1981): *Light scattering by small particles*. Dover Publications, New York
- [66] Lefebvre, A.H. , *Atomization and Sprays* (Hemisphere, New York, 1989), Chap. 3, p. 85.
- [67] Leitgeb, T et al. (2009), *Design and Validation of the Air System for a Versatile Turbine and Combustion Chamber Test Facility*, 8th European Conference on Turbomachinery Fluid Dynamics and Thermodynamics, Graz, Austria, pp 853-863
- [68] [www.sico.at](http://www.sico.at), product data sheet
- [69] Rachner, M., *Die Stoffeigenschaften von Kerosin Jet A1*, DLR Mitteilung 98-01, Institute of Propulsion Technology, DLR Cologne, Germany, 1999
- [70] Beaton, C.F. and Hewitt, G.F., *Physical property data for the design engineer*, ISBN 0-89116-739-0, Hemisphere Publishing Corporation, 1989
- [71] Gal, T., Lakatos, B.G. *Thermal cracking of recycled hydrocarbon gas-mixtures for re-pyrolysis: Operational analysis of some industrial furnaces*, *Applied Thermal Engineering* 28 218-225, 2008
- [72] <http://www.gaseq.co.uk/>
- [73] Camps, A., *Automated ignition for safe start at intermediate pressure conditions*. Technical report, Graz University of Technology, 2008.
- [74] *VDI Wärmeatlas*, ISBN 13 978-3-540-25504-8
- [75] Suttrop, F., *Gasturbinenbrennkammern für Triebwerksbauer*, FH Aachen
- [76] Giuliani, F., *Gas turbine combustion*, Graz University of Technology, Lecture script, 2010.
- [77] Lang, A. , *Konstruktion eines Brennkammer-Prüfstandes und Messungen unter mittlerem Druck*, Graz University of Technology, Diploma thesis, 2007.
- [78] Lang, A. *Unsteady Combustion Phenomena in current and Future Aero Engines*, Graz University of Technology, Doctoral thesis, 2011